Materials Optimization and GHz Spin Dynamics of Metallic Ferromagnetic Thin Film Heterostructures

Cheng Cheng

Submitted in partial fulfillment of the

requirements for the degree

of Doctor of Philosophy

in the Graduate School of Arts and Sciences

COLUMBIA UNIVERSITY

2014

Abstract

Materials Optimization and GHz Spin Dynamics of Metallic Ferromagnetic Thin Film Heterostructures

Cheng Cheng

Metallic ferromagnetic (FM) thin film heterostructures play an important role in emerging magnetoelectronic devices, which introduce the spin degree of freedom of electrons into conventional charge-based electronic devices. As the majority of magnetoelectronic devices operate in the GHz frequency range, it is critical to understand the high-frequency magnetization dynamics in these structures.

In this thesis, we start with the static magnetic properties of FM thin films and their optimization via the field-sputtering process incorporating a specially designed *in-situ* electromagnet. We focus on the origins of anisotropy and hysteresis/coercivity in soft magnetic thin films, which are most relevant to magentic susceptibility and power dissipation in applications in the sub-GHz frequency regime, such as magnetic-core integrated inductors.

Next we explore GHz magnetization dynamics in thin-film heterostructures, both in semi-infinite samples and confined geometries. All investigations are rooted in the Landau-Lifshitz-Gilbert (LLG) equation, the equation of motion for magnetization. The phenomenological Gilbert damping parameter in the LLG equation has been interpreted, since the 1970's, in terms of the electrical resistivity. We present the first interpretation of the size effect in Gilbert damping in single metallic FM films based on this electron theory of damping.

The LLG equation is intrinsically nonlinear, which provides possibilities for rf signal processing. We analyze the frequency doubling effect at small-angle magnetization

precession from the first-order expansion of the LLG equation, and demonstrate second harmonic generation from $Ni_{81}Fe_{19}$ (Permalloy) thin film under ferromagnetic resonance (FMR), three orders of magnitude more efficient than in ferrites traditionally used in rf devices. Though the efficiency is less than in semiconductor devices, we provide field- and frequency-selectivity in the second harmonic generation.

To address further the relationship between the rf excitation and the magnetization dynamics in systems with higher complexity, such as multilayered thin films consisting of nonmagnetic (NM) and FM layers, we employ the powerful time-resolved x-ray magnetic circular dichroism (TR-XMCD) spectroscopy. Soft x-rays have element-specific absorption, leading to layer-specific magnetization detection provided the FM layers have distinctive compositions. We discovered that in contrast to what has been routinely assumed, for layer thicknesses well below the skin depth of the EM wave, a significant phase difference exists between the rf magnetic fields H^{rf} in different FM layers separated by a Cu spacer layer. We propose an analysis based on the distribution of the EM waves in the film stack and substrate to interpret this striking observation.

For confined geometries with lateral dimensions in the sub-micron regime, there has been a critical absence of experimental techniques which can image small-amplitude dynamics of these structures. We extend the TR-XMCD technique to scanning transmission x-ray microscopy (STXM), to observe directly the local magnetization dynamics in nanoscale FM thin-film elements, demonstrated at picosecond temporal, 40 nm spatial and $< 6^\circ$ angular resolution. The experimental data are compared with our micromagnetic simulations based on the finite element analysis of the time-dependent LLG equation. We resolve standing spin wave modes in nanoscale $Ni_{81}Fe_{19}$ thin film ellipses (1000 nm $\times$ 500 nm $\times$ 20 nm) with clear phase information to distinguish between degenerate eigenmodes with different symmetries for the first time. With the element-specific imaging capability of soft x-rays, spatial resolution up to 15 nm with improved optics, we see great potential for this technique to investigate functional devices with multiple FM layers, and provide insight into the studies of spin injection, manipulation and detection.

Contents

List of Figures **v**

List of Tables **viii**

0.1 Publication List ix

Acknowledgments **xi**

Chapter 1 Introduction **1**

1.1 Thesis outline 2

Chapter 2 Static magnetic properties: the hysteresis loop and its control via field-sputtering **5**

2.1 Introduction 5

2.2 Looking into the hysteresis loop 7

2.2.1 Induced uniaxial anisotropy 8

2.2.2 Permeability and initial susceptibility 15

2.2.3 Coercive field 20

2.3 Kinetics of magnetron sputtering and thin film growth 23

2.3.1 Magnetron sputtering 23

2.3.2 Film growth, the thickness dependence 26

2.4 Field-sputtering: *in-situ* quadrupole electromagnet 28

2.4.1 Introduction to field-sputtering 30

2.4.2 Instrumentation 31

2.4.3 Demonstration 36
2.4.4 Summary of the field-sputtering using *in-situ* electromagnet 40
2.5 Summary 41

Chapter 3 Laminated $Co_{91.5}Zr_{4.0}Ta_{4.5}$ and $Ni_{80}Fe_{20}$ thin films: implementation in magnetic-core integrated inductors 42

3.1 Introduction: magnetic-core integrated inductors 43
3.2 Experiment 44
3.2.1 Core loss in inductors 44
3.2.2 Single-layer FM film optimization 45
3.2.3 Bilayer patterned FM films: magnetic flux closure between the layers and rotational response 47
3.3 Conclusion and outlook 51

Chapter 4 The Landau-Lifshitz-Gilbert equation: equation of motion for magnetization dynamics 52

4.1 Circular precession 53
4.2 Elliptical precession: in-plane FMR for a thin film 56
4.3 Power absorption in FMR 61

Chapter 5 Electron theory of Gilbert damping in fast magnetization dynamics of itinerant ferromagnets 62

5.1 The electronic theory of Gilbert damping 63
5.1.1 Building up the effective field model 63
5.1.2 Breathing Fermi surface 66
5.1.3 Bubbling Fermi surface 67
5.2 Experimental approach: Gilbert damping and the electron scattering time . 68
5.2.1 Instrumentation: temperature-dependent α and ρ 69
5.2.2 The samples 77
5.2.3 Results and discussion 79

5.3 Summary and outlook 91

Chapter 6 Nonlinear effect of LLG at small angle precession: high-efficiency GHz frequency doubling without power threshold in thin-film $Ni_{81}Fe_{19}$ 93

6.1 Introduction: nonlinearity in LLG equation 94

6.2 Experiment: detecting FMR and second harmonic generation using spectrum analyzer 95

6.2.1 Experimental setup 95

6.2.2 Experimental data: power absoprtion at FMR and emission at the second harmonic 96

6.3 Analysis: first-order expansion of LLG with longitudinal rf field 98

6.3.1 The equation of motion for perturbation terms 98

6.3.2 Power of the second harmonic generation 100

6.3.3 Power ratio between FMR and the second harmonic 102

6.4 Summary 103

Chapter 7 X-ray magnetic circular dichroism and pump-probe technique 104

7.1 X-ray mangeitc circular dichroism (XMCD) 105

7.2 The pump-probe technique 107

7.3 Sample preparation 109

7.3.1 The substrate 109

7.3.2 The FM thin film 112

Chapter 8 Detection of microwave phase variation in nanometer-scale magnetic heterostructures 113

8.1 Introduction 114

8.2 Experiment 116

8.2.1 The samples 116

8.2.2 TR-XMCD measurements 117

8.3 Results 121

8.4 Calculations: response of magnetization to incident rf fields 122
8.5 Discussion 127
8.6 Conclusions 128

Chapter 9 Time-resolved scanning transmission x-ray microscopy for resolving small-angle magnetization dynamics in confined geometries 129

9.1 Stochastic limits in synchronous imaging of sub-micron magnetization dynamics 131
9.1.1 Introduction 131
9.1.2 Experimental Technique 132
9.1.3 Results and discussion 135
9.1.4 Summary 138
9.2 Submicron mapping of GHz magnetic susceptibility 139
9.2.1 Introduction 139
9.2.2 The sample 140
9.2.3 Experimental technique: FMR-STXM 141
9.2.4 Data analysis 144
9.2.5 Conclusion 146
9.3 Phase-resolved imaging of spin-wave eigenmodes in submicron ellipses using scanning transmission xray microscopy 148
9.3.1 Introduction: spin-wave eigenmodes 149
9.3.2 Experiment: odd and even excitation 152
9.3.3 Results and discussion 155

List of Figures

2.1 An assortment of hysteresis (M-H) loops 6

2.2 The loop: H_k, H_c and μ 7

2.3 The induced anisotropy: dependence on dopant concentration 15

2.4 The Stoner-Wohlfarth model 16

2.5 Initial susceptibility χ_{init} for coherent **M** rotation in the Stoner-Wohlfarth model 17

2.6 Energy of the 180° domain wall 18

2.7 Initial susceptibility χ_{init} of the 180° domain wall 19

2.8 Initial susceptibility χ_{init} of the 90° domain wall 20

2.9 Ripple domains and hard-axis coercivity 21

2.10 Surface irregularities and easy-axis coercivity 22

2.11 Diagram of the magnetron sputtering system 24

2.12 Kinetics of the sputtering process: at the target 25

2.13 Kinetics of the sputtering process: at the substrate 26

2.14 Thin film growth zones 27

2.15 Toroidal isotropic magnetic core for an integrated inductor 29

2.16 ac permeability along the hard- and easy-axes in a thin film 29

2.17 Layout of the field-sputtering system 32

2.18 Working principle of field generation from the quadrupole electromagnet . . 35

2.19 Magnitude of field from the quadrupole electromagnet 36

2.20 Alignment of the sample in field-sputtering 37

2.21 *B-H* loops of field-sputtered single-layer FM extended thin films 38
2.22 Ferromagnetic resonance field dependence on sample orientation in thin films with uniaxial anisotropy 39
2.23 Demonstration of the vector of magnetic anisotropy in FM thin films using the *in-situ* quadrupole electromagnet 40

3.1 Thickness dependence of coercivity in single-layer films 46
3.2 Sputtering voltage dependence of coercivity in single-layer films 47
3.3 *M-H* loops for $Co_{91.5}Zr_{4.0}Ta_{4.5}$(200 nm)/$SiO_2$(4 nm)/$Co_{91.5}Zr_{4.0}Ta_{4.5}$(200 nm) structures 49
3.4 STXM images for a Py/SiO_2/CoFeB element 50

4.1 Circular precession of $\mathbf{M}$ 53
4.2 Elliptical precession of $\mathbf{M}$ 57
4.3 Parallel susceptibility 60

5.1 Breathing and bubbling Fermi surface models 65
5.2 Temperature-dependent measurement of resistivity 70
5.3 Sheet conductance as a function of film thickness 74
5.4 Temperature-dependent measurement of Gilbert damping parameter 76
5.5 Extracting α from FMR 78
5.6 Samples for $\alpha(\rho)$ 78
5.7 α and ρ dependence on FM layer thickness t_{FM} 80
5.8 α as a function of ρ at 300 K for t_{FM} series 81
5.9 T-dependent M_s in Co 85
5.10 T-dependent perpendicular anisotropy in Co thin films 86
5.11 α as a function of ρ in T series 88
5.12 α as a function of ρ 90

6.1 Experimental setup for observing FMR and second harmonic generation . . 96

6.2 FMR and second harmonic generation as a function of the input power . . . 97
6.3 Second harmonic generation spectrum 102

7.1 X-ray mangeitc circular dichroism (XMCD) 105
7.2 The differential XMCD spectrum 106
7.3 Rf excitation and timing electronics for the pump-probe technique 108
7.4 Sample mount assembly for the pump-probe XMCD experiments 110
7.5 E-beam sample on Si_3N_4 membrane 112

8.1 Detection of the**M** precession amplitude and phase using TR-XMCD 115
8.2 Magnetic field bias dependence of layer-specific precession 119
8.3 Phase and amplitude of magnetization precession in two FM layers 120
8.4 Calculated phase offset 126

9.1 STXM at CLS 130
9.2 Experimental setup for TR-STXM at CLS using dual-gate photon counter . 134
9.3 Static STXM images showing domain configuration 135
9.4 15 nm Permalloy ellipse static hysteresis loops 136
9.5 Dynamic images 137
9.6 TR-STXM for measuring GHz magnetic susceptibility 143
9.7 Cone angle and phase map 145
9.8 Map of the complex susceptibility 146
9.9 Spin-wave normal modes 149
9.10 Edge mode and uniform mode 151
9.11 The rf circuit 152
9.12 Samples for odd and even excitation 154
9.13 The edge mode images 156
9.14 The mixed mode (between 'edge' and 'uniform') images 157
9.15 The mode images for a dipolarly coupled sample pair 158
9.16 Symmetric phase map under even excitation 159

List of Tables

5.1 Temperature-dependent $4\pi M_s$ for bulk *hcp* Co. 87

5.2 Fitting parameters for Co. 89

5.3 Fitting parameters for $Ni_{81}Fe_{19}$. 89

5.4 Fitting parameters for $Co_{60}Fe_{20}B_{20}$. 91

0.1 Publication List

Manuscripts in preparation, *presented at the 58th MMM conference*

1. *Size- and temperature-dependent damping in ferromagnetic ultrathin films: role of electron scattering time in Co, $Co_{60}Fe_{20}B_{20}$ and $Ni_{81}Fe_{19}$*, **C. Cheng**, A. Ghosh, S. Auffret, U. Ebels, W. E. Bailey (2013)

2. *Phase-resolved imaging of spinwave eigenmodes in submicrometer ellipses using scanning transmission x-ray microscopy (STXM)*, **C. Cheng** and W. E. Bailey (2013)

Accepted/In press

3. *High-efficiency GHz second harmonic generation from thin-film $Ni_{81}Fe_{19}$ in ferromagnetic resonance*, **C. Cheng** and W. E. Bailey, `Applied Physics Letters`, to appear (2013)

Published

4. *Detection of microwave phase variation in nanometer-scale magnetic heterostructures*, W. E. Bailey, **C. Cheng**, R. Knut, O. Karis, S. Auffret, S. Zohar, D. Keavney, P. Warnicke, J-.S. Lee, D.A. Arena, `Nature Communications`, **4** 2025 (2013)

5. *Coupled inductors with crossed-anisotropy $CoZrTa/SiO_2$ multilayer cores*, R. Davies, N. Sturcken, **C. Cheng**, W.E. Bailey, K. Shepard, `IEEE Transactions on Magnetics`, **49** 7 4009 (2013)

6. *Optimization of ultrasoft $CoZrTa/SiO_2/CoZrTa$ trilayer elements for integrated inductor structures*, **C. Cheng**, R. Davies, N. Sturcken, K. Shepard, W.E. Bailey, `Journal of Applied Physics`, **113** 17A343 (2013)

7. *Sub-micron mapping of GHz magnetic susceptibility using scanning transmission x-ray microscopy*, **C. Cheng** and W.E. Bailey, `Applied Physics Letters`, **101** 182407 (2012)

8. *Vector control of induced magnetic anisotropy using an in-situ quadrupole electromagnet in ultra-high vacuum sputtering*, **C. Cheng**, N. Sturcken, K. Shepard, W.E. Bailey, `Review of Scientific Instruments`, **83** 063903 (2012)

9. *Stochastic limits in synchronous imaging of submicron magnetization dynamics using scanning transmission x-ray microscopy*, **C. Cheng**, K. Kaznatcheev, W.E. Bailey, `Journal of Applied Physics`, **111** 07E321 (2012)

10. *Design of coupled power inductors with crossed-anisotropy magnetic core for integrated power conversion*, N. Sturcken, R. Davies, **C. Cheng**, W.E. Bailey, K. Shepard, `IEEE Applied Power Electronics Conference and Exposition (APEC)`, 417 (2012)

11. *Synchronous (lock-in) measurement techniques for magnetic contrast enhancement in STXM*, K. Kaznatcheev, D. Bertwistle, **C. Cheng**, S. Zohar, W.E. Bailey,`AIP Conference Proceedings (USA)`, 1365 333 (2011)

Acknowledgments

First and most of all, I would like to thank my advisor, Professor William Bailey, for his great mentoring during my time at Columbia. I have learned the style of conducting careful experiments and logical thinking from working closely with him at multiple synchrotron experiments and via countless enlightening discussions throughout my study; and the seemingly endless revisions of manuscripts lead me to the right path of writing a good article –all of which are the essential skills for a scientist. Prof. Bailey's dedication to science and most remarkably, his persistence in solving difficult problems through carefully designed experiments carried out over years have been most inspiring for a young researcher like me. I would never have come to this point without his constant guidance, corrections, and encouragement.

Thanks to Prof. Irving Herman, Prof. I. Cevdet Noyan and Prof. Bailey for serving on my thesis proposal committee. Thanks to Prof. Katayun Barmak, Prof. Latha Venkataraman, Prof. Abhay Pasupathy, Prof. Kenneth Shepard and Prof. Bailey for taking time from their busy schedules to serve on my thesis defense committee.

I would like to thank Dr. Sioan Zohar and Dr. Noah Sturcken for being my mentors in the laboratory. They had spared great amount of time and patience in teaching me each and every basic lab skill. Noah has provided extraordinarily generous help within and beyond our collaboration project, introduced me to Dr. Jacob Rosenstein and Jared Roseman who had provided me the invaluable help with SiN membrane fabrication and e–beam lithography. Dr. Erika Penzo gave incisive discussions and suggestions on the improvement of nanofabrication. Dr. Abhijit Ghosh and Dr. Stephane Auffret at SPIN-

TEC/CEA/CNRS, Grenoble, France provided some samples and measurements in Chap. 5 and Chap. 6. Thanks to Dr. GUAN Yongfeng and Dr. JIA Zhang, who I never met in person but provided so much help during my late stage of PhD on the subject of career development.

I would like to thank my collaborators during the synchrotron trips, Dr. Dario Arena, Dr. Konstantine Kaznatcheev, Dr. WANG Jian, Prof. Olof Karis, Dr. Peter Warnicke and Dr. Ronny Knut, for their inspirational discussions and great humor. Special thanks to Peter, who shares the passion not only on physics but also on so many other subjects, and gives constant encouragement during my difficult times.

Thanks to all the fellow students throughout my 5 years at APAM. I have greatly enjoyed the time spent with them on and off campus, about or irrelevant to physics.

Finally I would like to express my most sincere gratitude towards my family and friends. My father CHENG Jian and mother LAI Ming, for being my role models, giving most inspirational discussions like friends, and unreserved support and encouragement throughout my PhD. Greatest friends over a decade, SUN Guan, CHEN Guannan and TIAN Miao, who are also working towards their PhD here. They have always been there whenever I needed them, to share the light and darkness of life. Thanks to a very special person XU Jiong, for sharing the great beauty of physics, nature, and much more.

Chapter 1

Introduction

The field of spintronics (spin-electronics) [1], which combines the charge and spin degree of freedom of electrons, has thrived in the past two decades. Metallic ferromagnetic (FM) materials in thin-film form, based on $3d$ transition metal alloys, are widely used in spintronic devices and are particularly attractive for their compatibility with existing CMOS processing technology. In this thesis, we look into the static and dynamic properties of these $3d$ transition metal alloy thin films, with focus on GHz magnetization dynamics in FM heterostructures.

The Landau-Lifshitz-Gilbert (LLG) equation governs the fast magnetization dynamics and is the center of this thesis. We treat it in systems with increasing complexitiy. First, we start with the simplest case of uniform magnetization/macrospin precession in the linear regime, with homogeneous rf driving magnetic field in a semi-infinite extended FM film, and investigate the microscopic origins of the Gilbert damping term. Next we introduce the first-order nonlinearity of the LLG equation, still within the macrospin model under uniform excitation, and understand the emergence of second harmonic and its device potential in the small-angle precession limit. Further extending the system to multilayered structures, we see inhomogeneous excitation field across the film stack, observing the depth-dependent effective rf field in the film using time-resolved (TR) x-ray magnetic circular dichroism (XMCD) spectroscopy. Here the magnetization precession amplitude and phase have to be

analyzed with the combination of the LLG equation and the Maxwell's equations. Finally we have FM thin film heterostructures with confined lateral geometries. In these systems, when we have homogeneous static magnetization under large external bias, standing spin waves in the film plane occur under uniform excitation, due to the finite film size. For an element in the remanent state, nonuniform magnetic domain structures introduce inhomogeneous effective magnetic fields within the element, which results in extremely localized dynamic responses. We bring in the numerical calculations, based on the finite-element analysis of the LLG equation, to interpret the experimental data we obtained employing the TR-scanning transmission x-ray microscopy (STXM) with spatial resolution of 40 nm.

1.1 Thesis outline

I would group the following chapters of this thesis into three parts.

1. The **materials optimization part**, which includes Chapters 2 and 3:

   - **Chapter 2**, '*Static magnetic properties: the hysteresis loop and its control via field-sputtering*', describes 1) the static magnetic properties that we could read from a hysteresis loop, and their physical origins; 2) the sputtering process: tuning the parameters and their influence on the microstructure, surface and interface properties, and the relationship with soft magnetic properties; 3) the design and implementation of the *in-situ* electromagnet for field sputtering (Publication list **8**).

   - **Chapter 3**, '*Laminated* $Co_{91.5}Zr_{4.0}Ta_{4.5}$ *and* $Ni_{80}Fe_{20}$ *thin films: implementation in magnetic-core integrated inductors*', describes the magnetic-core integrated inductor project and the results of materials optimization (Publication list **6, 5, 10**) based on the guidelines in *Chapter 2*.

2. The **magnetization dynamics part**, which includes Chapters 4, 5 and 6, where we introduce the *LLG equation*, look into the physical origin of the Gilbert damping

parameter, and explore possibilities in rf processing with the samll-angle nonlinear effect of the LLG.

- **Chapter 4**, '*The Landau-Lifshitz-Gilbert equation: equation of motion for magnetization dynamics*' describes 1) the LLG eqation, 2) the thin film linearized case, fundamentals of ferromagnetic resonance (FMR).
- **Chapter 5**, '*Electron theory of Gilbert damping in fast magnetization dynamics of itinerant ferromagnets*', discusses the physical origin, the electron scattering mechanism, of the phenomenological Gilbert damping parameter in metallic ferromagnets based on $3d$ transition elements; it gives a review of the theoretical approach and presents our experimental data in three commonly used device ferromagnets (Publication list **1**).
- **Chapter 6**, '*Nonlinear effect of LLG at small angle precession: high-efficiency GHz frequency doubling without power threshold in thin-film* $Ni_{81}Fe_{19}$', describes the nonlinearity of the LLG equation in the small-angle limit, the analytical form of the second harmonic generation, and demonstrates the experimental observation of the frequency doubling effect (Publication list **3**).

3. The last part is a dedicated section for our **synchrotron experiments** which have been a continuous effort over years and perhaps contains some of the most intriguing results found during my dissertation research.

   - **Chapter 7**, '*X-ray magnetic circular dichroism and pump-probe technique*', describes the origin of magnetic contrast from soft x-ray, the x-ray magnetic circular dichroism (XMCD), the working principles of the pump-probe technique, and desbribes the special sample preparation required by x-ray spectroscopy and microscopy.
   - **Chapter 8**, '*Detection of microwave phase variation in nanometre-scale magnetic heterostructures*', describes the large phase variation in the magnetization precession over different layers of FM materials in nanoscale heterostructures, ob-

served by TR-XMCD spectroscopy, and its interpretation by solving Maxwell's equations and the LLG equation (Publication list **4**).

- **Chapter 9**, '*Time-resolved scanning transmission x-ray microscopy for resolving small-angle magnetization dynamics in confined geometries*', describes the TR-STXM work(Publication list **2, 7, 9, 11**), with the initial demonstration of the technique in a micrometer scale CoZrTa element, and the subsequent work in nanoscale Permalloy elements showing phase-resolved imaging of standing spin-wave eigenmodes and corresponding micromagnetic simulations results.

Chapter 2

Static magnetic properties: the hysteresis loop and its control via field-sputtering

2.1 Introduction

The hysteresis loop, the dependence of magnetization M on the auxillary magnetic field H, contains much information about a ferromagnetic (FM) thin film structure. Fig. 2.1 exhibits *M-H* loops for different materials and heterostructures, with the panel (a) representing the most 'standard' loops of a single-layer extended FM film with uniaxial anisotropy, the blue and green loops for the *easy*- and *hard*-axes respectively. In this chapter, we will focus on the single-layer extended FM film case, since it is the building block of any other systems with higher complexity and reflects mostly the intrinsic properties of the magnetic material.

In the first part of this chapter, we will look into the physical origins of the properties that we read from the hysteresis loop, *i.e.* (1) the uniaxial anisotropy K_u induced in soft FM thin films by atomic pair-ordering, (2) the permeability μ_r from the major loop and the initial susceptibilities from the minor loops and (3) the coercivity H_c and its relationship to the microstructure and morphology of the thin film. Next we review the basic working

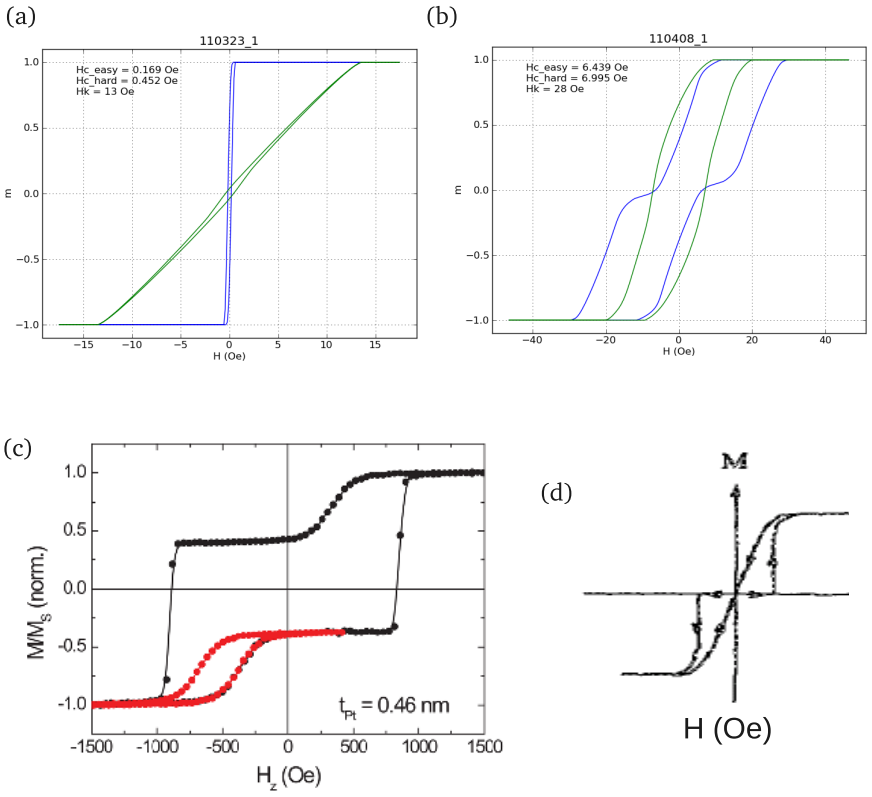

Figure 2.1: Illustration of typical hysteresis (M-H) loops for various magnetic thin film systems. (a) the most 'standard' hysteresis loops, the blue curve for the *easy*-axis and the green curve for the *hard*-axis, of a single-layer extended film; (b) M-H loops measured from a bilayer film; (c) hysteresis loops in a multilayered system with perpendicular anisotropy and interlayer exchange coupling [2]; (d) easy-axis hysteresis loop of a sample with magnetic domain wall pinning [3].

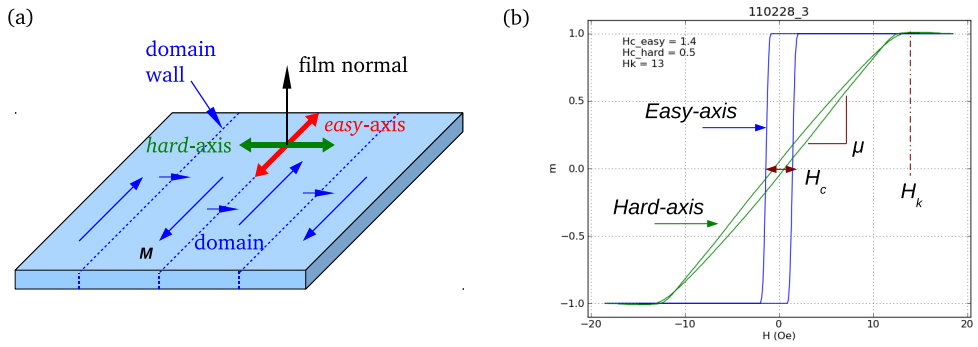

Figure 2.2: A closer look at the type of loop in Fig. 2.1(a). (a) The remanence state (zero bias field) of an extended single-layer FM film with uniaxial anisotropy, showing magnetization along the *hard*-axis in domain walls; (b) The hysteresis loop illustrating the anisotropy field H_k, the permeability μ and the coercivity H_c.

principles of magnetron field-sputtering with a focus on the kinetic model of the adatoms on the surface of the film from the sputtering process, relate the sputtering parameters to the film quality, then thus build the connection between the soft ferromagnetic properties and the control of sputtering parameters. The last section of this chapter addresses the experimental aspects with detailed description of the design and incorporation of our *in-situ* electromagnet in the ultra-high vacuum (UHV) sputtering chamber for field-sputtering. Finally we will conclude with the experimental data from field-sputtered single-layer FM extended films, demonstrating vector control of the induced anisotropy using this *in-situ* electromagnet.

2.2 Looking into the hysteresis loop

For a uniaxially anisotropic film we are interested in, Fig. 2.2 (a) shows the relaxed magnetization configuration under zero bias and introduces some basic concepts. There is one axis in the film plane, the *easy*-axis, along which the film will be uniformly magnetized under a minimum external field. The axis perpendicular to the easy-axis in the film plane is the hard-axis: the free energy of the system reaches its maximum for the magnetization

to lie along this axis, and the highest external field is required to magnetize the film along this direction. Taking a closer look at the hard-axis hysteresis loop in Fig 2.2 (b), we notice three critical parameters, H_k, μ and H_c. The anisotropy field H_k is the external field value at which the film is uniformly magnetized, *i.e.* reaches its saturation magnetization. The relative permeability μ_r is defined as the slope of the loop, $\mu_r = 1+\chi_M = 1+M_s/H_k \simeq M_s/H_k$. The hard-axis loop is strictly linear in the single-domain Stoner-Wohlfarth model because of the reversible, coherent rotation of the magnetization; however, in realistic thin film systems, the ideal case of a single magnetic domain is unusual. Due to the existance of domain walls, there is always a remanent magnetization along the hard-axis when the external field is reduced to zero, as shown in Fig. 2.2 (a). We define the external field under which the film exhibits *zero* net magnetization as the coercive field, or coercivity H_c. The area enclosed by the hysteresis loop indicates the power dissipated by the magnetization when the material is cycled under cyclic external magnetic field. Therefore, it is important to pay attention to the coercivity and to minimize it for reduced power consumption in some applications.

2.2.1 Induced uniaxial anisotropy

In this section, we look into the physical origin of the induced uniaxial anisotropy in polycrstalline or amorphous FM films, with detailed derivation for binary and ternary alloys. The single domain state of a thin film ferromagnetic element with uniaxial anisotropy,

$$E_a = K_u \cos^2 \phi \tag{2.1}$$

where E_a is the anisotropy energy, K_u is the uniaxial anisotropy constant, and ϕ is the angle between the magnetization and the easy-axis, is desirable in many applications. The magnetization in the element switches when the external field is applied along the easy-axis, as in magnetic memory devices, and rotates coherently and reversibly when the applied field is along the hard-axis, eliminating hysteresis loss when energy dissipation is the prior concern. For an infinitely large, stress-free, ideally magnetically soft polycrystalline or amorphous ferromagnetic alloy thin film, the crystal anisotropy and magnetostriction are negligible,

and the demagnetizing field will force the magnetization **M** to lie in the film plane. If an external magnetic field parallel to the film surface is applied during deposition or post-deposition annealing, a uniaxial anisotropy is induced, as explained by the pair ordering model [4, chap.17].

The simplest case is binary alloy A_xB_{1-x}. The basic assumptions are:

1. For a unit volume, the number of lattice sites is n, and z is the number of nearest neighbors (n.n.) for each lattice site. The **volume density** of **atomic pairs** is then

$$\frac{1}{2}nz$$

   The i**th direction** of atomic pair is determined by the position of the ith n.n., for $i = 1$ to $\frac{1}{2}z$. In each direction, there are **n** atomic pairs per unit volume.

2. The alloy is an ideal solid solution, and the probabilities of forming AA, BB, and AB pairs, P_{AA}, P_{BB} and P_{AB}, are determined solely by the concentrations of A and B atoms, C_A and C_B, since there are no differences in the chemical bonding energies.

$$P_{AA} = C_A^2 = x^2 \implies n_{AA} = \sum_{i=1}^{\frac{1}{2}z} n_{AAi} = \frac{1}{2}nz\ x^2$$

$$P_{BB} = C_B^2 = (1-x)^2 \implies n_{BB} = \sum_{i=1}^{\frac{1}{2}z} n_{BBi} = \frac{1}{2}nz\ (1-x)^2$$

$$P_{AB} = 2C_AC_B = 2x(1-x) \implies n_{AB} = \sum_{i=1}^{\frac{1}{2}z} n_{ABi} = nz\ x(1-x)$$

   where n_{AA} is the volume density of the AA pairs and n_{AAi} is the volume density of the AA pairs in the ith direction. **Note:** In each direction, $n_A = nx, n_B = n(1-x)$, but n_{AAi}, n_{BBi}, n_{ABi} are not determined by x only, but direction dependent. However, they satisfy the relation

$$n_{AAi} + n_{BBi} + n_{ABi} = n$$

$$n_{AAi} - n_{BBi} = (2x-1)n \implies n_{BBi} = n_{AAi} - (2x-1)n$$

$$\implies n_{ABi} = n - n_{AAi} - n_{AAi} + (2x-1)n = -2n_{AAi} + 2xn$$

3. l_{AA}, l_{BB}, l_{AB} are the coefficients of the pseudodipole interaction for different atom pairs. ϕ_i is the angle between the system magnetization and the ith direction.

In a unit volume, the anisotropy energy due to the directional distribution of the three kinds of atom pairs is given by

$$E_a = \sum_{i=1}^{\frac{1}{2}z} (n_{AAi} l_{AA} + n_{BBi} l_{BB} + n_{ABi} l_{AB})(\cos^2 \phi_i - \frac{1}{3})$$

Substitute the expressions for n_{BBi} and n_{ABi} obtained in assumption 2, we have

$$E_a = \sum_{i=1}^{\frac{1}{2}z} \{n_{AAi}[l_{AA} + l_{BB} - 2l_{AB}] + const.\}(\cos^2 \phi_i - \frac{1}{3})$$

With the definition

$$l_0 \equiv l_{AA} + l_{BB} - 2l_{AB}$$

, we have

$$E_a = \sum_{i=1}^{\frac{1}{2}z} n_{AAi} l_0 (\alpha_1 \gamma_{1i} + \alpha_2 \gamma_{2i} + \alpha_3 \gamma_{3i})^2 + const. \tag{2.2}$$

where (α_1, α_2, α_3) and (γ_{1i}, γ_{2i}, γ_{3i}) are the direction cosines of the domain magnetization and of the ith direction, respectively.

During field-sputtering or field-annealing, the atoms in the film gain a kinetic energy E_k from either the bombardment of the adatoms or the elevated temperature. The probability of finding AA pair in the ith direction is proportional to

$$\exp(-l_0 \cos^2 \theta_i / E_k)$$

, where θ_i is the angle between the ith n.n. direction and the applied field direction which is also the domain magnetization direction provided $H_{app} > H_{sat}$. Therefore, the volume density of AA pairs in the ith direction is given by

$$n_{AAi} = n_{AA} \frac{\exp(-l_0 \cos^2 \theta_i / E_k)}{\sum_{i=1}^{\frac{1}{2}z} \exp(-l_0 \cos^2 \theta_i / E_k)}$$

For $l_0 << E_k$, which means $-l_0 \cos^2 \theta_i / E_k \sim 0$,

$$\exp(-l_0 \cos^2 \theta_i / E_k) \sim 1 - l_0 \cos^2 \theta_i / E_k \sim 1$$

$$\Longrightarrow\ n_{AAi} = n_{AA}\frac{1 - l_0\cos^2\theta_i/E_k}{z/2} = \frac{2n_{AA}}{z}(1 - l_0\cos^2\theta_i/E_k)$$

$$= \frac{2n_{AA}}{z}[1 - l_0(\beta_1\gamma_{1i} + \beta_2\gamma_{2i} + \beta_3\gamma_{3i})^2/E_k], \tag{2.3}$$

where (β_1, β_2, β_3) is the direction cosines of the applied field.

From the analysis shown in the previous paragraph, it can be seen that the directional distribution of atom pairs is determined by the direction of the applied magnetic field. After the field-sputtering or annealing is completed, n_{AAi} is fixed. Now we can analyze the anisotropy energy of the system by evaluating equation 2.2, neglecting the constant term and substituting the directional distribution n_{AAi} given by equation 2.3.

$$E_a = \sum_{i=1}^{\frac{1}{2}z}\frac{2n_{AA}}{z}[1 - l_0(\beta_1\gamma_{1i} + \beta_2\gamma_{2i} + \beta_3\gamma_{3i})^2/E_k]l_0(\alpha_1\gamma_{1i} + \alpha_2\gamma_{2i} + \alpha_3\gamma_{3i})^2$$

$$= -\frac{n_{AA}l_0^2}{E_k}(k_1\sum_{i=1}^{3}\alpha_i^2\beta_i^2 + k_2\sum_{i>j}\alpha_i\alpha_j\beta_i\beta_j)$$

where [4, chap 17, p.364]

$$k_1 = \frac{2}{z}(\sum_{i}^{\frac{z}{2}}\gamma_{1i}^4 - \sum_{i}\gamma_{1i}^2\gamma_{2i}^2)$$

$$k_2 = \frac{8}{z}(\sum_{i}^{\frac{z}{2}}\gamma_{1i}^2\gamma_{2i}^2)$$

and k_1 and k_2 are merely determined by the crystal type.

$\mathbf{Ni}_{1-x}\mathbf{Fe}_x$

In our polycrystalline films, with Fe substituting in the *fcc* Ni lattice, the atoms are typically arranged in a columnar growth along the $< 111 >$ direction, where the $\{111\}$ planes are the close-packed planes. However, the in-plane orientation of each columnar grain is random, resulting in a film which is isotropic in the film plane. The values of k_1 and k_2 for isotropic material are 2/15 and 4/15 respectively, which leads to the following form of the anisotropy energy in the form of Eq. 2.1:

$$E_a = -\frac{2\times\frac{1}{2}nz\ x^2l_0^2}{15E_k}(\sum_{i=1}^{\frac{z}{2}}\alpha_i\beta_i)^2$$

$$= -\frac{nz\ x^2 l_0^2}{15E_k}\cos^2\varphi$$

where φ is the angle between the domain magnetization and the direction of the sputtering field.

Finally, the uniaxial anisotropy constant induced by field-sputtering or annealing is given by

$$K_u = \frac{nzl_0^2}{15}\frac{1}{E_k}x^2$$

where x is the atomic percentage of the Fe atoms. Taking $z = 12$, $n = 9.17 \times 10^{28}$ m^{-3}, $nl_0 = 2.7 \times 10^6$ J m^{-3}, $E_k = 9.66 \times 10^{-21}$ J, we have $K_u = 2600$ erg cm^{-3} for $x = 0.2$, *i.e.* the composition of Permalloy ($Ni_{80}Fe_{20}$). Using the equation $H_k = 2Ku/M_s$, we have an induced uniaxial anisotropy field $H_k \sim 3$ Oe, which is consistent with our hysteresis loop measurements in the Permalloy thin films.

The induced anisotropy for Ni-rich Fe alloy peaks at a maximum concentration of the dilute atom species Fe 50%. However, the concentration of Fe is typically fixed at values around 20% for soft magnetic properties since the crystal anisotropy and magnetostriction pass through 0 at this composition. In order to increase the anisotropy of the film at this composition, it is necessary to introduce a third impurity element without varying the ratio of Ni/Fe atoms. This expression for uniaxial anisotropy also implies that the anisotropy energy decreases with increasing kinetic energy of the adatoms, provided $l_0 << E_k$. However, higher kinetic energy gives a more homogeneous film and smoother surface, which will give a higher quality film with lower coercivity along the hard-axis, if we consider the ripple issue. Therefore, a balance between these two factors should be reached for actual deposition conditions optimization.

CoZrTa, CoFeB, NiFeTb

The treatment for ternary alloys uses the same principles as in the binary alloy case, but with greater complexity [5]. With the addition of a third impurity element, the composition of the alloy becomes $(A_xB_{1-x})_{1-y}C_y$. Instead of considering only one kind of different-atom

pair AB in a binary system, three combinations have to be treated: AB, BC and AC. Therefore, we define

$$l_0^{AB} \equiv l_{AA} + l_{BB} - 2l_{AB}$$

$$l_0^{BC} \equiv l_{BB} + l_{CC} - 2l_{BC}$$

$$l_0^{AC} \equiv l_{AA} + l_{CC} - 2l_{AC}$$

For $(\mathrm{A}_x\mathrm{B}_{1-x})_{1-y}\mathrm{C}_y$, the volume density of atoms and atomic pairs in the ith direction satisfies the following relations, where n is the volume density of the lattice sites:

$$n_A = n(1-y)x$$

$$n_B = n(1-y)(1-x)$$

$$n_C = ny$$

note that n_A, n_B and n_C are constants for fixed composition.

$$2n_{AAi} + n_{ABi} + n_{ACi} = 2n_A \tag{2.4}$$

$$2n_{BBi} + n_{ABi} + n_{BCi} = 2n_B \tag{2.5}$$

$$2n_{CCi} + n_{ACi} + n_{BCi} = 2n_C \tag{2.6}$$

Solving the above equations, we have

$$n_{ABi} = -n_{AAi} - n_{BBi} + n_{CCi} + const.$$

$$n_{ACi} = -n_{AAi} + n_{BBi} - n_{CCi} + const.$$

$$n_{BCi} = n_{AAi} - n_{BBi} - n_{CCi} + const.$$

Thus the anisotropy energy in a unit volume due to the directional distribution of the six kinds of atom pairs is given by

$$E_a = \sum_{i=1}^{\frac{1}{2}z}(n_{AAi}l_{AA} + n_{BBi}l_{BB} + n_{CCi}l_{CC} + n_{ABi}l_{AB} + n_{ACi}l_{AC} + n_{BCi}l_{BC})(\cos^2\phi_i - \frac{1}{3})$$

$$= \sum_{i=1}^{\frac{1}{2}z}\frac{1}{2}[(n_{AAi} + n_{BBi} - n_{CCi})(l_{AA} - 2l_{AB} + l_{BB}) + (n_{AAi} - n_{BBi} + n_{CCi})(l_{AA} - 2l_{AC} + l_{CC})$$

$$+(-n_{AAi}+n_{BBi}-n_{CCi})(l_{BB}-2l_{BC}+l_{CC})](\cos^2\phi_i-\frac{1}{3})$$

$$=\sum_{i=1}^{\frac{1}{2}z}\frac{1}{2}[(n_{AAi}+n_{BBi}-n_{CCi})l^0_{AB}+(n_{AAi}-n_{BBi}+n_{CCi})l^0_{AC}+(-n_{AAi}+n_{BBi}+n_{CCi})l^0_{BC}](\cos^2\phi_i-\frac{1}{3})$$

$$=\frac{1}{2}\sum_{i=1}^{\frac{1}{2}z}n_{AAi}(l^0_{AB}+l^0_{AC}-l^0_{BC})(\cos^2\phi_i-\frac{1}{3})$$

$$+\frac{1}{2}\sum_{i=1}^{\frac{1}{2}z}n_{BBi}(l^0_{AB}-l^0_{AC}+l^0_{BC})(\cos^2\phi_i-\frac{1}{3})$$

$$+\frac{1}{2}\sum_{i=1}^{\frac{1}{2}z}n_{CCi}(-l^0_{AB}+l^0_{AC}+l^0_{BC})(\cos^2\phi_i-\frac{1}{3})$$

which is in the exact mathematical form of Eq. 2.2 but with different l parameters and dependence on the three same-atom pair densities. Using the same derivation line as in the case of $Ni_{1-x}Fe_x$, we arrive at the final expression for K_u in the ternary alloy system $(A_xB_{1-x})_{1-y}C_y$:

$$E_a=-\frac{2}{15E_k}[n_{AA}(l^0_{AB}+l^0_{AC}-l^0_{BC})+n_{BB}(l^0_{AB}-l^0_{AC}+l^0_{BC})+n_{CCi}(-l^0_{AB}+l^0_{AC}+l^0_{BC})]\cos^2\phi$$

where

$$n_{AA}=n_A^2=x^2(1-y)^2$$

$$n_{BB}=n_B^2=(1-x)^2(1-y)^2$$

$$n_{CC}=n_C^2=y^2$$

assuming an ideal solid solution.

If A substitutes the B matrix sites at a fixed ratio and C is added as dilute impurities, the uniaxial anisotropy energy shows a parabolic dependence on the impurity concentration $K_u \propto ay^2+by$, where the constants a and b are determined by the A/B atom concentration and the pseudodipolar constants for the different atom pairs. For a dilute impurity concentration value in the range of 0 to 1% and a, b at the same order of magnitude, the experimental data might be fitted as a linear dependence because of the small y value, in which case $y^2 \ll y$. See Fig. 2.3 [6].

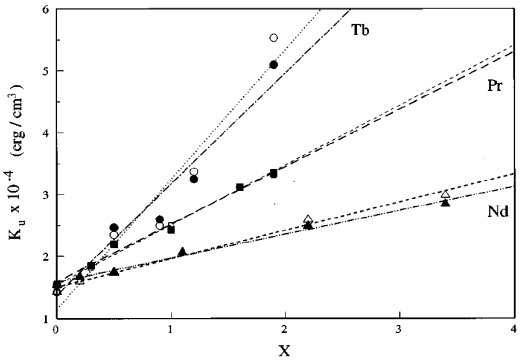

Figure 2.3: Figure from Ref. [6], *Induced and local anisotropies in amorphous CoZr-rare earth thin films containing Pr, Nb and Tb.* Rare earth concentration dependence of the in-plane uniaxial anisotropy K_u of amorphous $(Co_{93}Zr_7)_{100-x}RE_x$ thin films, showing a linear trend at low doping levels.

2.2.2 Permeability and initial susceptibility

For high frequency applications, the ferromagnetic film often operates under moderate external fields on the order of Oe (1×10^{-4} T). Therefore, besides the permeability, which is defined by the major loop where the magnetization is cycled between the opposite saturated magnetization directions, the initial susceptibility is of significant importance. It is defined as the susceptibility in the vicinity of zero external field:

$$\chi_{init} = (\frac{\partial M}{\partial H})_{H=0}.$$

• The Stoner-Wohlfarth Model, Reversible Coherent Rotation

In a single-domain, uniaxially anisotropic ferromagnetic thin film element, the magnetization lies spontaneously along the easy-axis. If an external magnetic field is applied at an angle θ_0 with respect to the easy-axis, the magnetization rotates away from the easy-axis as the amplitude of the field H increases, to minimize the free energy of the system. The equilibrium state is illustrated in Fig. 2.4: The unit volume free energy of the system is

$$E = -K_u \cos^2(\theta - \theta_0) - M_s H \cos\theta$$

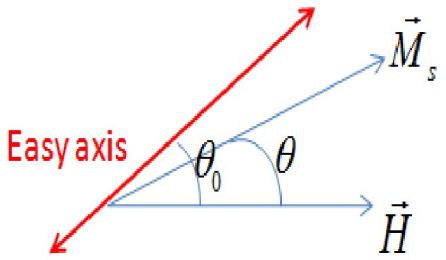

Figure 2.4: Equilibrium orientation of the magnetization under external bias in a system with uniaxial anisotropy, Stoner-Wohlfarth(single domain) model. θ is the angle between the magnetization direction and the bias field; θ is the angle between the bias field and the easy-axis.

and at equilibrium θ,

$$M = M_s \cos\theta$$

$$\frac{\partial E}{\partial \theta} = K_u \sin 2(\theta - \theta_0) + M_s H \sin\theta = 0 \tag{2.7}$$

For the small applied field limit, the magnetization lies almost parallel to the easy-axis, forming a small angle of

$$\delta\theta = \theta_0 - \theta \sim 0$$

$$\sin\delta\theta \sim \delta\theta$$

Then equation 2.7 becomes

$$-2K_u\delta\theta + M_s H \sin\theta_0 = 0 \Rightarrow \delta\theta = \frac{M_s H}{2K_u}\sin\theta_0$$

The initial susceptibility is then

$$\chi = (\frac{\partial M}{\partial H})_{H=0}$$
$$= (\frac{M_s \partial \cos\theta}{\partial H})_{H=0}$$
$$= -M_s \sin\theta_0 \frac{\partial\theta}{\partial H}$$
$$\frac{\partial\theta}{\partial H} = -\frac{\partial\delta\theta}{\partial H} = -\frac{M_s}{2K_u}\sin\theta_0$$

Therefore we have $\chi_{init} = \frac{M_s^2}{2K_u}\sin^2\theta_0$, as illustrated in Fig. 2.5. We could see that for coherent magnetization rotation, the initial susceptibility reaches its maximum along the

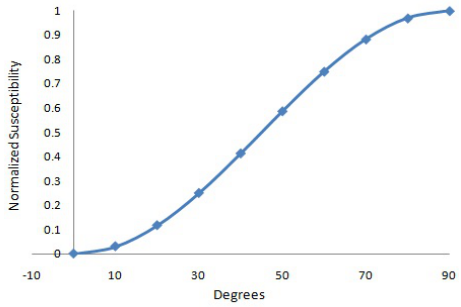

Figure 2.5: The initial susceptibility χ_{init} as a function of the angle θ_0 between the easy-axis and the external field.

hard-axis.

• **Reversible 180° domain wall motion**

If the system is not single-domain, domain walls exist at the boundaries of the multiple magnetic domains. The domain wall energy varies as a function of the position S of the wall, due to the inhomogeneity of the system [7, chap.4]. Local impurities or defects introduce additional energy terms to the wall and cause energy fluctuations, as illustrated in Fig. 2.6 (a). In the vicinity of a local energy minimum, where the small-field limit applies, the domain wall energy per unit area can be approximated in a parabollic form as illustrated in Fig. 2.6 (c), $\epsilon_w = \frac{1}{2}\alpha s^2$, where s is the displacement from the equilibrium position. In the case of 180° domain walls, the magnetizations adjacent to the wall on either side are antiparallel along the easy-axis. Under an applied bias field, for a domain wall displacement s from the equilibrium position, the change in the total magnetic moment is

$$\Delta M = 2M_s A s$$

where M_s is the saturation magnetization and A is the domain wall area. This leads to a reduction in the Zeeman energy of the system,

$$\Delta E = MH = 2M_s A s H \cos\theta$$

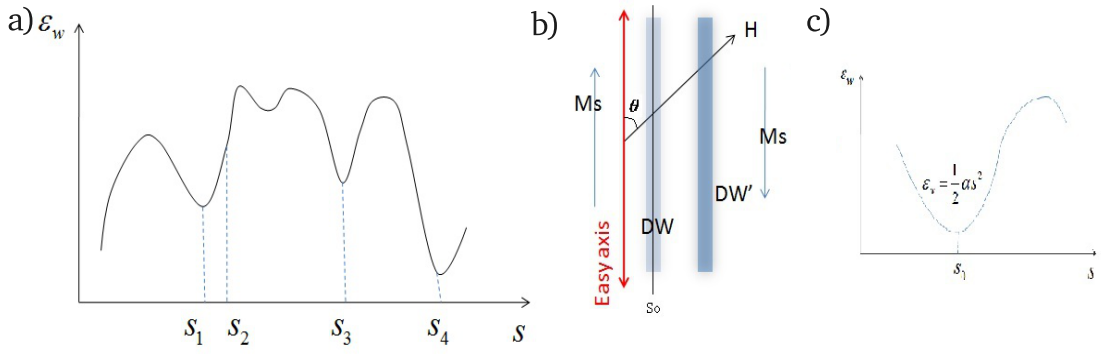

Figure 2.6: (a)Illustration of the fluctuation in the 180° domain wall energy as a function of the wall position, due to local impurities and defects; (b) diagram of the configuration of the system, where θ is the angle between the applied field and the easy-axis, S_0 is the equilibrium position of the 180° domain wall under zero bias, DW' represents the displacement of DW when the field H is applied, and M_s across the DW are antiparallel along the easy-axis; (c) the parabolic approximation of the domain wall energy in vicinity of the equilibrium position.

We define a pseudo-pressure exerted by the applied field on the domain wall,

$$p = \frac{\Delta E/s}{A} = M_s H 2\cos\theta$$

The total energy per unit volume of the system is then

$$\epsilon = \epsilon_w + \epsilon_H = \epsilon_w - pA$$

with the equilibrium criterion

$$\frac{\partial \epsilon}{\partial s} = \alpha s - 2M_s H\cos\theta = 0$$

which gives the equilibrium domain wall displacement in the small-field limit

$$s = \frac{2M_s\cos\theta}{\alpha} H$$

leading to a change in the magnetization of

$$\Delta M = \frac{4M_s^2\cos^2\theta}{\alpha} AH.$$

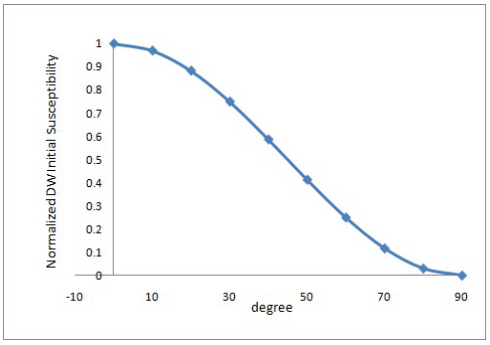

Figure 2.7: The initial susceptibility χ_{init} of the 180° domain wall as a function of the angle θ between the external field and the easy-axis.

Therefore we have the expression of the initial susceptibility due to the motion of the 180° domain wall:

$$\chi_{init} = \frac{2M_s \cos\theta}{\alpha} A$$

which is plotted in Fig. 2.7 and reaches its maximum when the external field is applied along the easy-axis.

• **Reversible 90° domain wall motion**

Similar analysis applies to the 90° domain wall case, resulting in

$$p = M_s H(\cos\theta_1 - \cos\theta_2)$$

$$\frac{\partial \epsilon}{\partial s} = \alpha s - 2M_s H(\cos\theta_1 - \cos\theta_2) = 0$$

$$\chi_{init} = \frac{4M_s^2(\cos\theta_1 - \cos\theta_2)^2}{\alpha} A$$

The system configuration and the initial susceptibility as a function of the external field orientation are illustrated in Fig. 2.8 (a) and (b), respectively.

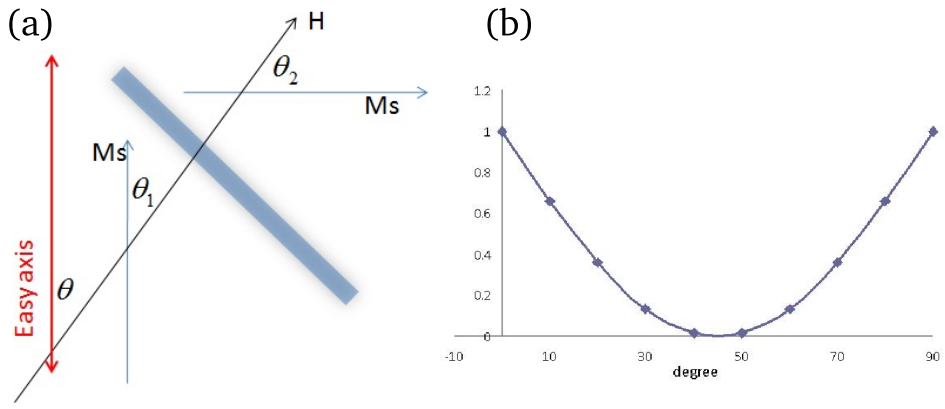

Figure 2.8: (a) diagram of the configuration of the system, where θ is the angle between the applied field and the easy-axis, θ_1 and θ_2 are the angles between the applied field and domain 1 and domain 2, respectively; (b) the initial susceptibility χ_{init} of the 90° domain wall as a function of the angle θ between the external field and the easy-axis.

2.2.3 Coercive field

First we consider the hard-axis coercivity, which is more important in applications requiring high initial susceptibility. In the Stoner-Wohlfarth model, the magnetization in the system under investigation is strictly uniform and therefore, the switching of **M** along the hard-axis is due to the reversible, coherent rotation of **M**, which predicts zero coercivity as **M** lies along the easy-axis at zero bias. However, in realistic thin film systems, fluctuations in the local magnetic or microstructural properties are inevitable. As illustrated in Fig. 2.9 [3], if a film is saturated under an external field along the hard-axis and then the field is reduced to zero, due to the inhomogeneous distribution of the easy-axis in the extended film area, the film will be devided into stripe domains along the average easy-axis but with slightly dispersive orientations. The domain walls between adjacent domains contain magnetization oriented in the hard-axis and introduce the remanence magnetization. Based on this scenario of the hard-axis coercivity, we conclude that H_c^{hard} could be reduced if we eliminate the area density of the domain walls in the thin film system.

On the other hand, the Stoner-Wohlfarth model predicts the easy-axis coercivity

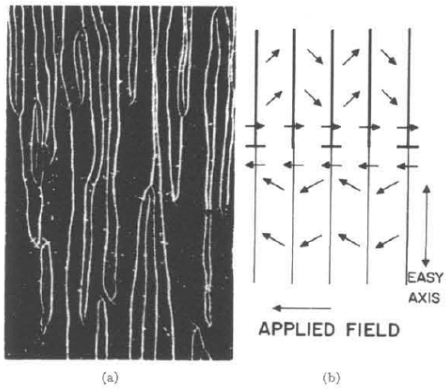

Figure 2.9: From Fig. 2 of Ref. [3]. (a) Bitter pattern of partially switched hard-axis remanent state. (b) Interpretation of the pattern in (a), note the crosstie domain walls.

to be the same value as the anisotropy field H_k, again due to the coherent rotation of the magnetization **M** but irreversible. In realistic magnetically soft thin film systems, the easy-axis coercivity H_c^{easy} is in most cases significantly lower than the anisotropy field H_k. As mentioned multiple times before, the single-domain configuration is extremely difficult to achieve under moderate bias field values and the switching of the magnetization does not occur as the coherent rotation of **M** but via the nucleation of reversed domains and then their propagation through the whole film by domain wall motion. The coercive field H_c along the easy-axis is thus determined by the reversed domain nucleation field and the de-pinning field of the domain walls. In a semi-infinite extended thin film with various inhomogeneities, the reversed domain nucleation is probable. Therefore, the de-pinning field of the domain walls is the dominant influence on H_c^{easy} [7, chap.7]. The pinning of the domain walls occurs both in the bulk and at the surface/interface of the thin film system. The bulk contribution comes from the intrinsic fluctuations of exchange and local anisotropy energy, which causes ripple domains in the hard-axis case, as discussed above, and the internal stress sources originating from dislocations, grain boundaries, impurity atoms and agglomeration of vacancies. The surface/interface contribution comes from the irregularities on the surface, *i.e.* the film roughness, as domain wall energy depends on the

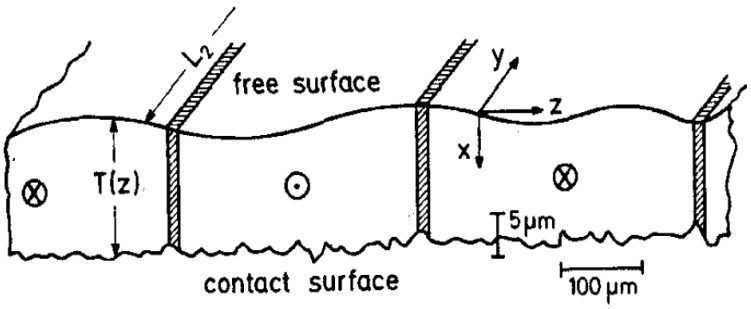

Figure 2.10: From Fig. 7.10 of Ref. [7]. Domain walls in a ribbon with fluctuating thickness $T(y,z)$; L_2 is the length over which the planar domain wall extends.

wall area which fluctuates with the thickness of the film.

The magnetically soft metallic FM films of the greatest interest for device are either amorphous or nanocrystalline with near-zero magnetostriction. Therefore, in the systems considered in this thesis, the surface roughness has the dominant influence on the easy-axis coercivity. As illustrated in Fig. 2.10, the planar domain wall extending the length L_2, parallel to the y-axis, has a total wall energy

$$\epsilon^w(z) = \gamma_w L_2 \langle T(z) \rangle$$

where γ_w is the area energy of the domain wall and $\langle T(z) \rangle$ is the averaged film thickness in the y-direction. The force acting on the wall is then given by

$$P_{surf} = -\gamma_w L_2 \frac{d\langle T(z) \rangle}{dz}$$

Using a sinusoidal ansatz

$$\langle T(z) \rangle = \langle T \rangle + \Delta T \sin(2\pi z/\lambda)$$

where λ is the wavelength of the thickness fluctuation and ΔT is the amplitude of the irregularities, we have the expression for the easy-axis coercivity H_c^{surf} found in the limit of dominant surface/interface roughness [7, Chap.7.2, P.163]:

$$\mu_0 H_c^{surf} = \frac{\pi}{M_s} \frac{\Delta T}{\langle T \rangle} \rho_s^{1/2} \gamma_w (\frac{L_2}{2\lambda})^{1/2} (ln \frac{L_3}{2L_0})^{1/2}$$

where ρ_s is the are density of the 2-D distribution of pinning centers, L_3 is the domain width and L_0 is the average wavelength of the pinning potential. Thie expression indicates that H_c^{surf} should exhibit a linear dependence on the film roughness ΔT and the inverse of the film thickness $1/\langle T \rangle$.

In conclusion, the coercivity along both the easy- and hard-axes could be reduced if the film homogeneity is enhanced, both in the bulk and at the surface.

2.3 Kinetics of magnetron sputtering and thin film growth

Sputtering has the advantages of high deposition rate and low substrate temperature compared with other deposition techniques, and is ideal for depositing polycrystalline or amorphous films spanning the thickness range of a few nm to several μm, which is dominant in the magnetic recording industry. We use this technique for all the thin-film samples considered in this thesis, so it is crucial to understand the relationship between the microstructure of the thin films and the sputtering process for optimization of magnetic properties.

2.3.1 Magnetron sputtering

Fig. 2.11 illustrates the configuration of our UHV magnetron sputtering system with the base pressure 2×10^{-9} Torr. The substrate is separated from the targets by about 10 cm and the Ar pressure is kept at the mTorr range with a minimum of ~ 1 mTorr, which allows for a relatively long mean free path (~ 4 cm) for the sputtered atoms in the Ar working gas. The right panel illustrates the structure of the plasma and shows the high voltage across the sputtering gun shield and the target, which acceclerates the Ar^+ ions for bombardment of the target. 'Magnetron' refers to the ring permanent magnet, embeded in the sputtering gun, which generates the magnetic field at the surface of the target, illustrated by the red curves at the lower left of Fig. 2.11. The magnetic field exerts a Lorentz force ($e\mathbf{v} \times \mathbf{B}$) on the electrons in the plasma, which traps the electrons in the green trajectory. Because of the enhanced electron density and consequently the enhanced collision rate between particles

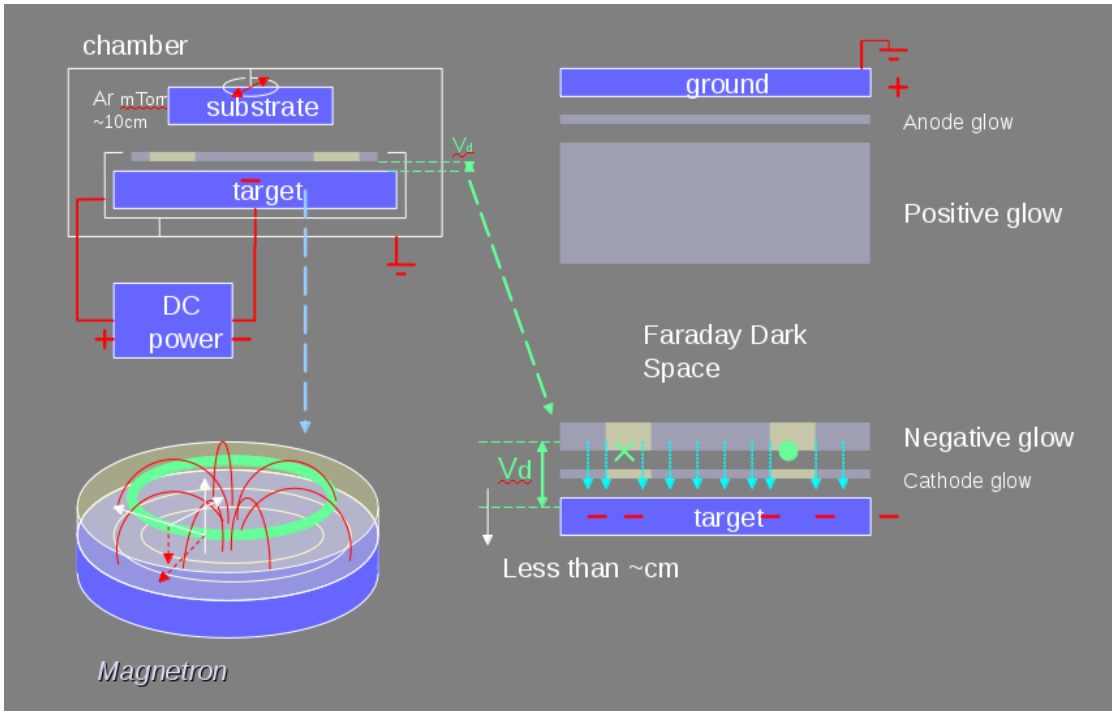

Figure 2.11: Diagram of the magnetron sputtering system.

in the vicinity of the target surface, the plasma could be maintained at sufficiently low Ar pressure to avoid thermalization of sputtered atoms in the UHV chamber.

Fig. 2.12 (a) illustrates the sputtering process at the target. The Ar^+ ions are accelerated by the sputtering voltage V_d between the sputtering gun shield, which is grounded, and the sputtering gun, which is negatively biased by a high voltage source. During collisions, an electron tunnels from a low-velocity neutral Ar atom to an accelerated Ar^+ ion and thus creates a fast neutral. The fast neutrals and accelerated ions collide with the target, importing momentum to the atoms in the target; some atoms escape the target surface provided they gain enough recoil energy from other atoms to overcome the surface energy barrier, which is in the range of several eV. The average kinetic energy of the sputtered atoms is given by

$$E = U_s \ln(\gamma \frac{E_{ion}}{U_s}) - U_s \tag{2.8}$$

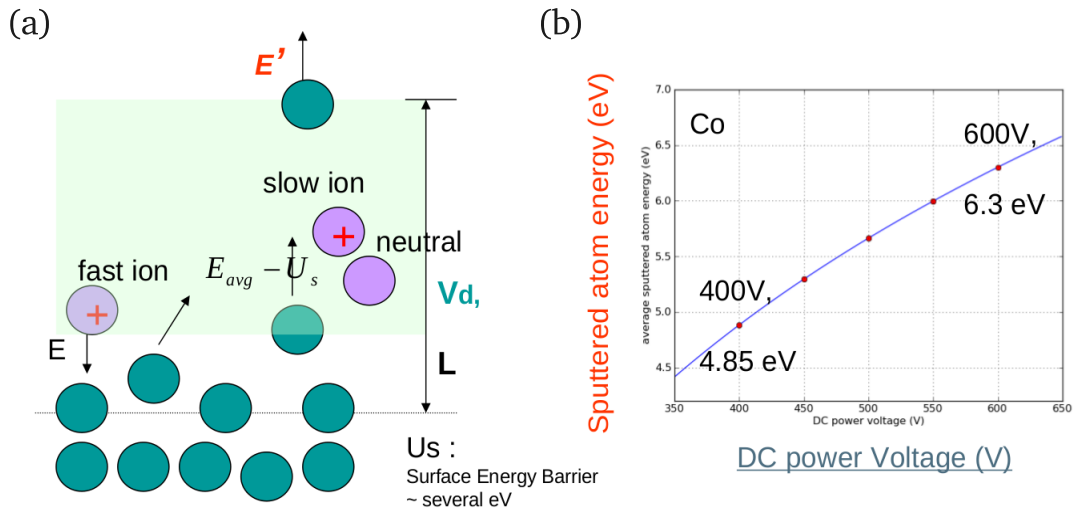

Figure 2.12: Sputtering kinetics at the target: (a) incoming Ar^+ ions and sputtered target atoms; (b) the kinetic energy of the sputtered atoms as a function of the sputtering voltage for Co under Ar plasma, calculated according to Eq. 2.8.

where U_s is the surface energy barrier for the atoms to escape from the target, $\gamma = (4M_1M_2)/(M_1 + M_2)^2$ with M_1 and M_2 being the incident and sputtered particle mass respectively, and E_{ion} is the incident Ar^+ ion energy (proportional to the sputtering voltage). This equation gives average sputtered Co atom energies of 4.85 eV and 6.3 eV under sputtering voltages of 400 V and 600 V, respectively, as illustrated in Fig. 2.12 (b).

Fig. 2.13 (a) describes the deposition of the sputtered target atoms on the substrate surface. The adatoms arriving at the film surface are first thermally accomodated with the substrate and then diffuse in the film. Because of the low substrate temperature in magnetron sputtering, the diffusion of the adatoms is the consequence of the incoming kinetic energy and the bombardment of the back-reflected Ar neutrals on the film surface. The diffusion length after the adatom's arrival at the film surface is determined by the surface diffusivity and the time interval of the subsequent adatoms arrival, inversely proportional to the deposition rate. The adatom is then frozen in the film by subsequent adatoms. In Fig. 2.13 (b), the dependence of the film roughness is plotted as a function of the bom-

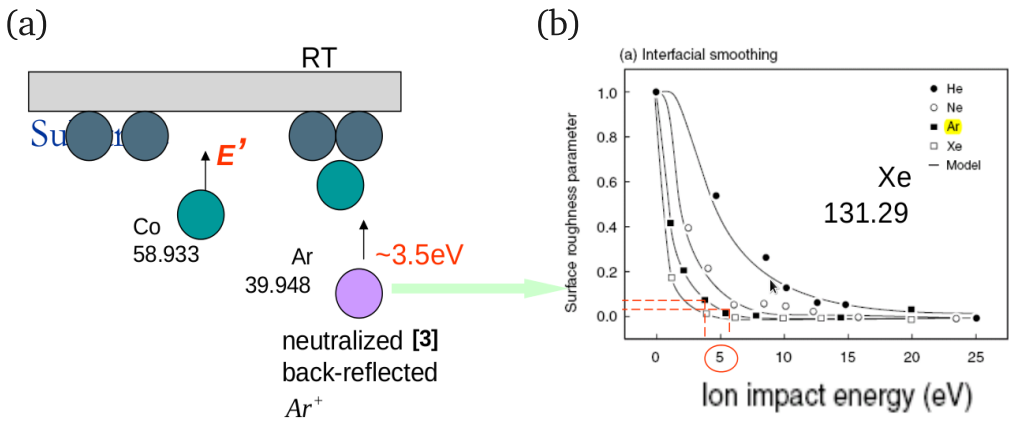

Figure 2.13: Sputtering kinetics at the substrate: (a) adatoms and back-reflected Ar neutrals at the sample surface; (b) surface roughness as a function of the impact energy of the bombarding particles, from ref. [8].

barding ion kinetic energy, calculated in ref. [8]. In Fig. 2.12 (b), we calculated the kinetic energy of the sputtered Co atoms to be in the range of ∼5 eV, and the neutralized back-reflected Ar^+ to be ∼3.5 eV. Finding these values in the plot for Ar bombarding ions, we find an approximately linear regime where *the surface roughness decreases with increasing ion impact energy.*

Summary: We have found, according to kinetic models of the sputtering process, that for the range of sputtering parameters considered, 1) adatom energy increases roughly linearly with sputtering voltage; 2) surface roughness is expected to decrease roughly linearly with adatom energy. These two observations help us infer a *decreasing* film roughness with *increasing* sputtering bias voltage. This model will be important in the experiments in *Chapter 3.*

2.3.2 Film growth, the thickness dependence

As illustrated in Fig. 2.14 (a) and (b), the growth of the film in the sputtering process is in *Zone T* with surface difussion and columnar growth. Columnar growth introduces surface roughness and film inhomogeneity above a critical thickness where the film is par-

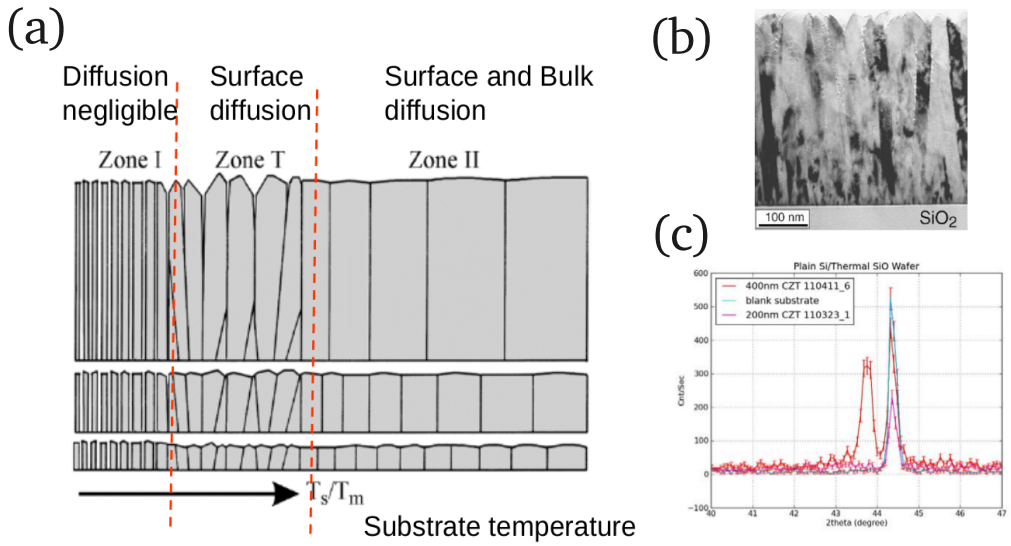

Figure 2.14: Thin film growth: (a) the temperature and thickness dependence of the film growth, from Ref. [9]; (b) experimental data corresponding to (a), from Ref. [10]; bright-field XTEM micrograph, TiN film deposited by magnetron sputtering in a pure N_2 atmosphere (20 mTorr) on amorphous SiO_2 at 350°C; (c) appearance of additional Co XRD peak in the 400 nm CoZrTa film indicating crystallization.

tially crystalized. We observe this crystallization in our thickest (400 nm) CoZrTa film, which is amorphous in the thin film form. Fig. 2.14 (c) shows that in the 200 nm CoZrTa sample there is only the Si x-ray diffraction (XRD) peak while in the 400 nm CoZrTa film an additional Co peak appears.

2.4 Field-sputtering: *in-situ* quadrupole electromagnet

With some understanding of the physical origins of soft magnetic properties in thin films, we next look into some experimental aspects of materials processing and characterization. Here we describe the *in-situ* quadrupole electromagnet specially designed for field-sputtering and demonstrate its effects on deposited FM thin films. One specific application of this technique is depositing the magnetic core for integrated inductors. Inductors are indispensible components in high-frequency electronics. The inductance hancement of integrated inductors have long been limited by the inability of flux to close on a high- μ path in finite structures with magnetization along surface or edge normals. In order to maximize the inductance density, a toroidal core geometry which closes flux within the structure, as shown in Fig. 2.15, can be adapted [11], requiring a high-permeability core material with isotropic magnetic properties. This is a challenge because typical soft magnetic materials have only a single high-μ axis, as shown in Fig. 2.16. Here we are developing isotropic high-μ multilayers, consisting of alternating metallic ferromagnetic (FM) layers and ultra-thin insulators, for use in high inductance density, high Q-factor next-generation integrated inductors operating at 100-500 MHz. Our unique quadrupole electromagnet in the sputtering chamber provides a magnetic field synchronized with sample rotation, inducing a well-defined uniaxial anisotropy in individual FM layers with designated angle, allowing the rotation of anisotropy in subsequent FM layers and thus yielding a nearly isotropic multilayered core.

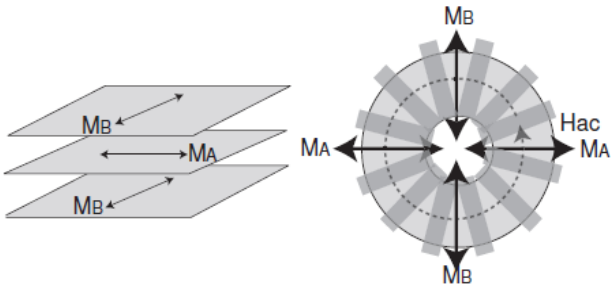

Figure 2.15: Toroidal isotropic magnetic core for an integrated inductor, consisting of multiple FM layers separated by dielectric layers. The uniaxial anisotropy in each FM layer rotates through the laminated structure, producing an isotropic core.

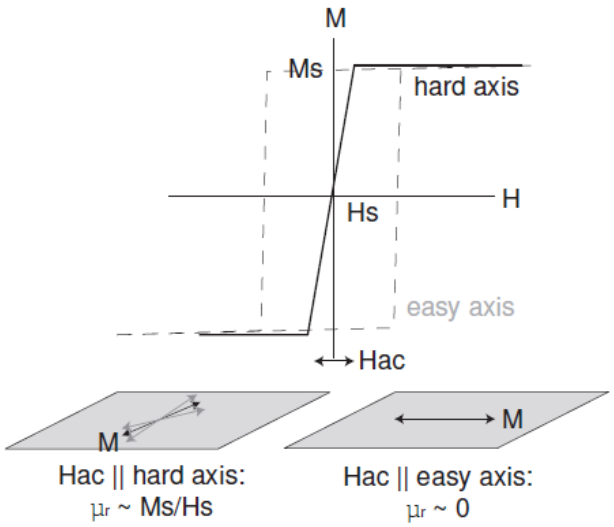

Figure 2.16: Ac permeability along the hard- and easy-axes in a thin film, showing high permeability along the hard-axis and zero permeability along the easy-axis.

2.4.1 Introduction to field-sputtering

Field-sputtering is the most important step for optimizing soft magnetic thin films in various applications and has severe limitations in its usual configuration. In this section, we demonstrate the incorporation of a quadrupole electromagnet into our ultra-high vacuum (UHV) sputtering system, enabling vector control of induced magnetic anisotropy in specific layers of magnetic thin-film heterostructures [12]. The stationary quadrupole electromagnet is used to generate a magnetic field which rotates synchronously with the physical axes of the substrate *in-situ* during sputtering. An arbitrary anisotropy direction can be set for successive ferromagnetic layers by adjusting the phase difference between the rotation of the substrate and the external field. The ability to rotate the substrate during deposition and change anisotropy without breaking vacuum enables the deposition of magnetically soft heterostructures with arbitrary in-plane anisotropy axes. These structures have so far proven useful for the generation of high, isotropic μ toroidal inductor geometries [13, 14].

Well-defined magnetic anisotropy is a critical property for soft magnetic materials used in a wide range of applications, including but not limited to thin-film magnetic recording heads [15], magnetic random access memory [16], on-chip magnetic field sensors [17–19], and power management devices [20,21]. As these applications continuously seek higher sensitivity, smaller device sizes and lower power dissipation, respectively, the magnetic thin films included require more nearly-ideal soft magnetic properties. Near-zero coercive field (H_C) and high magnetic permeability (χ_m) along particular axes of the devices are desirable.

To induce uniaxial or unidirectional anisotropy in an alloy ferromagnetic thin film, either amorphous or polycrystalline, deposition or postannealing in the presence of a magnetic field is generally required [22, 23]. Deposition in magnetic field saves a process step and is advantageous for multilayers or device structures which are temperature-sensitive. The external magnetic field during sputtering is often applied by a permanent magnet assembly fixed to the sample stage, which rotates to ensure the uniformity of the deposited (typically sputtered) film [23]. It is then difficult, if not impossible, to change the direction

of anisotropy in different layers of a laminated structure without breaking vacuum. Raanaei *et al.* [24] have rotated anisotropy *in-situ* manually, with a wobble stick, by repositioning the sample on a permanent magnet plate. This approach is prohibitively cumbersome for structures with more than one or two anisotropy rotations [17, 25] and could not easily be adapted for production. A structure with variable anisotropy axes in successive films could be interesting for both fundamental and applied sciences; Zohar *et al.* [26] used orthogonal induced anisotropy in ferromagnetic(FM)/non-magnetic(NM)/ferromagnetic(FM) structures to search for a hallmark of the spin pumping effect; in a device proposed by Frommberger *et al.* [11], it functions as the isotropic magnetic core of a toroidal thin-film inductor in on-chip DC-DC converters.

Here we present a new technique to achieve vector control of magnetic anisotropy in the layers of magnetic heterostructures. We apply an external magnetic field during sputtering using a UHV compatible quadrupole electromagnet with two pairs of coils. The magnitude of the field can be adjusted easily through the amplitude of bipolar, sinusoidal currents running through the coils; the direction of the field is determined by the phase of the sinusoid. To ensure that the angle between the sample and the field is fixed for an individual layer during sputtering, rotation of the field direction is synchronized with the physical rotation of the sample. This approach enables integration of precise anisotropy control into automation of the sputtering process, making it possible to sputter complex multilayered magnetic structrures with engineered anisotropy.

2.4.2 Instrumentation

The layout of our six-target UHV magnetron sputtering chamber with the *in-situ* quadrupole electromagnet installed is illustrated in Fig. 2.17(a). Base pressure of the cryopumped chamber is 2×10^{-9} Torr without baking. During sputtering, the sample sits at the center point of the chamber, facing down. The targets are arranged at the bottom of the chamber in a fourfold symmetric manner, each inclining towards the focal point at a 30° angle from

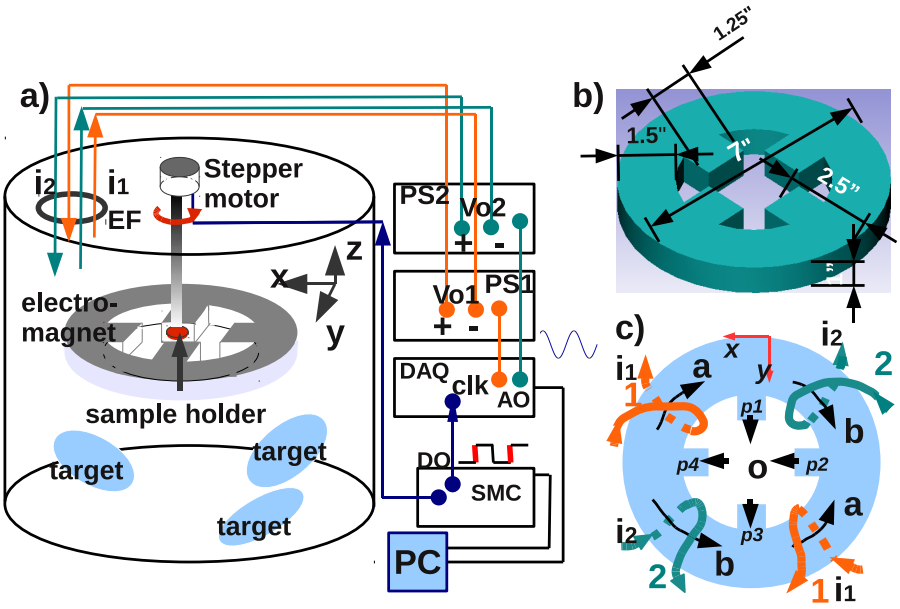

Figure 2.17: (a) Layout of the field sputtering system; FE: electrical feedthrough for the coils of the electromagnet, 2 3/4" conflat flange (CF); PS2, PS1: bipolar power supplies (Kepco BOP 20-20M) for coil pairs 2 and 1, respectively; DAQ: MIO DAQ (NI 6212); (b) shape and dimensions of the silicon steel core (4% Si, Scientific Alloys); (c) coils arrangement of the electromagnet and magnetic flux in the core.

the cylindrical axis, in a confocal 'sputter-up' geometry. The adatoms flux from an individual target will be slightly nonuniform across the surface of the substrate. To ensure the homogeneity of the sputtered film, physical rotation of the sample stage is necessary. The rotation is controlled by the combination of a stepper motor and motor contoller. While the electromagnet is fixed to a top flange of the chamber (using 'groove grabbers') and remains stationary, the magnetic field it generates can rotate by phasing sinusoidal currents through the coils of a quadrupole electromagnet (described in the following paragraphs). We use a National Instruments multiple IO data acquisition device (NI6212, 'DAQ' in Fig. 2.17(a) to communicate between the power supplies to the coils ('PS1', 'PS2' in Fig. 2.17(a) and the stepper motor controller ('SMC' in Fig. 2.17(a), and synchronize the rotating magnetic field with the physical rotation of the sample.

We use a Lin Engineering 5718M high torque stepper motor to rotate the sample. The motor is installed on top of the chamber via a 2 3/4" conflat flange (CF) magnetically-coupled rotary feedthrough (Thermionics FRMRE-275-38/MS-EDR) which is mounted on a linear translator with 2" of z travel (Thermionics Z-B275C-T275T-1.53-2). The sample stage is attached to the end of the motor shaft. The programmable Thermionics TMC 1-C motor controller controls the stepper motor, at 800 steps per cycle with a designated angular speed. The motor controller has 11 user I/Os (digital or analog), and one of them is programmed to change the digital output level between high and low every 5 steps, sending out a square wave with 80 rising edges for each full rotation of the motor. This digital pulse train is sent to the PFI0 terminal ('clk' in 'DAQ', Figure 1 a) on the DAQ NI6212. The PFI0 terminal is a digital input channel used for the timer input. The clock rate in NI6212 is therefore determined by the rotation speed of the sample stage; and for each rotation of the motor, 80 clock pulses occur.

To implement field sputtering, we apply the external magnetic field using the electromagnet with a quadrupole silicon steel core (4% Si Fe, Scientific Alloys) and 2 pairs of coils (4 coils total), as specified in Fig. 2.17(b) and (c). Each coil has approximately 250 turns of 14 gauge Cu wire coated with polyamideimde (NEMA MW 35-C, class 200).

The electromagnet assembly is suspended from the top of the chamber and is fixed as an integrated part of the sputtering system.

The center point O of the electromagnet coincides with the sample stage, to form a uniform in-plane magnetic field across the sample surface. The two sets of coil pairs are connected to two identical Kepco bipolar operational power supplies (BOP 20-20M), respectively, via a 2 3/4" CF electrical feedthrough, as shown in Fig. 2.17(a). See items FE, PS1, PS2. The power supplies are controlled under voltage programming input mode, the input signals coming from the two analog output channels AO0 and AO1 of the DAQ NI6212, for coil pairs 1 and 2 respectively. Fig. 2.17 (c) shows the distribution of magnetic fluxes in the electromagnet core. Magnetic flux a is generated by the coils in *Pair 1*, while flux b is generated by *Pair 2*. The flux flowing through poles *p2, p4* is thus $a+b$, and that through *p1, p3* is $a-b$. At the center point O, the magnetic field is therefore determined by the vector sum of $a+b$ and $a-b$, as illustrated in Fig. 2.18(a). If the currents in the coils alternate at a quasi-static (<1 Hz) rate, we can assume that the fluxes follow the instantaneous currents. By applying currents in the form of $\sin(\omega t+\phi)\times\cos(\omega t+\phi)$, where ω is the angular speed and ϕ the initial phase, and separating the currents in the two pairs of coils by a phase difference of $\pi/4$, we achieve a vector sum of constant norm rotating at the given angular speed, as shown in Fig. 2.18(b).

In terms of instrumentation, we define 80 evenly spaced sampling points on each of the two ac curves in Fig. 2.18 (b). These two sets of values are then written to the analog output channels of NI6212, AO0 and AO1, at the clock rate which is determined by the motor rotation speed. Since there are 80 sampling points for one period of the magnetic field rotation and 80 digital pulses for one rotation of the motor, the field rotates synchronously with the sample. To change the angle between the sample reference axis and the magnetic field, it is sufficient to change the initial phase ϕ of the ac current curve $\sin(\omega t+\phi)\times\cos(\omega t+\phi)$. This can be programmed in a straightforward manner.

To verify that the magnetic field does rotate as programmed, we set the sample rotation speed to 0.25 RPM and measured the field strength at point O in the x-direction

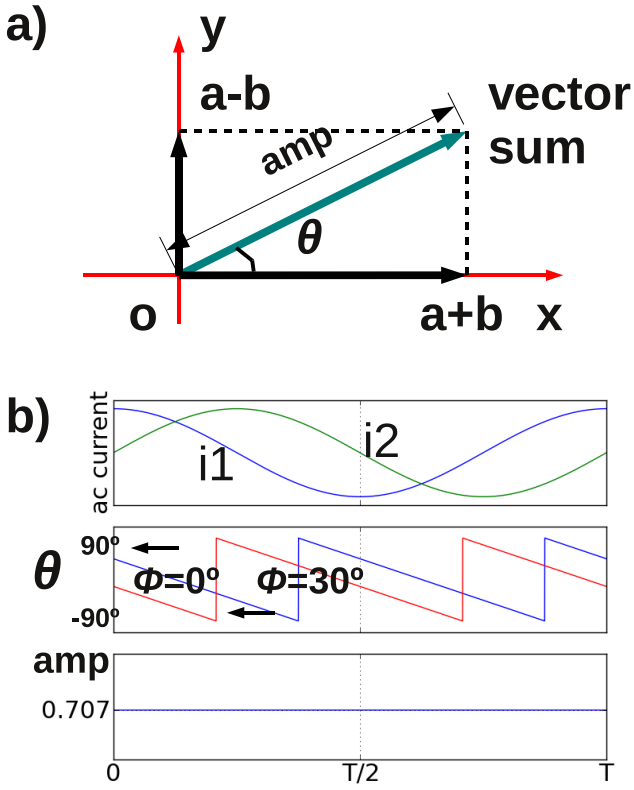

Figure 2.18: (a) Schematic: vector sum of the two orthogonal fluxes at the center point of the electromagnet; (b) the correspondence between the sputtering field and the applied ac currents; as shown in the middle panel, different choice in the initial phase ϕ would make the field start rotating at a different angle θ.

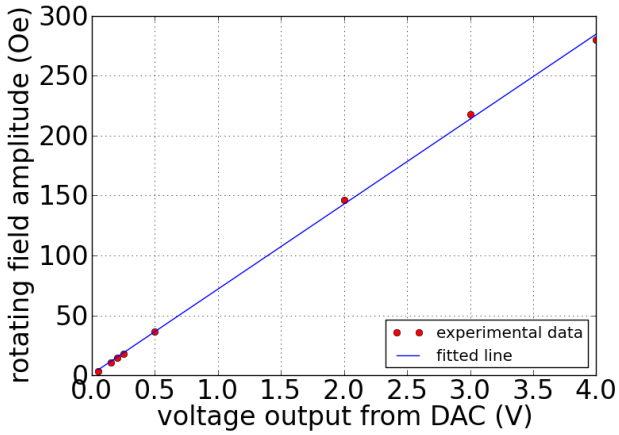

Figure 2.19: Linear relationship between the applied voltage control and measured magnitude of the rotating magnetic field.

using a LakeShore 421 Gauss probe, varying the voltage input amplitude to AO channels of NI6212. The measured field strength showed clear sinusoidal variation with a period of 4 seconds. The amplitude of the measured sinusoidal curves are shown in Fig. 2.19, which has a linear dependence on the amplitude of the ac voltage output of the power supplies.

2.4.3 Demonstration

To demonstrate the arbitrary vector control of the magnetic anisotropy in thin film samples using this *in-situ* electromagnet, we deposited two sets of Ta (3 nm)/$Co_{91.5}Zr_{4.0}Ta_{4.5}$ (200 nm)/SiO_2 (10 nm) films on 1 cm×1 cm Si/thermal SiO_2 substrates using the field sputtering setup described in the previous section, with the external field strength of 50 Oe, to study their soft magnetic properties. The 3 nm Ta layer is the seed layer to improve adhesion and homogeneity of the film. The top SiO_2 layer protects the metallic film from oxidation. The ferromagnetic layer $Co_{91.5}Zr_{4.0}Ta_{4.5}$ (200nm) was DC magnetron sputtered at optimized conditions, with power 400 W, Ar pressure 1.2 mTorr, and deposition rate 4.3 Å/sec. The alignment of the sample with the sputtering field is demonstrated in Fig. 2.20

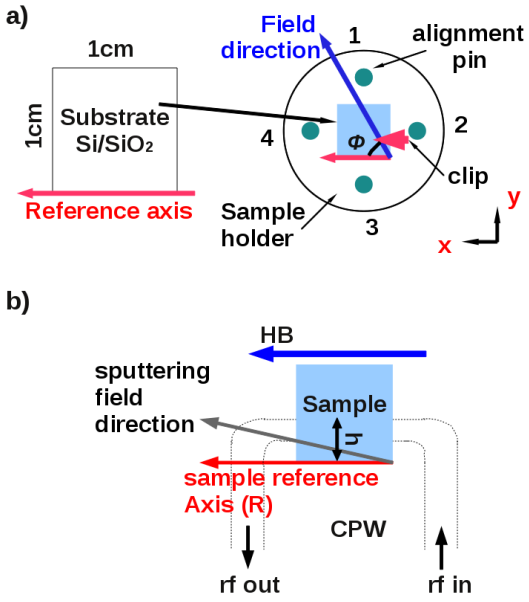

Figure 2.20: (a) Alignment of the sample and the sputtering field; the field direction is determined by the initial phase ϕ; the default setting of $\phi = 0$ results in a sputtering field parallel to the sample reference axis; (b) FMR setup configuration: the film side of the sample faces the coplanar waveguide (CPW); the sputtering field direction is also the easy-axis of the sample with uniaxial induced anisotropy.

(a). One of the substrate edges is chosen to be the reference axis for the sample. When mounted on the sample holder, the reference axis is aligned with the alignment pins 2 and 4 in the x-direction, which is the default direction of the magnetic field when the initial phase is set to zero. The initial phase ϕ can be set to an arbitrary value to change the relative angle between the sputtering field direction and the sample reference axis.

To first confirm that the sample rotation during field sputtering improves the uniformity of the film and hence the soft magnetic properties, two films, A and B, were deposited in sample set 1; sample A was stationarily field-sputtered (without sample rotation), and B was deposited under the magnetic field rotating synchronously with the sample. The hysteresis loops of the two samples were measured using a BH loop tracer, and are shown in Fig.2.21 (a) and (b), respectively. While both of the samples have an anisotropy field H_K

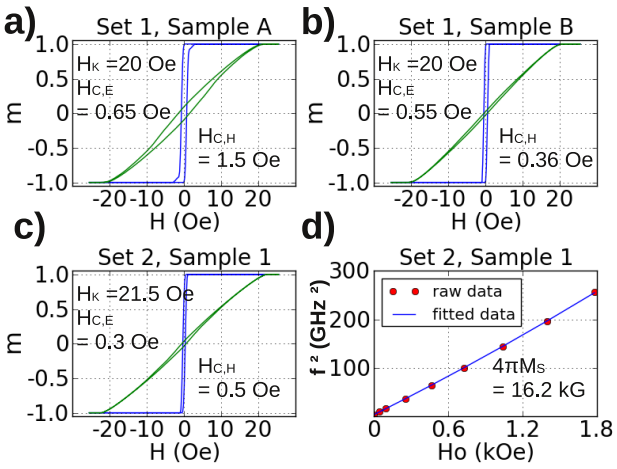

Figure 2.21: (a) *B-H* loop of sample 1 in set 1; (b) *B-H* loop of sample 2 in set 1; (c) *B-H* loop of sample 1 in set 2; (d) FMR Kittel relation of sample 1 in set 2.

= 20 Oe and comparably low easy-axis coercivities, sample B shows a more linear response along the hard-axis ($H_{C,H}$ = 0.36 Oe compared with 1.5 Oe for A).

To verify that the induced anisotropy in the sputtered films follows the applied rotating magnetic field as expected, we deposited a second sample set consisting of 9 films, all field-sputtered under rotating magnetic field, with the initial phase of the field set to be $\phi = 0°$, 18°, 36°, 45°, 63°, 90°, 108°, 135° and 153° respectively. The magnetic properties of the as-deposited films were studied by B-H loop tracer and parallel-condition ferromagnetic resonance (FMR) spectra. Fig. 2.20 (b) illustrates the FMR measurement configuration. As a reference, the *B-H* loop and Kittel relation of the FMR field and frequency for sample 1 ($\phi = 0°$) are shown in Fig. 2.21 (c) and (d) respectively. The easy-axis of the film was measured by the B-H loop tracer to be parallel with the sample reference axis, along which the sputtering field was applied. The anisotropy field H_K is 21.5 Oe. The film shows very low coercivity along both the easy- and the hard-axes, with $H_{C,E}$ = 0.3 Oe and $H_{C,H}$ = 0.5 Oe. Note that the second set of samples were deposited at a different point in the lifetime of the $Co_{91.5}Zr_{4.0}Ta_{4.5}$ sputtering target, and a slight change in the sputtered film composition or target current is possible compared with the first set of samples. This fact is likely to

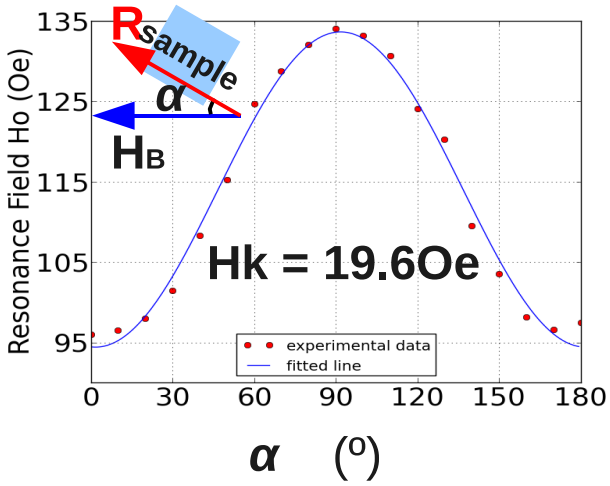

Figure 2.22: Change of ferromagnetic resonance field H_0 at 4GHz, as the angle α between the FMR bias field H_B and the sample reference axis R varies from 0° to 180°.

lead to a change in the uniaxial anisotropy energy of the material. The FMR measurement gives the saturation magnetization of 16.2 kG, using the Kittel relation

$$(\frac{\omega}{2\pi})^2 = \gamma^2 \times (H_B + H_K) \times (H_B + H_K + 4\pi M_S)$$

where ω is the rf circular frequency, $\gamma = \frac{e}{2mc} = 2\pi \times 2.799 \times \frac{g_{eff}}{2} \times \frac{MHz}{Oe}$ assuming $g_{eff} = 2.2$, and H_B is the in-plane bias magnetic field. A rotational FMR measurement at 4 GHz was also performed to investigate the uniaxial anisotropy of sample 1 in set 2. As shown in Fig. 2.22, the resonance field values (H_0) were recorded as the angle α between the sample reference axis R and the direction of the bias field H_B varied at a step of 10 degrees. Note that the angle has estimated error of ± 1.5°. The sinusoidal fit yields $H_K = 19.6$ Oe, which is in reasonable agreement with the value of 21.5 Oe given by the BH looper. Fig. 2.23 shows the FMR field values at 4 GHz for samples 2-9, when the sample reference axis is parallel with the FMR bias field direction. Assuming the alignment during substrate mounting is perfect, the data points should sit on the identical curve as in Fig. 2.22. The sinusoidal fit gives $H_k = 21.4$ Oe, in agreement with the value of 21.5 Oe given by the BH looper, and comparable with 19.6 Oe given in Fig. 2.22. There is a phase offset of 8.8°, which is

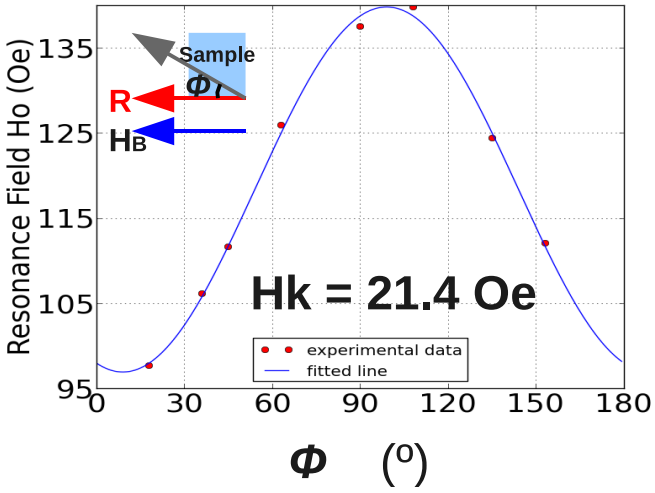

Figure 2.23: Change of ferromagnetic resonance field H_0 at 4 GHz, as the initial phase of the rotating magnetic field ϕ varies from 0° to 180°; each data point corresponds to one sample; FMR setup configuration for samples 2-9: the induced anisotropy of the film is determined by the sputtering field direction; the sample reference axis is always parallel with the FMR bias field.

introduced by the error in alignment when loading the samples into the sputtering chamber.

2.4.4 Summary of the field-sputtering using *in-situ* electromagnet

We have demonstrated the technique to generate magnetic anisotropy at arbitrary angle in the plane of a sputtered layer, compatible with uniform deposition in UHV. Our experimental data on the $Co_{91.5}Zr_{4.0}Ta_{4.5}$ films show well-defined induced uniaxial anisotropies, controlled *in-situ*, with very soft magnetic properties enabled through deposition uniformity from the rotating substrate. Further extension of the technique would include orthogonal anisotropy generation for the pinned and free layers of a magnetic tunnel junction sensor, allowing for linear response along the free layer hard-axis.

2.5 Summary

We have understood in this chapter the physical origins of the most essential static magnetic properties in FM thin films, the uniaxial anisotropy field H_k, the permeability μ and the coercivity H_c, which are critical parameters for evaluating a material as the candidate for specific applications. We reviewed the trajectories of the atoms in the sputtering process, related the film quality to the kinetics of the adatoms and therefore the sputtering parameters, and connected the control of sputtering process to the optimization of the magnetic properties. We demonstrated the incorporation of the specially designed *in-situ* electromagnet in the UHV sputtering chamber and its successful implementation in materials optimization. With this knowledge of the building blocks of our heterostructures, the FM thin film single layers, we now proceed to the next step of making device-related structures out of them.

Chapter 3

Laminated $Co_{91.5}Zr_{4.0}Ta_{4.5}$ and $Ni_{80}Fe_{20}$ thin films: implementation in magnetic-core integrated inductors

With the rapid development of consumer electronics market, higher efficiency of power management systems for microprocessor and system-on-chip (SoC) applications has become a pressing need. Integrated voltage regulators (IVRs) offer the potential of scalable power supplies that improve dynamic voltage and frequency scaling for digital integrated circuits [27]. Exploiting package-level air-core inductors, buck-converter IVRs have displayed the most promise with high current densities and efficiencies with a continuous range of conversion ratios [27–30]. The use of magnetic-core inductors in these applications promises higher efficiencies and support of higher converter densities.

3.1 Introduction: magnetic-core integrated inductors

In this chapter, We show the optimization of magnetic properties of ferromagnetic (FM)/SiO_2 /FM trilayer structures as potential candidates for the magnetic core in toroidal integrated inductors, with FM materials $Co_{91.5}Zr_{4.0}Ta_{4.5}$ (CZT) and $Ni_{80}Fe_{20}$ (Py). In the single-layer parent films we found a monotonic reduction of easy-axis coercivity (H_c down to 0.17 Oe in CZT, 0.4 Oe in Py) with increasing dc magnetron sputtering voltage. In the trilayer rectangular structures, with induced easy-axis in the short lateral dimension, we found proof of dipolar coupling between the two FM layers from BH loop measurements in the CZT system, showing linear response with minimal hysteresis loss when the external field is applied in the long axis. Py elements did not show this optimized property. Further investigation of domain configurations using scanning transmission x-ray microscopy (STXM) suggests an insufficient induced anisotropy in Py compared with the shape anisotropy to realize the antiparallel-coupled state.

Integrated ferromagnetic (FM)-core inductors have been limited in the enhancement of inductance density over air-core structures, of a factor ∼30 at best [31], due to magnetostatic edge effects. Toroidal, flux-closed structures avoid this problem and can increase the effective permeability to as high as μ_r of the core [11]. The challenge lies in two aspects. One is engineering an isotropic core, keeping high permeability with low hysteresis loss throughout the closed path, while FM films typically have uniaxial anisotropy [32]. Another is aligning the magnetization transverse to the flux path for high permeability, overcoming the demagnetizing effect from the path shape. $Ni_{80}Fe_{20}$ (Py) ($4\pi M_s$ = 10.75 kG, ρ = 20 Ω·cm) and $Co_{91.5}Zr_{4.0}Ta_{4.5}$ (CZT) ($4\pi M_s$ = 17 kG, ρ = 100 Ω·cm) are well-investigated soft magnetic materials with much application in magnetoelectronics [33]. We choose them as candidates for the toroidal core material and address the above-mentioned two issues accordingly.

First, to achieve isotropy in magnetic films, we use the concept of isotropic high permeability multilayers, proposed by Frommberger *et al.* [25]. In an improvement over this prior work, we have incorporated the quadrupole electromagnet into the UHV magnetron

sputtering chamber, which enables an *in situ* magnetic field rotating synchronously with the substrate at arbitrary phase difference [12]. Successive laminations of FM material with anisotropy axes rotating at designated step could be obtained in one deposition, without breaking vacuum. In addition, very low Ar pressure during dc sputtering is used in our system, allowing for a mean free path comparable with the target-substrate separation. We show the control of soft magnetic properties of single-layer extended films by varying the sputtering voltage and thus the kinetic energy of the incident particles, optimizing the building blocks for isotropic multi-layered films.

Second, to arrange the high-permeability axis along the flux path, we fabricate elongated structures (rectangles and stripes) and induce the easy axis transverse to the long lateral dimension. By using FM/nonmagnetic (NM)/FM trilayers, we expect to produce the easy-axis state in the element originating from the dipolar coupling between the two FM layers [34]. The elimination of domain walls (DWs) (inevitable in the closure-domain states in single-layer patterned elements) leads to nearly-pure rotational hard-axis response when an external field is applied along the elongated direction. We found CZT more suitable for this application with its relatively high induced anisotropy overcoming the shape anisotropy. Negligible hysteresis loss could be achieved in these elements. However we did not find proof of the easy-axis state in the Py trilayer elements, conflicting with the calculated phase diagrams in Ref. [34].

3.2 Experiment

3.2.1 Core loss in inductors

The power dissipation in metallic inductor cores comes from two sources of loss: eddy currents and hysteresis [33]. Laminating the magnetic alloy film with a dielectric, NM material (SiO_2) is thought to inhibit the eddy currents and reduces the coercivity significantly [35,36]. In optimizing the multilayered structure, the first step is to determine the optimal single FM layer thickness t_{FM} and its deposition conditions. To eliminate the eddy currents, t_{FM}

should be thinner than the skin depth δ of the FM material, $\delta_{Py} = 159$ nm, $\delta_{CZT} = 622$ nm at 500 MHz, calculated from parameters given in Ref. [33]. In terms of the hysteresis, we attribute the easy-axis (EA) coercivity H_c^{EA} dominantly to the interaction of 180° DWs with surface irregularities, since Py (polycrystalline) and CZT (amorphous) both have zero magnetostriction [37]. The coercive field can be estimated proportional to $\Delta t_{FM}/t_{FM}$, where Δt_{FM} is the fluctuation in film thickness. Hard-axis (HA) coercivity comes from the small local fluctuation of induced anisotropy which leads to ripple domains [3]. The magnetization orienting in the HA in the DWs contributes to the remanent magnetization in the HA loop. H_c^{HA} is thus not associated with DW motion. However, longer wavelength of anisotropy dispersion or better film homogeneity will reduce the DW density in the HA remanent state, leading to a reduction in H_c^{HA}.

3.2.2 Single-layer FM film optimization

Fig. 3.1 shows the thickness dependence of the EA and HA coercivities in extended single-layer films. The uniaxial anisotropy ($H_k^{Py} = 3.5$ Oe, $H_k^{CZT} = 20$ Oe measured with B-H loop tracer) is induced during deposition, by a field of ∼75 Oe imposed by the quadrupole electromagnet. The dc sputtering voltage and Ar pressure for Py and CZT were 480 V, 1.3 mTorr and 420V, 1.2 mTorr, respectively (we see voltage as a critical parameter determining the film surface quality, explained in the next section). While thicker amorphous CZT films, up to 500 nm, might have given much lower coercivity (0.015 Oe) [38], we found crystallization in our 400 nm film, confirmed by XRD, leading to an abrupt increase in H_c. Elevated substrate temperature during long deposition may contribute to this result since the sample stage is not water-cooled in our system. 100 nm Py film is in the vicinity of transition from cross-tie walls to asymmetric Bloch walls [39], showing an increase in H_c^{EA} while H_c^{HA} remained at the same level. If we plot the EA coercivity as a function of $1/t_{FM}$ in the region where no DW-type transition or crystallization occurs, the data show linearity, which is expected from $H_c^{EA} \propto \Delta t_{FM}/t_{FM}$. The offset might reflect the instrinsic H_c not

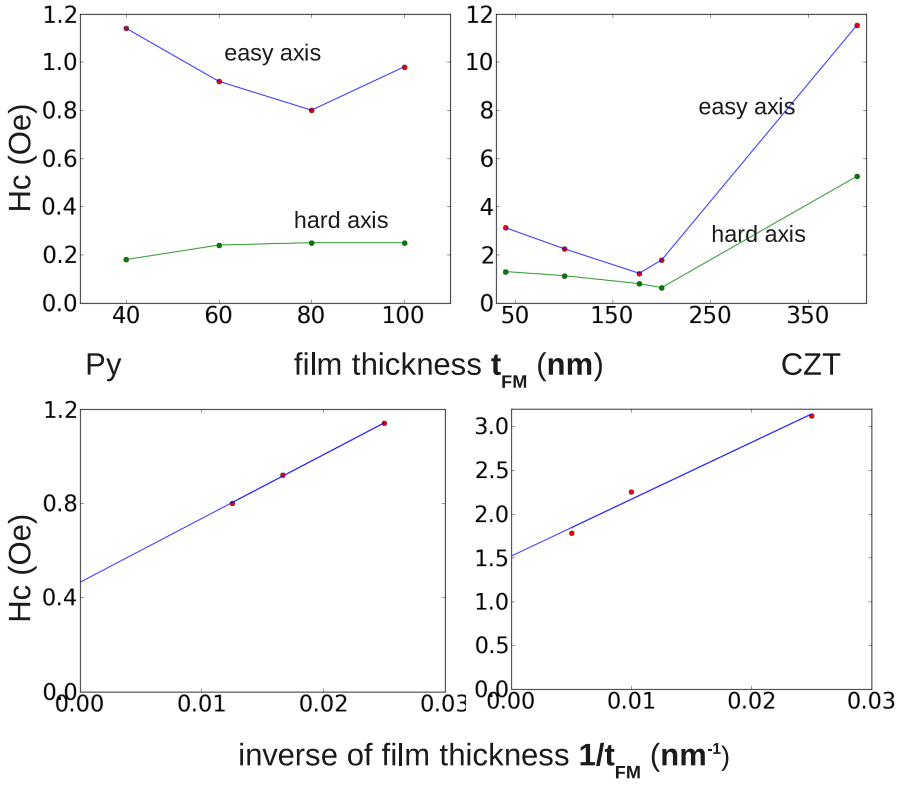

Figure 3.1: Thickness (t_{FM}) dependence of coercivity (H_c) in uniaxial anisotropy extended single-layer films, Py(left) and CZT(right). Lower panel demonstrates the linear dependence of H_c^{EA} on the inverse of t_{FM}, $1/t_{FM}$, while Δt_{FM} remains at the same level at a specific sputtering voltage.

associated with the surface property.

Next, we chose the film thicknesses with the lowest coercivity, *i.e.* 80 nm for Py and 200 nm for CZT, for further optimization in the deposition conditions. We keep the lowest possible Ar pressure (∼1.2 mTorr) during sputtering for all depositions, with an estimated mean free path of 4 cm which is comparable with the target-substrate separation of 10 cm. Sufficient presputtering ensures the target composition in the deposited films [40]. The average sputtered atom energy is dependent on the dc sputtering voltage, given by

$$E = U_s \ln(\gamma \frac{E_{ion}}{U_s}) - U_s,$$

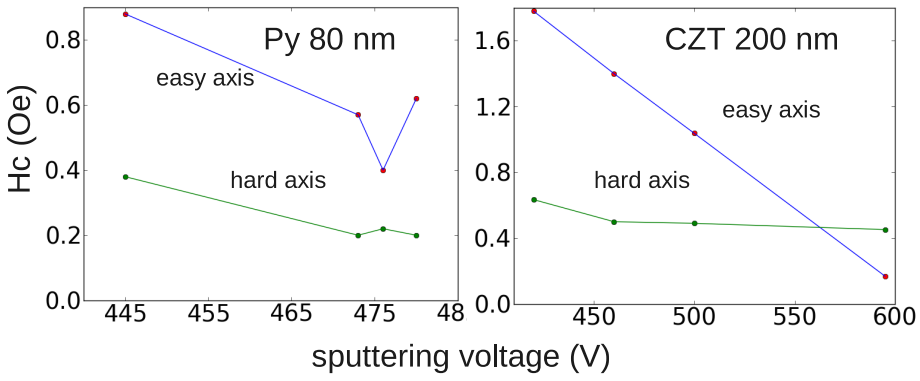

Figure 3.2: Sputtering voltage dependence of coercivity (H_c) in uniaxial anisotropy extended single-layer films with the optimized thickness, Py 80 nm (left) and CZT 200 nm (right).

where U_s is the surface energy barrier for the atoms to escape from the target, $\gamma = (4M_1M_2)/(M_1 + M_2)^2$ with M_1 and M_1 being the incident and sputtered particle weight respectively, and E_{ion} is the incident Ar ion energy (proportional to the sputtering voltage). This equation gives sputtered Co atom energy at 4.85 eV and 6.3 eV under sputtering voltage of 400 V and 600 V, respectively. Similar conclusion could be drawn about the fast neutrals, which are back-reflected Ar ions combined with electrons. These energetic particles, especially the high-energy fast neutrals, bombard the sample surface and improve the diffusivity of the adatoms, leading to enhanced film homogeneity and lower surface roughness [8]. Fig. 3.2 demonstrates the reduction of coercivity with increasing sputtering voltage, noticeably with CZT showing a monotonic trend.

3.2.3 Bilayer patterned FM films: magnetic flux closure between the layers and rotational response

After determining the individual FM layer thickness and the deposition conditions, we examine the shape anisotropy and the interaction between the FM layers in elongated, multilayer structures. For applications in integrated inductors, lateral dimensions of several

hundred microns are of the most interest [33]. One of our potential implementations of the magnetic core structures is described in Ref. [14]. To immitate the device operation conditions in a physically tangible manner for materials engineering, we make films with the lowest number of laminations, namely an FM/SiO_2(t_{SiO_2} nm)/FM sandwich trilayer with the optimized individual FM layer thickness. We selected the dielectric layer thickness t_{SiO_2} to be 4, 6, 10, 20 and 40, to explore the coupling effects between the FM layers. We then pattern the parent films, using photolithography and liftoff process, into stripes (1 cm$\times$ 150 μm) and rectangles (400 μm $\times$ 100 μm), with the induced EA parallel to the short axis of the patterned elements. The classic work of Slonczewski [34] examined the domain configurations in infinitely long FM/NM/FM stripes thoroughly, and demonstrated the flux-closure between the two FM layers, leading to single-domain easy-axis state in the individual FM layer. We find our elongated sandwich structures within the dimension range of this desirable configuration, and hope to realize a linear hard-axis response along the long axis in quasi-static (16 Hz) *B-H* loop tracer measurements.

The antiparallel alignment of magnetization in the two FM layers along the short axis in elongated FM/NM/FM sandwich structures could be inferred from the specific shape of the BH loop measured along the short axis, with a plateau at low applied field, centered at zero [41]. This feature is observed in all the CZT samples we explored for various t_{SiO_2} (hysteresis loops not shown). We choose the lowest t_{SiO_2} value 4 nm, to minimize the loss of effective permeability in the final multilayer magnetic core, as the dielectric layers do not contribute to the saturation magnetization. We demonstrate in Fig. 3.3 the hysteresis loops for CZT(200 nm)/SiO_2(4 nm)/CZT(200 nm) stripes and rectangles. We estimated a permeability of $\sim$1380 for these structures, from the saturation magnetization of 17.15 kG measured by FMR and H_k of 12 Oe from both the FMR and BH loop measurements. This result is comparable with the highest value we found in the literature for CoZrTa patterned films [42], while our films exhibit lower H_c. Note, however, that the plateau is much more accentuated in the long stripes (Fig. 3.3(a)) than in the rectangles (Fig. 3.3 (b)). A possible explanation for the weakening of this antiparallel flux-closure between the FM

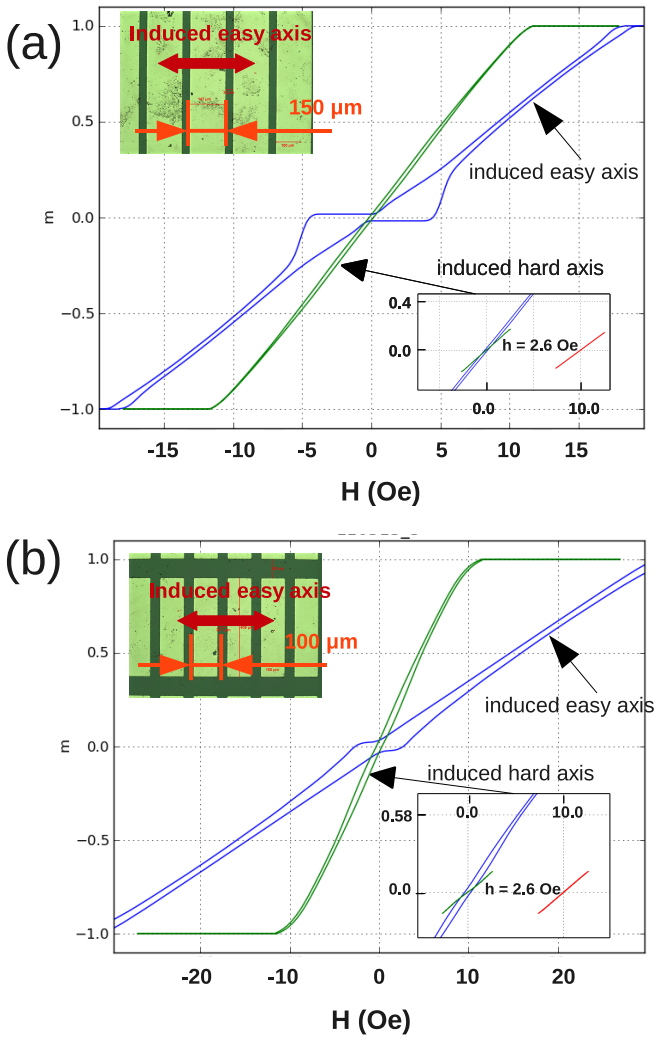

Figure 3.3: *M-H* loops for $Co_{91.5}Zr_{4.0}Ta_{4.5}$(200 nm)/$SiO_2$(4 nm)/$Co_{91.5}Zr_{4.0}Ta_{4.5}$(200 nm) structures. The inset at the lower right minor loops on induced hard axis showing linear response with negligible hysteresis loss, at 0 and 10 Oe bias fields. The permeability is slightly reduced in minor loops. (a) 1 cm× 150 μm (b) 400 μm × 100 μm

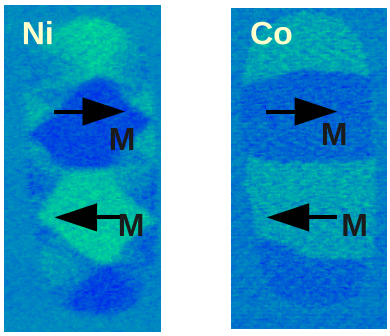

Figure 3.4: Domain imaging using STXM, with the x-ray photon energy set to Ni L_3 edge for the top Py layer (left panel, showing diamond structure) and Co L_3 edge for the bottom CoFeB layer (right panel, magnetization along the induced easy axis); the dark and bright contrast refer to magnetization pointing to the right and left respectively.

layers is the extra demagnetizing effect introduced by the sharp corners of the rectangular shape, preventing the local formation of edge curling wall [34]. In the theoretical models of Slonczewski, the FM/NM/FM stripes are infinitely long, and the effects at the ends are eliminated. In our case, the stripes 1 cm$\times$ 150 μm are better suited to the theoretical model.

Further more, we did not observe any plateau in the Py(80 nm)/SiO_2(t_{SiO_2} nm)/Py(80 nm) systems (loops not shown). An estimation of the shape anisotropy in the Py elements, $H_{shape} = M_s(2t/\pi)(1/w - 1/l)$ where t is the thickness, w is the width and l is the length of the FM slab, respectively, gives 4.5 Oe, which is at least equivalent to, if not dominating over the induced anisotropy $H_k = 3.5$ Oe. A further investigation on the domain configuration in a rectangular (30 μm $\times$7.5 μm) heterostructure $Ni_{80}Fe_{20}$(23 nm)/Ta(4 nm)/$Co_{40}Fe_{40}B_{20}$(15 nm) was carried out using STXM at the Canadian Light Source (CLS) SM beamline. Fig. 3.4 demonstrates the alignment of domains in the induced easy axis in the CoFeB element (having similar $4\pi M_s$ and H_k to CZT), while the Py element forms classic diamond structures.

3.3 Conclusion and outlook

We have shown in this chapter, together with our previous work [12] on the *in-situ* electromagnet described in Chap.2.4, the control of well-defined high-permeability axis in micron-patterned, multilayered structures. We demonstrated in the CZT system the ability to align the magnetization transverse to the long axis in finite elongated structures, with optimized 3d dimensions for the interest of integrated inductors, leading to extremely low hysteresis loss and high-permeability along the net magnetic flux path. These structures make up the segments in a toroidal magnetic core. With rotating induced anisotropy in adjacent sandwich trilayers in a multilayered film (with tens of laminations), isotropic high-permeability flux-closed core could be achieved. Since these multilayered structures are intended for inductors operating in the GHz range, we are now prepared for the exploration of high-frequency magnetization dynamics, governed by the Landau-Lifshitz-Gilbert (LLG) equation which we will discuss in the next chapter.

Chapter 4

The Landau-Lifshitz-Gilbert equation: equation of motion for magnetization dynamics

The equation of motion for magnetization dynamics is the Landau-Lifshitz-Gilbert (LLG) equation, which has the form

$$\dot{\mathbf{m}} = -\gamma \mathbf{m} \times \mathbf{H}_{eff} + \alpha \mathbf{m} \times \dot{\mathbf{m}} \tag{4.1}$$

where $\mathbf{m} = \mathbf{M}/M_s$ is the normalized magnetization, γ is the gyromagnetic ratio defined as the ratio of the magnetic dipole moment to the angular momentum, $\gamma = (g_{eff}/2)2\pi \times$ 2.799 MHz/Oe where g_{eff} is the effective g-factor, $\mathbf{H}_{eff}$ is the effective magnetic field with contributions from the DC bias field, anisotropy field, demagnetizing field, exchange interaction, *etc.*, and α is the dimensionless, phenomenological Gilbert damping parameter, typically in the range of 0.002 - 0.10 in ferromagnetic (FM) metals. The first term is the driving torque and represents the Larmor precession, which causes the magnetization $\mathbf{M}$ to precess about the effective field $\mathbf{H}_{eff}$; the second term is the phenomenological damping term following the Gilbert form, which exerts a torque perpendicular to the precessional motion of $\mathbf{M}$, reducing the precession cone angle between $\mathbf{M}$ and $\mathbf{H}_{eff}$ if an external driving rf field is not applied continuously. In this chapter, we will look into solutions of the LLG

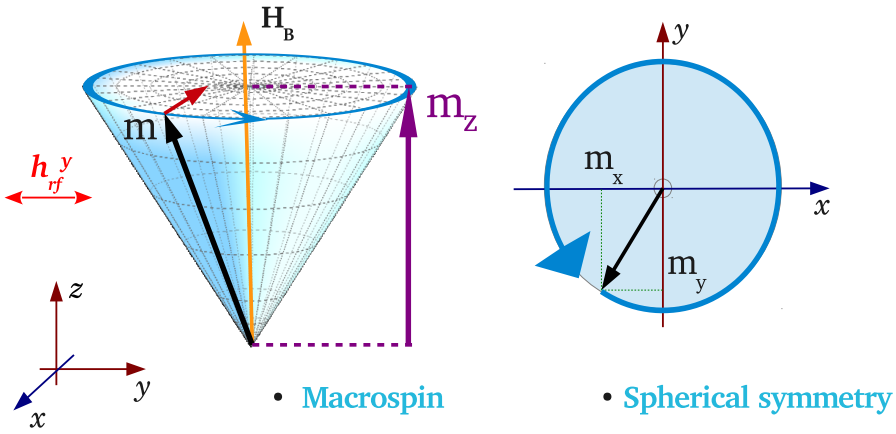

Figure 4.1: *Left* panel: cartoon illustrating the precession of **M** around the DC bias field H_B; the blue arrow indicates the motion of **M** and the red arrow at the tip of **m** represents the damping torque which cause the cone angle to decrease. *Right* panel shows the circular pression of the **M**, with the trajectory of the tip of **m** forming a circle and $\mathbf{m}_z$ remains constant.

equation in the small-angle limit, under the two most typical circumstances, 1) circular and 2) elliptical precession, which could be applied in the out-of-plane ferromagnetic resonance (FMR) and the in-plane FMR, respectively, and discuss the power absorption in the FMR spectra. We will leave the discussion of the physical origin of the phenomenological Gilbert damping parameter in itinerant ferromagnets to Chap. 5, where we will introduce the theoretical model of electron scattering mechanism as well as our experimental results which apply the model to ultrathin films and verify certain aspects for the first time.

4.1 Circular precession

If we have an isotropic, bulk material, the LLG equation can be solved in the simplest case, yielding the circular precession of the magnetization **M**. Fig. 4.1 illustrates the geometry of this most basic circular pressesional case. Here, we have four basic assumptions for treating the problem:

1. The *macrospin* model: perfectly uniform magnetization in the material; exchange interaction as $H_{ex} = \frac{A}{M}\nabla^2\mathbf{M}$, where A is the exchange stiffness constant, does not contribute to the effective field $\mathbf{H}_{eff}$.

2. Isotropic bulk material: zero magnetocrystalline anisotropy and zero demagnetizing field from the geometry of the system, therefore we need concern only the DC bias field in the z-axis $H_z^{eff} = H_B$.

3. Small excitation rf field h_y^{rf} along the y-axis, in the form of $H_y^{eff} = H_y e^{-i\omega t}$

4. Small angle precession where m_z could be approximated by 1, and m_x, $m_y \ll 1$.

First we calculate the driving torque, starting from evaluating the term $\mathbf{m} \times \mathbf{H}_{eff}$, where

$$\mathbf{m} = m_x\hat{\mathbf{i}} + m_y\hat{\mathbf{j}} + m_z\hat{\mathbf{k}},$$

$$\mathbf{H}_{eff} = H_x^{eff}\hat{\mathbf{i}} + H_y^{eff}\hat{\mathbf{j}} + H_z^{eff}\hat{\mathbf{k}}.$$

$\mathbf{m} \times \mathbf{H}_{eff}$ is calculated as

$$\begin{vmatrix} \hat{\mathbf{i}} & \hat{\mathbf{j}} & \hat{\mathbf{k}} \\ m_x & m_y & m_z \\ H_x^{eff} & H_y^{eff} & H_y^{eff} \end{vmatrix} = \begin{vmatrix} \hat{\mathbf{i}} & \hat{\mathbf{j}} & \hat{\mathbf{k}} \\ m_x & m_y & 1 \\ 0 & H_y e^{-i\omega t} & H_B \end{vmatrix}$$

which yields

$$-\gamma\mathbf{m} \times \mathbf{H}_{eff} = -\gamma \begin{pmatrix} m_y H_B - H_y e^{-i\omega t}, & -m_x H_B, & 0 \end{pmatrix} \begin{pmatrix} \hat{\mathbf{i}} \\ \hat{\mathbf{j}} \\ \hat{\mathbf{k}} \end{pmatrix} \tag{4.2}$$

neglecting the second order term $m_x H_y e^{-i\omega t}$. Next, we calculate the term $\mathbf{m} \times \dot{\mathbf{m}}$ as

$$\begin{vmatrix} \hat{\mathbf{i}} & \hat{\mathbf{j}} & \hat{\mathbf{k}} \\ m_x & m_y & 1 \\ -\gamma(m_y H_B - H_y e^{-i\omega t}), & -\gamma(-m_x H_B), & 0 \end{vmatrix}$$

which yields

$$\alpha \mathbf{m} \times \dot{\mathbf{m}} \;=\; -\alpha\gamma \begin{pmatrix} m_x H_B, & m_y H_B - H_y e^{-i\omega t}, & 0 \end{pmatrix} \begin{pmatrix} \hat{\mathbf{i}} \\ \\ \hat{\mathbf{j}} \\ \\ \hat{\mathbf{k}} \end{pmatrix} \tag{4.3}$$

neglecting the second order terms.

Inserting Eq. 4.2 and Eq. 4.3 into Eq. 4.1 we have the linearized form of Eq. 4.1 in the small angle limit:

$$\begin{pmatrix} \dot{m_x} \\ \\ \dot{m_y} \end{pmatrix} \;=\; \gamma H_B \begin{pmatrix} -\alpha & -1 \\ \\ 1 & -\alpha \end{pmatrix} \begin{pmatrix} m_x \\ \\ m_y \end{pmatrix} \;+\; \gamma \begin{pmatrix} H_y e^{-i\omega t} \\ \\ 0 \end{pmatrix} \tag{4.4}$$

neglecting the second order terms. Using the second row of Eq. 4.4, we have

$$m_x = \alpha m_y + \frac{1}{\gamma H_B} \dot{m_y}. \tag{4.5}$$

Inserting this expression of m_x into the first row of Eq. 4.4, we arrive at the equation of motion for m_y,

$$\ddot{m_y} + 2\alpha(\gamma H_B)\dot{m_y} + (\gamma H_B)^2 m_y = (\gamma H_B)(\gamma H_y) e^{-i\omega t} \tag{4.6}$$

which takes the form of the classical equation of motion for a driven damped harmonic oscillator,

$$\ddot{x} + 2\eta\omega_0 \dot{x} + \omega_0^2 x = f_0 e^{-i\omega t} \tag{4.7}$$

where η is the damping factor, ω_0 is the resonance frequency of the harmonic oscillator and the term $f_0 e^{-i\omega t}$ is the sinusoidal driving force. Comparing Eq. 4.6 to this forced damped harmonic oscillator case, we can easily see that the resonance frequency of the **M** precession is

$$\omega_0 = \gamma H_B,$$

determined by the bias field H_B and the gyromagnetic ratio, $\gamma = (g_{eff}/2)2\pi \times 2.799$ MHz/Oe, of the FM material. Assuming the form of solution to Eq. 4.6 as

$$m_y = \tilde{A} e^{-i\omega t} \tag{4.8}$$

where $\tilde{A}$ is the complex amplitude of m_y and inserting this expression into Eq. 4.5, we have

$$m_x = (\alpha - i\frac{\omega}{\gamma H_B})\tilde{A}e^{-i\omega t}$$

which states that for $\alpha \ll 1$, which is the typical case, on resonance at $\omega = \omega_0 = \gamma H_B$, m_x and m_y oscillate at the same amplitude with m_x lagging m_y by 90°, as illustrated in the right panel of Fig. 4.1. Again use the solution form Eq. 4.8 and insert it into Eq. 4.6, we can calculate the complex amplitude $\tilde{A}$ of oscillating m_y:

$$\tilde{A} = \frac{\gamma H_y}{[\omega_0 - (\frac{\omega}{\omega_0})\omega] - (2\alpha\omega)i} \tag{4.9}$$

where $\omega_0 = \gamma H_B$. On resonance at $\omega = \omega_0$, we have

$$\tilde{A} = \frac{\gamma H_y}{-(2\alpha\omega_0)i} = i\frac{\gamma}{2\alpha\omega_0}H_y \tag{4.10}$$

The parallel susceptibility $\chi_{\parallel}$ is defined as M_y/H_y and reflects the cone angle. We can see from Eq. 4.10 that on resonance,

$$\chi_{\parallel} = i\frac{1}{2\alpha H_0}.$$

where H_0 is the resonance field. This treatment of circular precession could be implemented for the out-of-plane ferromagnetic resonance (FMR) case with the effective field in the z-axis H_B replaced by $(H_B - 4\pi M_s)$, taking into account the demagnetizing field in a thin film.

4.2 Elliptical precession: in-plane FMR for a thin film

In this section we look into the in-plane ferromagnetic resonance (FMR) case for a thin film, which is widely encountered in applications due to the fact that the demagnetizing field forces the magnetization to lie in the sample plane in absence of a large (on the order of T, the saturation magnetization of typical itinerant FM materials) perpendicular bias field. The system geometry is illustrated in Fig. 4.2. We have used in-plane FMR in all experiments described in this thesis.

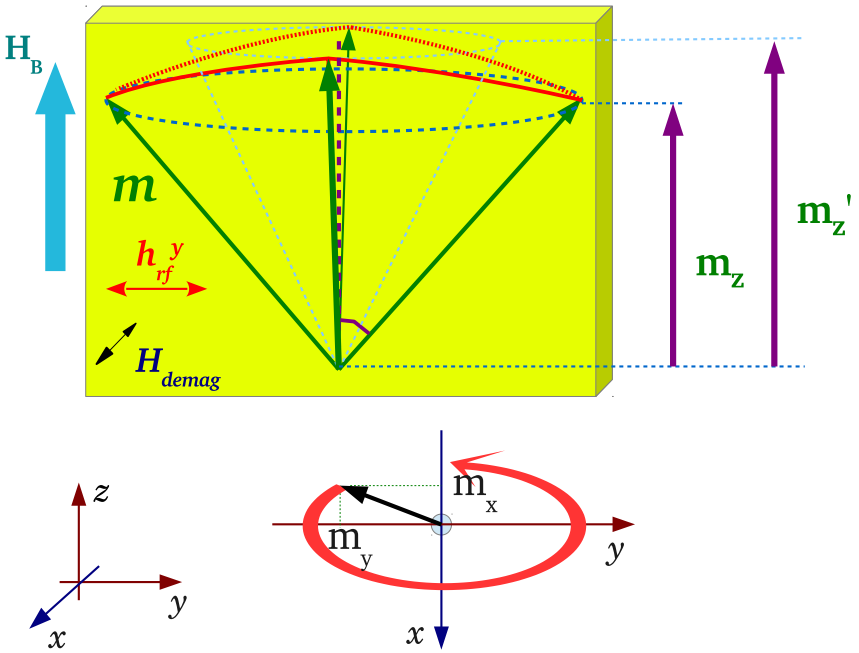

Figure 4.2: *Upper* panel: cartoon illustrating the precession of **M** around the DC bias field H_B with the in-plane driving rf field h_y^{rf} and out-of-plane demagnetizing field H_{demag} due to the oscillating out-of-plane **M** component m_x. The cone angles along the x-axis and the y-axis differ due to the demagnetizing effect. *Lower* panel shows the elliptical pression of the **M**.

Similar to the treatment of the circular case, still in the small-angle limit, we first calculate $\mathbf{m} \times \mathbf{H}_{eff}$:

$$\begin{vmatrix} \hat{\mathbf{i}} & \hat{\mathbf{j}} & \hat{\mathbf{k}} \\ m_x & m_y & m_z \\ H_x^{eff} & H_y^{eff} & H_y^{eff} \end{vmatrix} = \begin{vmatrix} \hat{\mathbf{i}} & \hat{\mathbf{j}} & \hat{\mathbf{k}} \\ m_x & m_y & 1 \\ -m_x(4\pi M_s) & H_y e^{-i\omega t} & H_B \end{vmatrix}$$

Note that the difference comes in the x-component of the effective field $\mathbf{H}_eff$, which is the demagnetizing field due to the oscillating m_x. This yields

$$-\gamma \mathbf{m} \times \mathbf{H}_{eff} = -\gamma \begin{pmatrix} m_y H_B - H_y e^{-i\omega t}, & (-4\pi M_s - H_B) m_x, & 0 \end{pmatrix} \begin{pmatrix} \hat{\mathbf{i}} \\ \hat{\mathbf{j}} \\ \hat{\mathbf{k}} \end{pmatrix} \tag{4.11}$$

Then we calculate the term $\mathbf{m} \times \dot{\mathbf{m}}$ as

$$\begin{vmatrix} \hat{\mathbf{i}} & \hat{\mathbf{j}} & \hat{\mathbf{k}} \\ m_x & m_y & 1 \\ -\gamma(m_y H_B - H_y e^{-i\omega t}), & -\gamma(-4\pi M_s - H_B) m_x, & 0 \end{vmatrix}$$

which yields

$$\alpha \mathbf{m} \times \dot{\mathbf{m}} = -\alpha\gamma \begin{pmatrix} m_x(4\pi M_s + H_B), & m_y H_B - H_y e^{-i\omega t}, & 0 \end{pmatrix} \begin{pmatrix} \hat{\mathbf{i}} \\ \hat{\mathbf{j}} \\ \hat{\mathbf{k}} \end{pmatrix} \tag{4.12}$$

neglecting the second order terms.

We can see from Eq. 4.11 and Eq. 4.12 that they are in complete analogy with Eq. 4.2 and Eq. 4.3 with the additional term of $-4\pi M_s$ in front of m_x representing the demagnetizing effect. Inserting Eq. 4.11 and Eq. 4.12 into Eq. 4.1 we have the linearized form of Eq. 4.1 in the small angle limit for in-plane FMR:

$$\begin{pmatrix} \dot{m}_x \\ \dot{m}_y \end{pmatrix} = \begin{pmatrix} -\alpha\gamma(4\pi M_s + H_B) & -\gamma H_B \\ \gamma(4\pi M_s + H_B) & -\alpha\gamma H_B \end{pmatrix} \begin{pmatrix} m_x \\ m_y \end{pmatrix} + \gamma \begin{pmatrix} H_y e^{-i\omega t} \\ 0 \end{pmatrix} \tag{4.13}$$

neglecting the second order terms. We have already learned from the circular precession that the resonance frequency is determined by the effective field and the gyromagnetic ratio as $\omega_0^{circ} = \gamma H_B$, therefore it makes the physical picture clearer if we define the following:

$$\omega_H \equiv \gamma H_B$$

$$\omega_M \equiv \gamma 4\pi M_s$$

for the elliptical case and make the expression of Eq. 4.13 more compact, as

$$\begin{pmatrix} \dot{m}_x \\ \\ \dot{m}_y \end{pmatrix} = \begin{pmatrix} -\alpha(\omega_M + \omega_H) & -\omega_H \\ \\ (\omega_M + \omega_H) & -\alpha\omega_H \end{pmatrix} \begin{pmatrix} m_x \\ \\ m_y \end{pmatrix} + \gamma \begin{pmatrix} H_y e^{-i\omega t} \\ \\ 0 \end{pmatrix} \tag{4.14}$$

Using the second row of Eq. 4.14, we have

$$m_x = \frac{\alpha\omega_H m_y + \dot{m}_y}{\omega_M + \omega_H}. \tag{4.15}$$

Inserting this expression of m_x into the first row of Eq. 4.14, we arrive at the equation of motion for m_y,

$$\ddot{m}_y + \alpha(2\omega_H + \omega_M)\dot{m}_y + \omega_H(\omega_M + \omega_H)m_y = (\omega_M + \omega_H)(\gamma H_y)e^{-i\omega t} \tag{4.16}$$

neglecting the second-order terms. Again comparing with the forced damped harmonic oscillator Eq. 4.7, we have the resonance frequency of the in-plane thin film FMR case

$$\omega_0^{in-plane} = \sqrt{\omega_H(\omega_M + \omega_H)} \tag{4.17}$$

Assuming the form of solution to Eq. 4.16 as

$$m_y = \tilde{A}e^{-i\omega t} \tag{4.18}$$

where $\tilde{A}$ is the complex amplitude of m_y and inserting this expression into Eq. 4.15, we have

$$m_x = \frac{-i\omega + \alpha\omega_H}{\omega_M + \omega_H} m_y \tag{4.19}$$

On resonance, with $\alpha \ll 1$, we could approximate the ellipticity, m_x/m_y as

$$\varepsilon = -i\sqrt{\frac{\omega_H}{\omega_M + \omega_H}} = -i\sqrt{\frac{H_0}{4\pi M_s + H_0}} \tag{4.20}$$

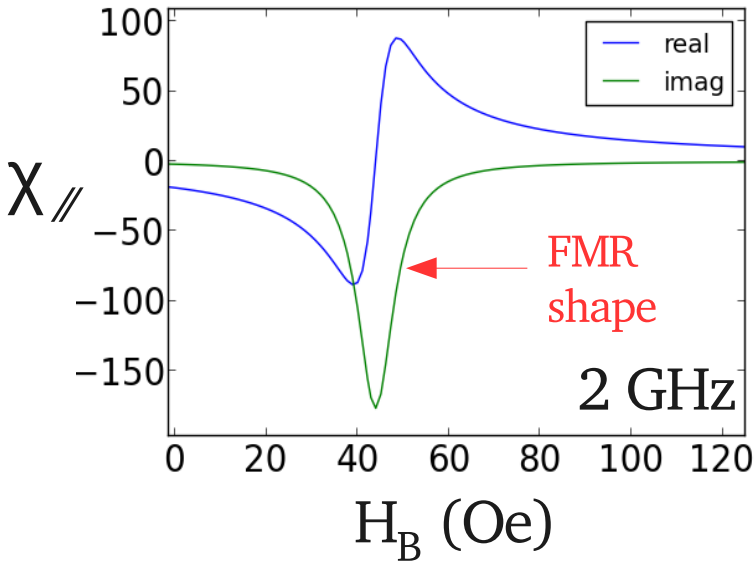

Figure 4.3: Parallel susceptibility $\chi_{\parallel}$ as a function of the bias field H_B: Permalloy at 2 GHz.

from which we can see that the cone angle along the x-axis is considerably smaller than along the y-axis, and the effect is more obvious at low frequencies, where H_0 is much lower than the saturation magnetization $4\pi M_s$. Again using the solution form Eq. 4.18 and substituting it into Eq. 4.16, we can calculate the complex amplitude $\tilde{A}$ of oscillating m_y:

$$\tilde{A} = \frac{\gamma(\omega_M + \omega_H)}{[\omega_H(\omega_M + \omega_H) - \omega^2] - i2\omega\alpha(2\omega_H + \omega_M)} H_y \tag{4.21}$$

For in-plane FMR experiments where the frequency ω is fixed and the external bias field H_B is swept, the effect of the bias field is reflected in the term ω_H in Eq. 4.21, and the parallel susceptibility $\chi_{\parallel}$ takes the form of $M_s\tilde{A}/H_y$. Fig. 4.3 shows the real (blue) and imaginary (green) parts of the parallel susceptibility $\chi_{\parallel}$ as a function of the bias field H_B, at the driving frequency of 2 GHz for Permalloy.

4.3 Power absorption in FMR

Instantaneous power absorbed per unit volume by precessing **M** under driving transverse field H_T is

$$P(t) = -\frac{\partial U}{\partial t} = 2M_T \frac{\partial H_T}{\partial t} \tag{4.22}$$

Power absorption averaged over one period of the oscillation is

$$\langle P \rangle = \frac{\int_0^{\frac{2\pi}{\omega}} P(t)dt}{2\pi/\omega} \tag{4.23}$$

For the in-plane FMR case at frequency ω,

$$\tilde{M}_T(t) = H_0 e^{i\omega t}(\chi'_\parallel + i\chi''_\parallel) = H_0[\cos(\omega t) + i\sin(\omega t)](\chi'_\parallel + i\chi''_\parallel) \tag{4.24}$$

Take the real part of the complex expression,

$$M_T(t) = H_0[\cos(\omega t)\chi'_\parallel - \sin(\omega t)\chi''_\parallel] \tag{4.25}$$

$$H_T(t) = H_0 \cos(\omega t)$$

$$\frac{\partial H_T}{\partial t} = -H_0 \omega \sin(\omega t) \tag{4.26}$$

Thus the instantaneous absorbed power is

$$P(t) = 2M_T \frac{\partial H_T}{\partial t}$$

$$P(t) = -2H_0[\cos(\omega t)\chi'_\parallel - \sin(\omega t)\chi''_\parallel]H_0\omega\sin(\omega t)$$

$$= -2H_0^2\omega[\cos(\omega t)\sin(\omega t)\chi'_\parallel - \sin^2(\omega t)\chi''_\parallel] \tag{4.27}$$

The time integral of $\cos(\omega t)\sin(\omega t)$ is 0.

$$\int_0^{\frac{2\pi}{\omega}} P(t)dt = 2H_0^2\omega\chi''_\parallel \int_0^{\frac{2\pi}{\omega}} \frac{1}{2}[1 - \cos(2\omega t)]dt$$

$$= 2H_0^2\omega\chi''_\parallel \frac{1}{2}t|_0^{\frac{2\pi}{\omega}}$$

$$= 2\pi H_0^2 \chi''_\parallel \tag{4.28}$$

$$\langle P \rangle = 2\pi H_0^2 \chi''_\parallel \omega/(2\pi) = H_0^2 \chi(\omega)''_\parallel \omega \tag{4.29}$$

Eq. 4.29 is the expression of the peak shape in FMR absorption spectra, which is indicated by the red arrow in Fig. 4.3.

Chapter 5

Electron theory of Gilbert damping in fast magnetization dynamics of itinerant ferromagnets

As we discussed in Chap. 4, the second term of the Landau-Lifshitz-Gilbert (LLG) equation,

$$\dot{\mathbf{m}} = -\gamma \mathbf{m} \times \mathbf{H}_{eff} + \alpha \mathbf{m} \times \dot{\mathbf{m}} \tag{5.1}$$

represents the damping torque, parameterized by the value α, which tends to reduce the cone angle of the magnetization precession. The energy and the angular momentum are thus transferred via this term from the precessing spin system to other degrees of freedom. However, the Gilbert damping parameter is phenomenological; there have long been debates on the origin of the Gilbert damping and whether it could describe the general cases of fast magnetization dynamics adequately ([43] and references therein). Various theoretical approaches have been proposed and first-principles calculations [44–51] have been carried out for different types of magnetic systems. However, experimental studies are extremely limited to verify these theories, especially in modern thin-film alloys which are most relevant to the applications in spintronics. In this chapter, we will look into the electron theory of fast dissipative magnetization dynamics in the $3d$ transition metals which are the subject of interest for this thesis, and then present our experimental results, corresponding to the

theory, in three commonly used thin-film metallic ferromagnets for modern applications, Co, $Co_{60}Fe_{20}B_{20}$ and $Ni_{81}Fe_{19}$. We present the first cryogenic measurements of Gilbert damping for these materials in thin-film form, and compare with cryogenic measurements of electrical resistivity. We find good agreement with the electronic model, explaining the thickness and temperature dependence of α.

5.1 The electronic theory of Gilbert damping

The phenomenological damping can be devided into two types: (1) *direct* damping, energy and angular momentum transfer from the precessing spin system to non-magnetic degrees of freedom (and ultimately to heat); (2) *indirect* damping, energy and angular momentum transfer from a specific mode $\mathbf{M}(\mathbf{r},t)$ under consideration to other magnetic degrees of freedom; *e.g.* from the uniform precession mode, the spinwave/magnon with (q = 0, ω_0) to other spinwave modes $\mathbf{M}$ $(\mathbf{q},\omega)$ with different wavevector $\mathbf{q}$ and frequency ω. The indirect damping originates from the first term of the LLG equation 5.1, which is generally nonlinear since $\mathbf{H}_{eff}(\mathbf{r},t)$ depends on $\mathbf{M}(\mathbf{r},t)$ [43]. Nevertheless, at low power and for weak inhomogeneities in the film, indirect damping could be neglected and direct damping is most significant. In this thesis we focus on the *direct* damping and try to derive the Gilbert damping term, using the *effective field theory* [52], in the simplest case of macrospin model/uniform magnetization precession.

5.1.1 Building up the effective field model

First of all, we introduce the observable for the magnetization $\mathbf{M}$ on a mesoscopic scale,

$$\mathbf{M}(\mathbf{r},t) = \frac{1}{V(\mathbf{r})} \sum_{\mathbf{R}\in V(\mathbf{r})} \mathbf{M}_{\mathbf{R}}(t) \tag{5.2}$$

where

$$\mathbf{M}_{\mathbf{R}}(t) = M_{\mathbf{R}}(t)\mathbf{e}_{\mathbf{R}}(t) \tag{5.3}$$

is the atomic magnetic moment with magnitude $M_{\mathbf{R}}(t)$ and orientation $\mathbf{e}_{\mathbf{R}}(t)$ at site $\mathbf{R}$, and V($\mathbf{r}$) is the volume of a mesoscopic part of the sample around $\mathbf{r}$. In the case of uniform

precession, Eq. 5.2 could be reduced to

$$\mathbf{M}(t) = M(t)\mathbf{e}(t) \tag{5.4}$$

In our case of the $3d$ transition metals, the atomic magnetic moment has the major contribution from the itinerant electron spins; the localized orbital moment is negligible.

The *effective field theory* [52] starts with a quantum-mechanical equation of motion for the expectation value of the operator $\widehat{\mathbf{M}}_{\mathbf{R}}(t)$ under strict adiabatic situations, which yields

$$\frac{d\mathbf{e}_{\mathbf{R}}(t)}{dt} = -\gamma \mathbf{e}_{\mathbf{R}}(t) \times \mathbf{H}_{eff,\mathbf{R}}(t) \tag{5.5}$$

where

$$\mathbf{H}_{eff,\mathbf{R}}(t) = -\frac{1}{M_{\mathbf{R}}(t)} \frac{\delta E}{\delta \mathbf{e}_{\mathbf{R}}(t)} \tag{5.6}$$

is the effective field. The energy E is the total electronic energy, since the magnetic moment is mainly electron spin moment. In spin-density-functional theory, the variational $\mathbf{e}_{\mathbf{R}}(t)$ dependent part of E is given by

$$E = \sum_{j\mathbf{k}} f_{j\mathbf{k}}(\{\mathbf{e}_{\mathbf{R}}(t)\}) \varepsilon_{j\mathbf{k}}(\{\mathbf{e}_{\mathbf{R}}(t)\}) \tag{5.7}$$

where j is the electron band index, $\mathbf{k}$ is the wavevector of the electron, f is the probability of the occupation of the electron state $j\mathbf{k}$, and ε is the energy of the state. From Eq. 5.7 we could see that the electron band strucure and energy are dependent on the orientation of the magnetization, which arises from the spin-orbit coupling (SOC). The effective field 5.6 could therefore be calculated from the electronic structure of the material and does not introduce damping into the equation of motion 5.5 under strict adiabatic conditions.

In non-adiabatic situations, we replace the occupation probability $f_{j\mathbf{k}}$ with non-equilibrium occupation number $n_{j\mathbf{k}} \neq f_{j\mathbf{k}}$. Inserting $n_{j\mathbf{k}}$ into Eq. 5.7 and Eq. 5.6, we have

$$\tilde{\mathbf{H}}_{eff,\mathbf{R}}(t) = -\frac{1}{M_{\mathbf{R}}(t)} \sum_{j\mathbf{k}} (n_{j\mathbf{k}} \frac{\partial \varepsilon_{j\mathbf{k}}}{\partial \mathbf{e}_{\mathbf{R}}(t)} + \frac{\partial n_{j\mathbf{k}}}{\partial \mathbf{e}_{\mathbf{R}}(t)} \varepsilon_{j\mathbf{k}}) \tag{5.8}$$

The first term corresponds to the '*breathing Fermi surface*' model. In this scenario, the energies of the electron states $j\mathbf{k}$ in band j change with time, depending on the orientation

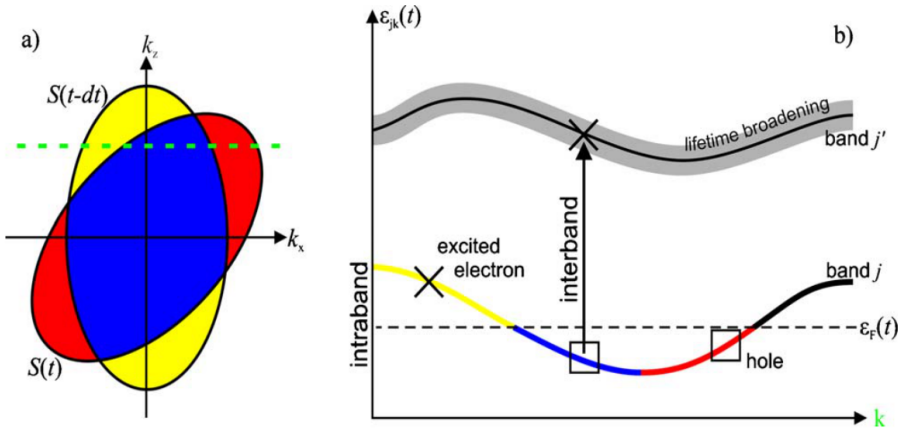

Figure 5.1: Breathing and bubbling Fermi surface models for the electron theory of fast dissipative magnetization dynamics, from Ref. [47]. (a) Illustration of the time-dependent Fermi surface due to the precessing magnetization and spin-orbit coupling (SOC): the yellow and blue electron states are below the Fermi surface at time $t - dt$; the red and blue electron states are below the Fermi surface at time t. (b) electron-band diagram showing the generation of electron-hole pairs within one band (*lower* panel, *breathing* Fermi surface model) and between the bands (*upper* panel, *bubbling* Fermi surface model).

of the magnetization $\mathbf{e_R}(t)$ due to spin-orbit coupling (SOC). Therefore certain electron states fluctuates with time above and below the Fermi surface. As illustrated in Fig. 5.1 (a), the yellow electron states are below the Fermi surface at time $t - dt$ while the red states are below the Fermi surface at time t. The blue states are occupied at all times. The redistribution of the electrons within the band always lags behind the change of the band structure. Therefore, at time t, the yellow states are still occupied, even though they are above the Fermi energy; the red states are vacant, even though they are below the Fermi energy. Electron-hole pairs are thus generated within the electron band j at time t, as illustrated in the lower panel of Fig. 5.1 (b). The electron-hole excitons are subsequently annihilated by scattering events (with phonons, crystal defects, impurities, *etc.*) on the time scale of τ, transferring energy and angular momentum from the precessing spin system to the crystal lattice. The second term in Eq. 5.8 states the change in the electron state occupation probablity caused by the magnetization orientation and is referred to as the '*bubbling Fermi surface*' model, as the electron-hole pairs are generated between electron bands, which is illustrated in the upper panel of Fig. 5.1 (b).

5.1.2 Breathing Fermi surface

Here we take a closer look at the first term of Eq. 5.8. Kambersky [53] used a relaxation time ansatz for the non-equilibrium occupation number $n_{j\mathbf{k}}$,

$$\frac{dn_{j\mathbf{k}}}{dt} = -\frac{1}{\tau_{j\mathbf{k}}}[n_{j\mathbf{k}}(t) - f_{j\mathbf{k}}(t)] \tag{5.9}$$

where the relaxation time $\tau_{j\mathbf{k}}$ is approximated by the electron momentum scattering time τ. Since for fast dynamics in the range of GHz, the time scale of the period of $\mathbf{e_R}(t)$ is $\sim 10^{-9} - 10^{-10}$ s while the momentum scattering time of electrons is in the range of $\sim 10^{-13} - 10^{-14}$ s, we could take the approximation

$$\frac{dn_{j\mathbf{k}}(t)}{dt} = \frac{df_{j\mathbf{k}}(t)}{dt} \tag{5.10}$$

Inserting Eq. 5.10 into Eq. 5.9 and taking $\tau_{j\mathbf{k}}$ to be the electron momentum scatting time τ, we have the solution

$$n_{j\mathbf{k}}(t) = f_{j\mathbf{k}}(t) - \tau \frac{df_{j\mathbf{k}}(t)}{dt} \tag{5.11}$$

Using the chain rule, we have

$$\frac{df_{j\mathbf{k}}(t)}{dt} = \frac{\partial f_{j\mathbf{k}}}{\partial \varepsilon_{j\mathbf{k}}} \sum_{\mathbf{R}} \frac{\partial \varepsilon_{j\mathbf{k}}}{\partial \mathbf{e}_{\mathbf{R}}} \frac{d\mathbf{e}_{\mathbf{R}}}{dt} \tag{5.12}$$

Inserting Eq. 5.12, 5.11 into the first term of Eq. 5.8, we have the equation of motion for $\mathbf{e}_{\mathbf{R}}(t)$ with a damping term having the Gilbert form,

$$\frac{d\mathbf{e}_{\mathbf{R}}}{dt} = -\gamma \mathbf{e}_{\mathbf{R}} \times \mathbf{H}_{eff,\mathbf{R}}(\{\mathbf{e}_{\mathbf{R}}\text{"}\}) + \mathbf{e}_{\mathbf{R}} \times (\sum_{\mathbf{R}'} \overset{\alpha}{=}_{\mathbf{R},\mathbf{R}'} (\{\mathbf{e}_{\mathbf{R}}\text{"}\}) \cdot \frac{d\mathbf{e}_{\mathbf{R}}\text{'}}{dt}) \tag{5.13}$$

where in the first, the driving torque, term, we have

$$\mathbf{H}_{eff,\mathbf{R}}(\{\mathbf{e}_{\mathbf{R}}\text{"}\}) = -\frac{1}{M_{\mathbf{R}}} \sum_{j\mathbf{k}} f_{j\mathbf{k}} \frac{\partial \varepsilon_{j\mathbf{k}}}{\partial \mathbf{e}_{\mathbf{R}}} \tag{5.14}$$

and in the second, the damping torque, term, we have

$$\overset{\alpha}{=}_{\mathbf{R},\mathbf{R}'} (\{\mathbf{e}_{\mathbf{R}}\text{"}\}) = -\gamma \frac{\tau}{M_{\mathbf{R}}} \sum_{j\mathbf{k}} \frac{\partial f_{j\mathbf{k}}}{\partial \varepsilon_{j\mathbf{k}}} \frac{\partial \varepsilon_{j\mathbf{k}}}{\partial \mathbf{e}_{\mathbf{R}}\text{"}} \frac{\partial \varepsilon_{j\mathbf{k}}}{\partial \mathbf{e}_{\mathbf{R}'}} \tag{5.15}$$

From Eq. 5.15 we could see clearly that in the 'breathing Fermi surface' case, the damping parameter is (1) proportional to the electron momentum scattering time τ, thus is called the *conductivity-like* damping; (2) generally not a scalar but a matrix and anisotropic for anisotropic systems; (3) nonlocal. If we simplify the system to the macrospin/uniform precession model, which reduces $\mathbf{e}_{\mathbf{R}}(t)$ to $\mathbf{e}(t)$, we have a scalar Gilbert damping parameter

$$\alpha = -\gamma \frac{\tau}{M_s} \sum_{j\mathbf{k}} \frac{\partial f_{j\mathbf{k}}}{\partial \varepsilon_{j\mathbf{k}}} (\frac{\partial \varepsilon_{j\mathbf{k}}}{\partial \mathbf{e}})^2 \tag{5.16}$$

5.1.3 Bubbling Fermi surface

The second term of Eq. 5.8 represents the interband electron-hole pairs generation. The hopping probability between the bands j and j' is proportional to the bandwidth of the excited state j', which is predicted by the lifetime broadening of band j'. According to the uncertainty principle $\Delta\varepsilon\Delta t \geq \hbar/2$, the bandwidth broadening is inversely proportional to

the scattering time τ of the electron-hole pairs. In contrast to the breathing Fermi surface model, there is no general derivation for the bubbling Fermi surface case. Ref. [54] gives the derivation for a small-angle circular magnetization precession. The damping parameter α from the contribution of this interband electron-hole pair generation-annihilation is *resistivity-like*, roughly proportional to τ^{-1} at not too large τ, as the lifetime broadening of the j' bandwidth decreases with increasing τ, which results in the decrease of the number of the accessible excited states.

5.2 Experimental approach: Gilbert damping and the electron scattering time

In the previous section, we have established the connection between the Gilbert damping paramter α and the electron momentum scattering time τ in itinerant ferromagnets, through the analysis of the effective field theory. Energy and angular momentum are transferred from the precessing spin system to the crystal lattice via the mediation of spin-orbit coupling (SOC). In this effective field model, a scalar α could be expressed in the simplest form as

$$\alpha = c_1\tau + c_2\tau^{-1} \tag{5.17}$$

where the first term is the *conductivity-like* term and the second is the *resistivity-like* term. The coefficients c_1 and c_2 reflect the strength of spin-orbit coupling (SOC), as could be implied from Eq. 5.8 and Eq. 5.16. Now we would like to take an experimental approach and verify Eq. 5.17. While various first-principles calculations [44–51] have been carried out in recent years based on the theories, extremely limited experimental data [55, 56] exist. Ref. [55] measured only bulk samples, therefore the resistivity size effects are not relevant; the authors also measured only the FMR linewidth at one frequency, from which the estimation of the damping paramter α was very inaccurate. Ref. [56] measured only Permalloy samples in a very small frequency range (< 2 GHz), insufficient to separate α from ΔH_0. For itinerant ferromagnets, we estimate the electron momentum scattering time

τ using the simple Drude model,

$$\sigma = \rho^{-1} = \frac{ne^2\tau}{m_e} \tag{5.18}$$

where σ is the electrical conductivity, ρ is the resistivity, τ is the electron scattering time, n is the electron volume density, and m_e is the effective electron mass. Since σ is proportional to τ and ρ is proportional to τ^{-1}, we could write Eq. 5.17 in the following form with observables directly accessible by experiments:

$$\alpha = c_\sigma\sigma + c_\rho\rho + \alpha_0 \tag{5.19}$$

We introduced the offset α_0 as a fitting parameter. To observe the damping parameter α as a function of the resistivity ρ, we have to vary the resistivity ρ as a control parameter by altering the electron mean free path λ in the material. We took two approaches in our thin film samples: (1) to change the thickness t_{FM} of the ferromagnetic (FM) layer; the averaged electron mean free path λ is reduced compared with the bulk value λ_0 when t_{FM} decreases, due to the enhanced surface scattering and could be estimated according to the Fuchs model [57]; (2) to decrease the temperature of the sample, which increases the electron mean free path λ_0 in the bulk. Therein we measure $\alpha(T, t_{FM})$ and $\rho(T, t_{FM})$, and try to fit α as a function of ρ.

5.2.1 Instrumentation: temperature-dependent α and ρ

In this part we review briefly the techniques for measuring the resistivity ρ and the Gilbert damping parameter α in thin film samples.

• The van der Pauw technique

First we introduce the temperature-dependent van der Pauw technique for measuring $\rho_{t_{FM}}(T)$. The experimental setup is outlined in Fig. 5.2. We use a one-stage cold head enclosed in a vacuum chamber (represented by the yellow rectangular frame in Fig. 5.2), cooled by the Helium compressor, to reach the cryogenic temperature of 25 K. The sample mount, which is a block of copper, is attached to the top of the cold head with sufficient

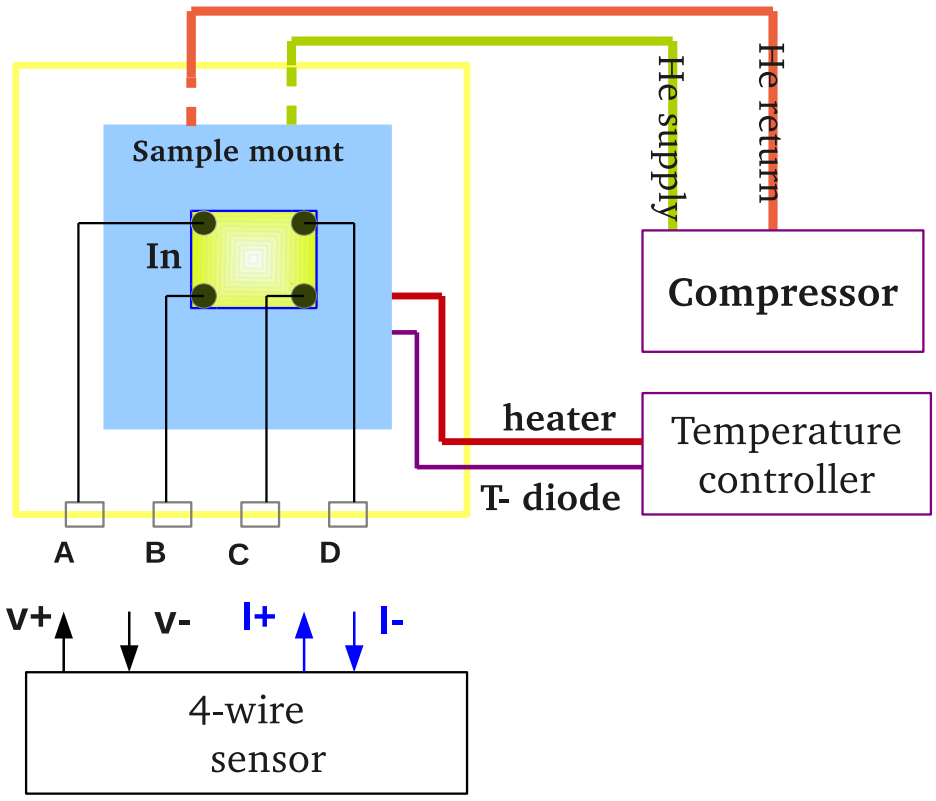

Figure 5.2: Temperature-dependent measurement of resistivity using the Van der Pauw technique. A, B, C, D are the four BNC ports on the vacuum chamber (represented by the yellow rectangular frame) for the 4-wire sheet resistance measurement. The 4 wires are soldered on the film by Indium. The sample mount is a copper block attached to the cold head. The film is mounted using thermal paste.

thermal contact. We use a programmable temperature controller with heater and temperature sensor to control the sample temeprature T over the range of 25 K - 300 K. The resistive heater and Pt temperature sensor wires are sent to the sample mount via the electrical feedthrough on the vacuum chamber. The sample FM thin film is mounted on the copper block with thermal paste on the back side of the Si substrate, to ensure thermal conductance between the sample mount the FM film. At the four corners of the rectangular thin film sample, we solder fine gauge Cu wires using In to make the electrical contacts. In has a low melting point and thus moderate temeprature of the soldering pen is required, which helps to reduce the influence of heat on the FM layer.

The van der Pauw technique [58] is a modification of the conventional four-probe method for measuring the resistivity of a bar-shaped sample, which allows the measurement of sheet resistance $R_S = \rho/t$ on arbitrary-shaped thin film samples. There are, however, some restrictions:

1. The contacts are on the edge of the sample. If the thickness t of the sample is not negligible, the contacts should be very thin vertical lines across t.

2. The contacts are point-like or have negligible area compared with the film surface.

3. The film is homogeneous in thickness and continuous.

It is shown in Ref. [58] that

$$\exp(-\pi\frac{R_{AB,CD}}{R_S}) + \exp(-\pi\frac{R_{BC,AD}}{R_S}) = 1$$

where

$$R_{AB,CD} = \frac{V_D - V_C}{i_{AB}}.$$

From the above equations, we have

$$R_S = \frac{\pi}{\ln 2} f(\frac{R_{AB,CD}}{R_{BC,DA}}) \frac{R_{AB,CD} + R_{BC,DA}}{2} \tag{5.20}$$

where f is the *correction* function and could be calculated from the relation:

$$\frac{R_{AB,CD} - R_{BC,DA}}{R_{AB,CD} + R_{BC,DA}} = \frac{f}{\ln 2} arccosh(\frac{\exp(\ln 2/f)}{2}) \tag{5.21}$$

It is advisable to take as many permutations as possible (up to eight) of the four contacts during the measurement to improve the accuracy of the measured sheet resistance, since in general V_{AB} and V_{BA} are not necessarily equal due to various factors, such as the thermoelectric effects, and averaging the two values can eliminate the extrinsic influences. Therefore, we take the $R_{AB,CD}$ value as $\frac{1}{2}(\frac{V_D-V_C}{i_{AB}}+\frac{V_C-V_D}{i_{AB}})$. Keeping this in mind, we have

$$\begin{aligned} R_{S1} &= \tfrac{\pi}{\ln 2} f(\tfrac{R_{AB,CD}}{R_{BC,DA}}) \tfrac{R_{AB,CD}+R_{BC,DA}}{2} \\ R_{S2} &= \tfrac{\pi}{\ln 2} f(\tfrac{R_{CD,AB}}{R_{AD,BC}}) \tfrac{R_{CD,AB}+R_{AD,BC}}{2} \end{aligned} \tag{5.22}$$

and finally we have the sheet resistance

$$R_S = \frac{R_{S1}+R_{S2}}{2} \tag{5.23}$$

Instead of having the direct relationship between the sheet resistance and the resistivity $R_S = \rho/t$ for a single-layer film, when we have a multilayered film with the heterostructure of nonmagnetic(NM)/FM/NM, additional efforts have to be made to extract the resistivity ρ of the FM layer. The analysis is based on the Fuchs model [57] and is briefly summarized as follows. If we have a series of thin film samples with the layer structure of $\mathrm{NM_1(t_1)/FM(t_{FM})/NM_2(t_2)}$, where we keep $\mathrm{t_1}$ and $\mathrm{t_2}$ constant but vary the thickness of the FM layer $\mathrm{t_{FM}}$, the sheet conductance, $G_S(t_{FM}) = 1/R_S(t_{FM})$, of the sample could be fitted with

$$G_S(t_{FM}) = G_{S,FM}(t_{FM}) + G_0 \tag{5.24}$$

where G_0 is the constant contribution from the $\mathrm{NM_1}$ and $\mathrm{NM_2}$ layers with the fixed thicknesses, and $G_{S,FM}(t_{FM}) = t_{FM}/\rho_{FM}(t_{FM})$. The Fuchs model states that for a single-layer metallic thin film, the resistivity differs from the bulk material if the film thickness is comparable with the electron mean free path λ_0 in the bulk, due to the enhanced surface scattering. The detailed derivation is neatly given in Ref. [57] and here we present only the final result for the reduced conductivity σ compared with the bulk value σ_0 due to random scattering at the film surface (no specularity):

$$\frac{\sigma}{\sigma_0} = 1 - \frac{3}{8\kappa} + \frac{3}{4\kappa}\int_0^{\pi} \sin^3\theta |\cos\theta| \exp(-\kappa/|\cos\theta|) d\theta \tag{5.25}$$

with θ denoting the angle between the electron trajectory and the film normal, and

$$\kappa \equiv t/\lambda_0 \tag{5.26}$$

where t is the thickness of the metallic single-layer film and λ_0 is the electron mean free path in the bulk material. To estimate λ_0, we need to know the Fermi velocity v_F of the electrons in a given material and calculate according to the simple Drude model

$$\lambda_0 = v_F \tau = \frac{v_F m^*}{\rho_0 n e^2} \tag{5.27}$$

from which we see a term that is often tabulated for individual materials in the bulk.

$$\lambda_0 \rho_0 = \frac{v_F m^*}{n e^2} \tag{5.28}$$

Based on Eq. 5.24, Eq. 5.25 and Eq. 5.28, we could then fit the experimental data $G_S(t_{FM})$ and extract $\rho_{FM}(t_{FM})$. See Fig. 5.3 for example.

For the temperature-dependent case where we have one sample with fixed t_{FM}, the analysis is still based on the Fuchs model, with the essential equations:

$$G_S(T) = G_{S,FM}(T) + G_0(T) \tag{5.29}$$

and

$$\kappa = t/\lambda_0(T) \tag{5.30}$$

$$\lambda_0(T)\rho_0(T) = \frac{v_F m^*}{n e^2} \tag{5.31}$$

for both the FM and NM layers. The Fuchs function Eq. 5.25 still applies with the variable κ, where the thickness t is fixed but the mean free path in the bulk λ_0 changes with temperature T. Since the Fermi velocity v_F does not have a strong dependence on T, the tabulated value of $v_F m^*/(ne^2)$ applies to both the t_{FM} and the T cases.

• Measurement of the Gilbert damping parameter α using broadband FMR

The analytical solution of in-plane ferromagnetic resonance (FMR) to the Landau-Lifshitz-Gilbert (LLG) equation has been discussed in detail in Chap. 4. Here we establish

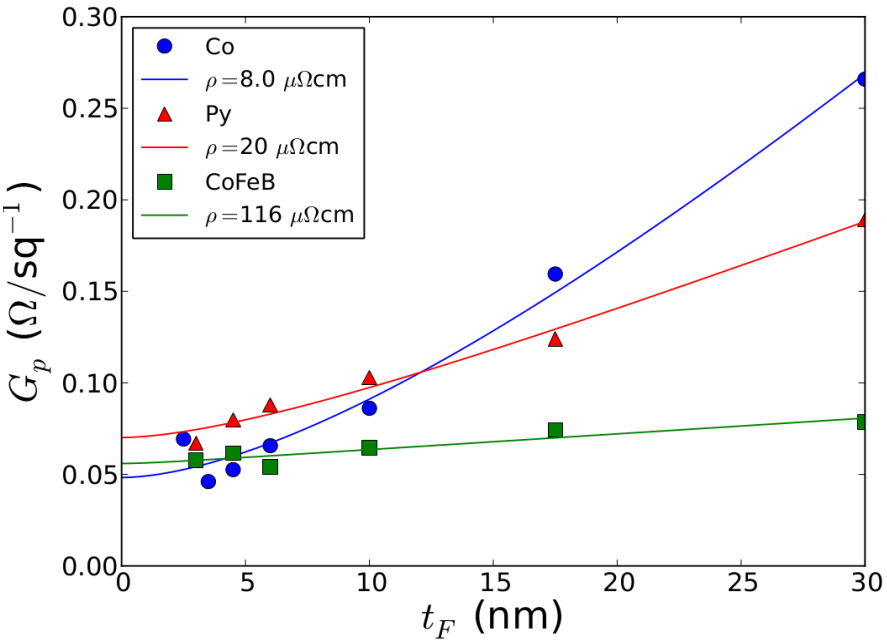

Figure 5.3: Sheet conductance as a function of the FM layer thickness t_{FM} for Co, $Ni_{81}Fe_{19}$ and $Co_{60}Fe_{20}B_{20}$. The parameters show the fitted bulk resistivities which are in reasonable agreement with tabulated values.

the relationship between the FMR spectrum linewidth with the damping parameter α. Eq. 4.21 expresses the complex amplitude of m_y, from which we could measure the parallel susceptibility by $\chi_\parallel = M_y/H_y = M_S\tilde{A}/H_y$:

$$\chi_\parallel = \frac{1}{4\pi}\frac{\omega_M(\omega_M+\omega_H)}{-\omega^2+\omega_H(\omega_M+\omega_H)-i2\alpha\omega(\omega_M+2\omega_H)} \tag{5.32}$$

where $\omega_M \equiv \gamma 4\pi M_S$ and $\omega_H \equiv \gamma H_B$. To look into the linewidth of the imaginary part of $\chi_\parallel$, which is the shape of the FMR spectrum as we pointed out in Fig. 4.3, we first simplify Eq. 5.32 by introducing the reduced variables: (1) the reduced field $h \equiv \omega_H/\omega_M$; and (2) the reduced frequency $\Omega \equiv \omega/\omega_M$. Deviding both the top and bottom parts of Eq. 5.32 by ω_M^2 and inserting the reduced variables, we have

$$\chi_\parallel = \frac{1}{4\pi}\frac{1+h}{-\Omega^2+h(1+h)-i2\alpha\Omega(1+2h)} \tag{5.33}$$

If we drive the FM thin film at the fixed frequency ω (reduced frequency Ω) and sweep the field H_B, we would see a peak in the imaginary part of Eq. 5.33 at the resonance field H_0 (reduced field h_r, and the fixed frequency $\Omega^2 = h_r(1+h_r)$). Near the resonance we could expand the reduced field as $h = h_r + \Delta h$. Inserting into Eq. 5.33 we have the approximation

$$\begin{aligned}\chi_\parallel &\simeq \frac{1}{4\pi}\frac{1+h_r}{\Delta h(2h_r+1)-i2\alpha\Omega(1+2h_r)} \\ &= \frac{1}{4\pi}\frac{h_r+1}{2h_r+1}\frac{\Delta h - i\alpha\Omega}{(\Delta h)^2+\alpha^2\Omega^2}\end{aligned} \tag{5.34}$$

Therefore we have the imaginary part of the parallel susceptibility

$$\chi_\parallel{}'' = \frac{1}{4\pi}\frac{h_r+1}{2h_r+1}\frac{-i\alpha\Omega}{(\Delta h)^2+\alpha^2\Omega^2} \tag{5.35}$$

We could see immediately from Eq. 5.35 that the full-width-half-maximum (FWHM) of $\chi_\parallel{}''$ is

$$\Delta h_{1/2} = 2\alpha\Omega \tag{5.36}$$

Therefore we have the full-width-half-maximum (FWHM) of the field-swept in-plane FMR,

$$\Delta H_{1/2} = 2\alpha\omega/\gamma \tag{5.37}$$

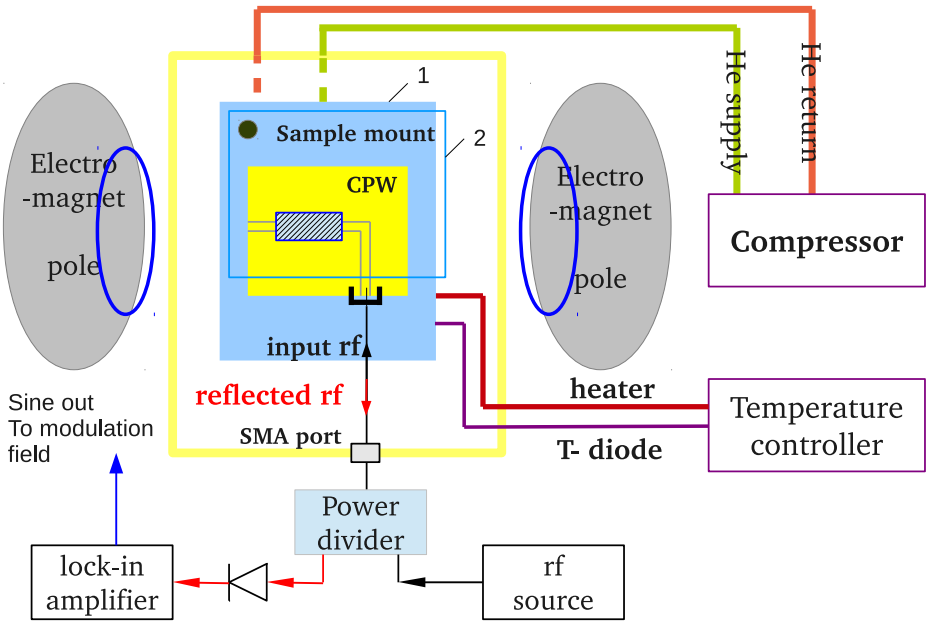

Figure 5.4: The setup for temperature-dependent measurement of the Gilbert damping parameter α. The yellow rectangular frame represents the vacuum chamber. 1 and 2 are the copper blocks as parts of the sample mount. The blue circles are the modulation field coils which are controlled by the lock-in amplifier, indicated by the blue arrow.

and the peak-peak linewidth is $\frac{1}{\sqrt{3}}\Delta H_{1/2}$. According to Eq. 5.37, the FMR linewidth is a linear function of the frequency ω with the coeffient of $2\alpha\gamma$. For a certain material, the gyromagnetic ratio γ is a constant which is often tabulated. Therefore we could fit the FMR linewidth as a linear function of the driving frequency, then extract the damping parameter α from the slope.

Fig. 5.4 illustrates the experimental setup of the T-dependent broadband FMR measurement for extracting the damping parameter α. The α measurements are taken separately after the resistivity measurements. The temperature control part is explained in the T-dependent resistivity measurements. The only difference is that we use an additional copper block (2 in Fig. 5.4) to press the sample/coplanar waveguide (CPW) assembly against

the sample mount (1 in Fig. 5.4) for better thermal contact. For the FMR part, we use the rf source to generate input rf signal in the frequency range of 2-18 GHz. The input rf signal is sent to one port of the power divider which is connected to the SMA port on the vacuum chamber. Inside the chamber, an SMA cable connects the SMA port and the CPW. The sample sits on top of the CPW with the film side down. The center conductor of the CPW is parallel with the DC bias field H_B which is applied by the electromagnet, and exerts an rf magnetic field on the sample, transverse to H_B. The configuration of the sample and the magnetic fields is then the in-plane FMR case. The rf signal is reflected from the sample to the same SMA cable, transmits through the SMA port and the power divider and finally detected by the crystal detector. The detected signal is then sent to the lock-in amplifier (LIA). Using the low frequency ($\sim$160 Hz) modulation field superimposed on H_B, the LIA detects only the ac signal with the modulation frequency and therefore the signal-noise ratio is significantly enhanced [59]. Instead of giving directly the reflected rf signal power P (as calculated in Eq. 4.29), the LIA takes the field derivative of P, which gives the FMR lineshape as shown in Fig. 5.5(a). The lineshape could be fitted using the Lorentzian function

$$\Re\left(\frac{1}{(x-x_0)+i\Delta x}e^{i\theta}\right) \tag{5.38}$$

where x is the variable, x_0 is the peak center, Δx is the half-width-half-maximum (HWHM), and θ is the phase. By plotting Δx as a function of the input frequency f, we could extract the damping parameter α, as shown in Fig. 5.5(b).

5.2.2 The samples

The sample structure is illustrated in Fig. 5.6, which is Ta (5 nm)/ Cu (5 nm)/FM (t_{FM} nm)/ Cu (3 nm)/ Al (3 nm). t_{FM} spans the range of 2.5 nm to 30 nm, as listed in the right panel of Fig. 5.6. The films are magnetron sputtered on thermally oxidized silicon substrates. These films were deposited at SPINTEC, by S. Auffret, as reference layers for a separate study on spin pumping [60]. The seed layer Ta (5 nm)/ Cu (5 nm) improves the homogeneity of the film and its adhesion to the substrate, and the cap layer Cu (3 nm)/

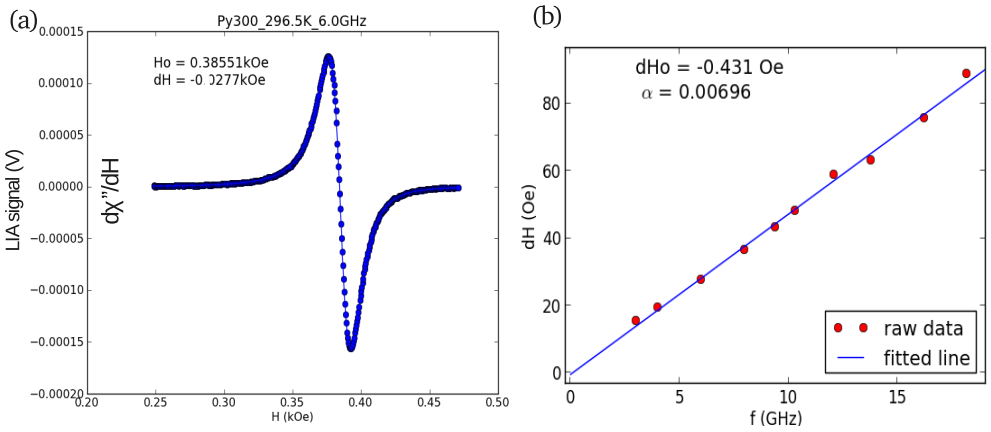

Figure 5.5: (a) FMR spectrum, $Ni_{81}Fe_{19}$ 30 nm at 6 GHz, room temperature. (b) $Ni_{81}Fe_{19}$ 30 nm, room temperature, α from the slope of $\Delta H_{1/2}(f)$.

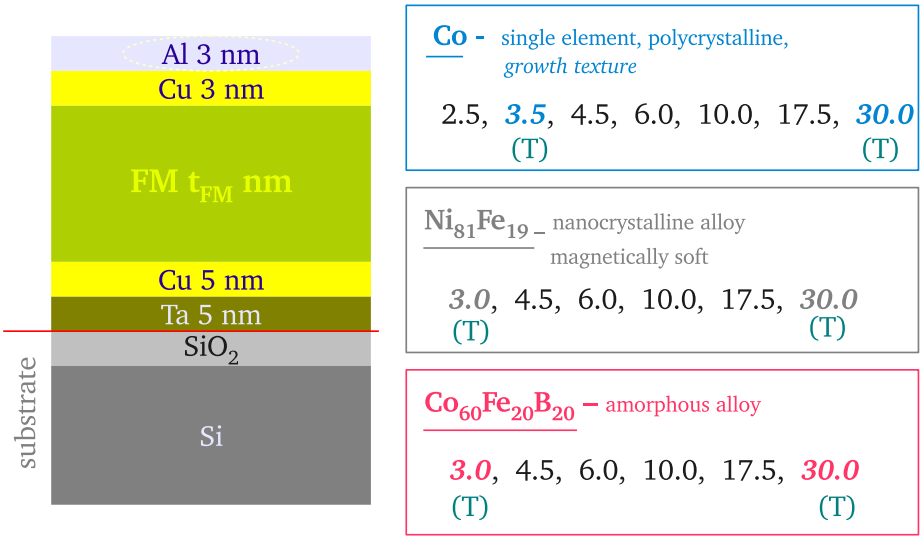

Figure 5.6: Samples for $\alpha(\rho)$. *Left* panel: the layers structure; the films are magnetron sputtered on thermally oxidized silicon substrates. Right panel: three materials for the FM layer, at various thicknesses t_{FM}; (T) indicates the thickness at which the temperature-dependent experiments are done.

Al (3 nm) protects the film from oxidation. We use the light element Al as the capping layer to exlude any enhanced damping from the spin pumping effect. The top and bottom interfaces of the FM layer are both Cu interfaces. We choose three different FM materials which are most representative for the applications in spintronics and have distinctive micro-/crystal structures. Co is a pure $3d$ transition metal which has the *hcp* crystal structure in its bulk form; in the sputtered polycrystalline films, it exhibits a transition from the *fcc* $\{111\}$ growth texture to the *hcp* $\{0001\}$ texture at a few nm. Co is widely used in perpendicular anisotropy applications due to its strong magnetocrystalline anisotropy along the $\langle 0001 \rangle$ directions. $Ni_{81}Fe_{19}$ is the classical soft magnetic binary alloy, with near-zero magnetostriction and anisotropy. The sputtered films have very fine grain size, in the range of several nm, which borders on amorphous material. $Co_{60}Fe_{20}B_{20}$ is amorphous and has high resistivity because of the Boron atoms. Due to the significantly different crystal structures, the spin-orbit coupling (SOC) strength in these three materials are different, with Co having the highest SOC as could be implied from the high magnetocrystalline anisotropy. At room temperature ($\sim$300 K), all the samples are measured for their resistivity ρ_{FM} and the damping parameter α, using the van der Pauw technique and the broadband FMR respectively, as explained in the previous '*instrumentation*' section. The films with the lowest and the highest thicknesses for each material are selected for the temperature-dependent ρ_{FM} and α measurements, since they are expected to demonstrate the most distinguishable behavior at the two limits of the thickness series.

5.2.3 Results and discussion

In this section we present our experimental results of the damping α as a function of the resistivity ρ_{FM}, based on the measurements at various FM layer thickness t_{FM} and temperature T, for the material systems of Co, $Ni_{81}Fe_{19}$ and $Co_{60}Fe_{20}B_{20}$.

- **Room temeprature $\sim$ 300 K, t_{FM} series**

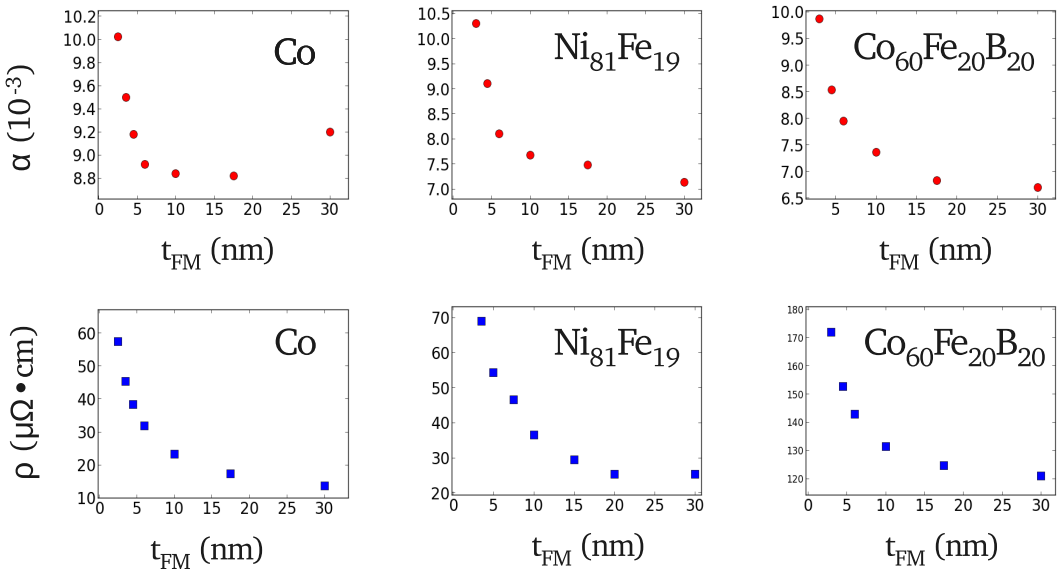

Figure 5.7: α and ρ_{FM} dependence on FM layer thickness t_{FM} at room temperature 300 K, for Co, $Ni_{81}Fe_{19}$ and $Co_{60}Fe_{20}B_{20}$.

Fig. 5.7 shows the dependence of the damping parameter α (upper panel) and the FM layer resistivity ρ_{FM} (lower panel) on the thickness t_{FM} of the FM layer. For all the three materials, we see very similar trends in both the damping parameter α and the resistivity ρ_{FM}, with high values at low t_{FM} and low values at larger film thicknesses, which converge as the FM layer thickness approaches the bulk limit. The only exception is the damping α of Co, which shows a slight increasing trend above $t_{FM} = 15$ nm. However if we plot α as a function of ρ as demonstrated in Fig. 5.8, distinctive characteristics emerge among the three material systems.

In Co, we see a clear cross-over from the *conductivity*-like damping to *resistivity*-like damping; $Ni_{81}Fe_{19}$ exhibits *resistivity*-like damping at high resistivity values with a broad minimum of α at low resistivities; $Co_{60}Fe_{20}B_{20}$ shows an almost linear dependence, *i.e.* the *resistivity*-like damping dominates at all available resistivity values for this high-resistivity material. Connecting these results with the theoretical models in the first section

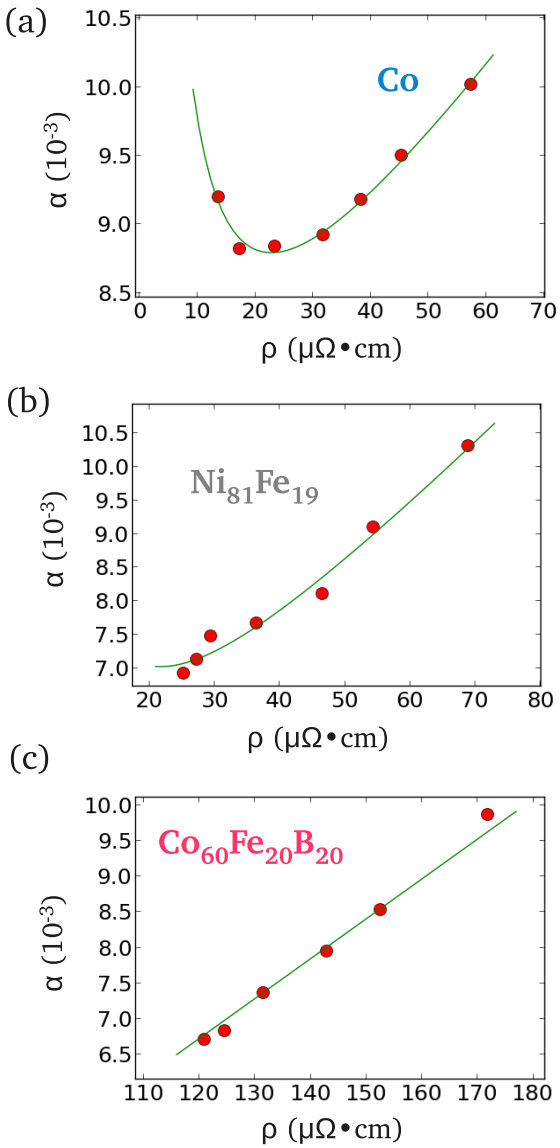

Figure 5.8: α as a function of ρ at 300 K for t_{FM} series: (a) Co; (b) $Ni_{81}Fe_{19}$; (c)$Co_{60}Fe_{20}B_{20}$. The red dots are experimental data and the green curve is the fitted curve from Eq. 5.19.

of this chapter, we could attribute the *resistivity*-like damping to the *interband* electron-hole pairs generation and the *conductivity*-like damping to the *intraband* electron-hole pairs generation. In the case of **Co**, we see a *conductivity*-like damping at high t_{FM} (low ρ_{FM}) which indicates strong SOC and *intraband* contribution. This is consistent with the relatively strong perpendicular anisotropy in Co, possibly due to the *hcp* {0001} texture in the thick film, via the Bruno model which relates the SOC with the anisotropy energy by [61, Chap.7.9]

$$\Delta E_{SO} = \zeta[\langle \mathbf{L}\cdot\mathbf{S}\rangle_{hard} - \langle \mathbf{L}\cdot\mathbf{S}\rangle_{easy}] = \frac{\zeta}{4\mu_B}(m_O^{easy} - m_O^{hard}) \tag{5.39}$$

where ΔE_{SO} is the difference in the spin-orbit energy for the magnetization to lie in the *easy*- and *hard*-axes, *i.e.* the anisotropy energy, and ζ is the spin-orbit coupling strength. μ_B is the Bohr magneton $e\hbar/(2m_e)$ and m_O is the orbital moment. On the other hand, the resistivity is low in the thick Co film, which corresponds to a relatively long electron scattering time τ. In the 'bubbling' Fermi surface model which contributes to the *resistivity*-like damping, the probability of *interband* electron-hole pairs generation is proportional to the lifetime broadening of the excited electron state, $\propto \tau^{-1}$. In the case of large τ, the *resistivity*-like damping is thus supressed. For $\mathbf{Ni}_{81}\mathbf{Fe}_{19}$ and $\mathbf{Co}_{60}\mathbf{Fe}_{20}\mathbf{B}_{20}$ it is recognized that significant band mixing occurs, from first-principles electron band structure calculations [49, 51], which implies a dominant contribution to the direct Gilbert damping from the interband electron-hole pairs generation. In the meantime, the lack of magnetic anisotropy in these two materials indicates that SOC is weak, *i.e.* the direction of the magnetization has minimal influence on the electron band energy. Therefore, the 'breathing' Fermi surface would fluctuate with time only at a negligible amplitude and thus the *conductivity*-like damping is diminished. Furthermore, in the case of $Co_{60}Fe_{20}B_{20}$, the resistivity is so high that the short electron scattering time would introduce large lifetime broadening of the excited states of the electrons, which further increases the contribution from the interband electron-hole pairs generation and therefore the *resistivity*-like damping.

- **T series for the thinnest and the thickest films**

Before we proceed to the discussion of T-dependent damping $\alpha(T)$ and resistivity $\rho_{FM}(T)$, some background should be introduced on the T-dependent effective saturation magnetization $4\pi M_s^{eff}(T)$ measured by the in-plane FMR and the analysis of T-dependent anisotropy. This step is important since we have already seen the influence of the SOC on the Gilbert damping behavior; and the anisotropy reflects the SOC, as pointed out by Eq. 5.39.

First we introduce the temperature dependence of anisotropy. At zero temperature in a ferromagnetic meterial, the spins at various locations are perfectly parallel due to the strong exchange interaction between the electrons. However at finite temperatures, the direction cosines of a local spin cluster, (β_1, β_2, β_3), deviate from the average spontaneous magnetization, and the deviations increase with increasing temperature. We could express the anisotropy at temperature T as

$$E_a(T) = \sum_n K^{(n)}(0)\langle nth\ power\ angular\ function\rangle \tag{5.40}$$

where E_a is the anisotropy energy, $K^{(n)}(0)$ is the anisotropy constant at 0 K for the nth power angular function, and $\langle\rangle$ is the average of the angular function for all the spin clusters. To give examples of the angular function, we list the two most typical magnetocrystalline anisotropies as follows:

uniaxial anisotropy:

$$E_a = K_{u1}\sin^2\theta + K_{u2}\sin^4\theta + K_{u3}\sin^6\theta + \ldots \tag{5.41}$$

where θ is the angle between the *easy*-axis and the magnetization direction;

cubic anisotropy:

$$E_a = K_1(\alpha_1^2\alpha_2^2 + \alpha_2^2\alpha_3^2 + \alpha_3^2\alpha_1^2) + K_2\alpha_1^2\alpha_2^2\alpha_3^2 + K_3(\alpha_1^2\alpha_2^2 + \alpha_2^2\alpha_3^2 + \alpha_3^2\alpha_1^2)^2 + \ldots \tag{5.42}$$

where (α_1, α_2, α_3) are the direction cosines of the magnetization with respect to the three cube edges.

In both cases, only the leading two terms have nonnegligible contribution to E_a, usually

with the dominant contribution from the first term. We could see from these expressions that in the uniaxial anisotropy case, K_{um} corresponds to the $2m$th power angular function and in the cubic anisotropy case, K_m corresponds to the $(2+2m)$th power angular function. Another special case worth mentioning is the anisotropy energy in the {111} plane of a close-packed structure, when the magnetization is confined to the {111} plane. This is the case for most of our sputtered soft magnetic thin films. The derivation is given in Ref. [4, Chap.12.1, P.252] and here we present the final form of the anisotropy energy:

$$E_a = \frac{K_1}{4} + \frac{K_2}{108}(1 - \cos 6\theta) + \frac{K_3}{16} + \dots \tag{5.43}$$

in which only the K_2 (n = 6) term has angular dependence and contributes to the anisotropy energy.

According to an accurate calculation for the nth power function, based on the random walk function of a unit vector on a spherical surface about a symmetry axis [62], we have [4, Chap.12.3, P.273]

$$\langle K^{(n)}(T)\rangle \propto M_s(T)^{n(n+1)/2} \tag{5.44}$$

Therefore for $n = 2$ (uniaxial anisotropy), we have

$$\frac{K_u(T)}{K_u(0)} = [\frac{M_s(T)}{M_s(0)}]^3 \tag{5.45}$$

for $n = 4$ (K_1 in cubic anisotropy), we have

$$\frac{K_1(T)}{K_1(0)} = [\frac{M_s(T)}{M_s(0)}]^{10} \tag{5.46}$$

and for $n = 6$ (K_2 in cubic anisotropy), we have

$$\frac{K_2(T)}{K_2(0)} = [\frac{M_s(T)}{M_s(0)}]^{21} \tag{5.47}$$

According to Eq. 5.44, by finding out the power law dependence of the temperature-dependent anisotropy constant on the temperature-dependent saturation magnetization,

$$\log K^{(n)}(T) = \frac{1}{2}n(n+1)\log\frac{M_s(T)}{M_s(0)} + \log K^{(n)}(0)(const.) \tag{5.48}$$

we could obtain the symmetry of the anisotropy in the FM system.

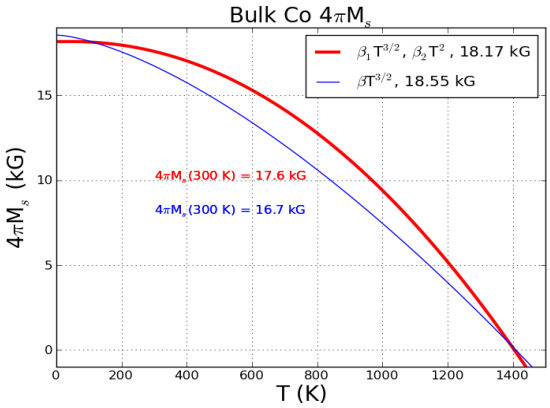

Figure 5.9: T-dependent $4\pi M_s$ in bulk Co, calculated from tabulated data points.

Next we look into the measurement of the anisotropy and saturation magnetization by in-plane FMR. According to the analysis carried out in Chap.4.2, we have the following Kittel relation:

$$\omega_0^{in-plane} = \sqrt{\omega_H(\omega_M + \omega_H)} \tag{5.49}$$

where $\omega_M \equiv \gamma 4\pi M_S$ and $\omega_H \equiv \gamma H_B$. In Chap.4.2, we treated a system consisting of isotropic material, therefore the ω_M term comes from the out-of-plane demagnetizting field and the ω_H term is attributed to the DC bias field only. However if we have in the film out-of-plane anisotropies (from the film growth texture or the surface anisotropy), this adds extra terms to the out-of-plane effective field H_x^{eff}, and in the Kittel relation we have $\omega_H[\omega_M + \omega_{H_k} + \omega_H]$ instead of $\omega_H(\omega_M + \omega_H)$. Therefore the effective saturation magnetization of the thin film $4\pi M_s^{eff} = 4\pi M_s - 2K/M_s$, where M_s is the saturation magnetization of the bulk material and K is the anisotropy constant. By measuring $4\pi M_s^{eff}(T)$ using T-dependent in-plane FMR and taking $4\pi M_s(T)$ from tabulated values, we have

$$K(T) = \frac{1}{2}[4\pi M_s(T) - 4\pi M_s^{eff}(T)] \times M_s(T) \tag{5.50}$$

Further analyzing the power law dependence of $K(T)$ using Eq. 5.48, we could infer the symmetry or origin of the anisotropy in the film. Fig. 5.10 gives such an example.

In Fig. 5.10 (a) and (b) we plot the effective saturation magnetization $4\pi M_S^{eff}$ as

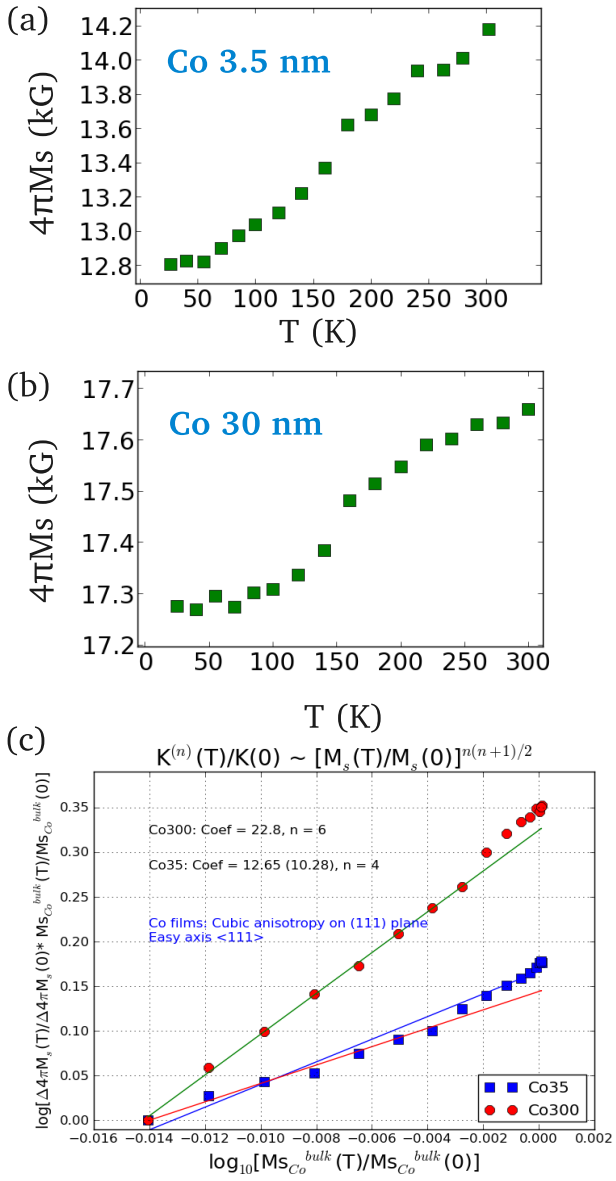

Figure 5.10: T-dependent perpendicular anisotropy in Co thin films. (a) Effective saturation magnetization $4\pi M_S^{eff}$ of Co 3.5 nm thin film measured by in-plane FMR over the temperature range of 27 K - 300 K; (b) Effective saturation magnetization $4\pi M_S^{eff}$ of Co 30 nm thin film measured by in-plane FMR over the temperature range of 27 K - 300 K; (c) T Power law of the out-of-plane anisotropy in the 3.5 nm and 30 nm Co films. 30 nm Co: slope = 22, n $\sim$ 6; 3.5 nm Co: slope = 12, n $\sim$ 4

Table 5.1: Temperature-dependent $4\pi M_s$ for bulk *hcp* Co.

T (K)	$4\pi M_s$ (kG)
0.0	18.17
0.15	18.17
300	17.6
1404.15	0

a function of T for the 3.5 nm and 30 nm Co films, respectively. Fig. 5.9 shows the T-dependent saturation magnetization in bulk Co, calculated using tabulated data points in Table 5.1 with the temperature dependence model $M_s(T)/M_s(0) = 1 - \beta_1 T^{3/2} - \beta_2 T^2$, where $\beta_1 = -4.94 \times 10^{-6}\ K^{-3/2}$ and $\beta_2 = 6.39 \times 10^{-7}\ K^{-2}$. The fitting parameters are in reasonable agreement with Ref. [63] ($\beta_1 = -1.5 \times 10^{-6}\ K^{-3/2}$). According to the analysis in the previous paragraph, we infer from Fig. 5.10 (a) and (b) that both the Co films have a strongly T-dependent perpendicular anisotropy, possibly from the crystalline anisotropy due to the growth texture in the thin film. The Co 3.5 nm film sees a decrease of 2.4 kG in $4\pi M_S^{eff}$ over the complete temperature range while the 30 nm film sees a decrease of 0.4 kG. Comparing these two figures, we would expect a stronger SOC in the 3.5 nm Co film. Fig. 5.10 (c) plots the change in $4\pi M_S^{eff}$ using the T dependent power law for both the 3.5 nm and the 3 nm films, based on Eq. 5.48. We found $n = 6$ for $K^{(n)}$ in the Co 30 nm film, which is consistent Eq. 5.43. For the 3.5 nm film, $n \sim 4$, which could be explained by a mixture of $n = 2$ (uniaxial out-of-plane anisotropy, probably due to the surface anisotropy K_s) and $n = 6$ (from the {111} texture). We conclude from this discussion of T-dependent $4\pi M_s^{eff}$ in Co films that the SOC increases significantly with decreasing temperature, especially in the 3.5 nm Co film. Similar $4\pi M_s^{eff}(T)$ and $K^{(n)}(T)$ analysis were carried out for $Ni_{81}Fe_{19}$ and $Co_{60}Fe_{20}B_{20}$; no significant T dependence of K were found for these two materials, except in the $Co_{60}Fe_{20}B_{20}$ 3 nm sample, where $n = 2$ indicating a uniaxial surface anisotropy.

Fig. 5.11 summarizes the relationship between the damping parameter α and the resistivity ρ_{FM} by varying the sample temperature, for the thinnest and the thickest films in

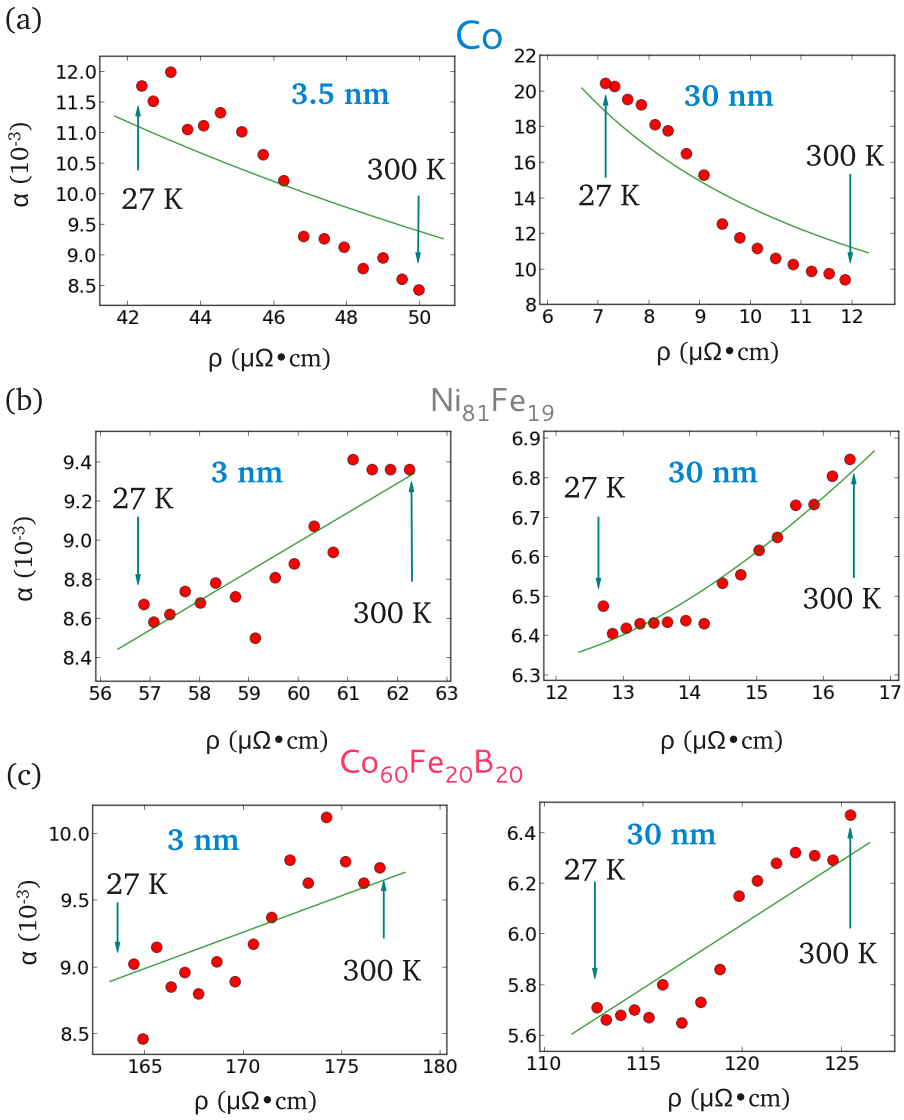

Figure 5.11: α as a function of ρ at various T in the range of 27 K - 300K, for (a) Co, (b) $Ni_{81}Fe_{19}$ and (c) $Co_{60}Fe_{20}B_{20}$, measuring the thinnest and the thickest films in each material series. The red dots are experimental data and the green curve is the fitted curve from Eq. 5.19.

Table 5.2: Fitting parameters for Co.

Sample	$c_\rho(\mu\Omega^{-1}\cdot\mathrm{cm}^{-1})$	$c_\sigma(\mu\Omega\cdot\mathrm{cm})$	α_0
3.5 nm (T)	~ 0	0.470	~ 0
30 nm (T)	~ 0	0.135	~ 0
t_{FM} (300 K)	5.97×10^{-5}	0.031	0.0061

Table 5.3: Fitting parameters for $Ni_{81}Fe_{19}$.

Sample	$c_\rho(\mu\Omega^{-1}\cdot\mathrm{cm}^{-1})$	$c_\sigma(\mu\Omega\cdot\mathrm{cm})$	α_0
3 nm (T)	15.0×10^{-5}	~ 0	~ 0
30 nm (T)	28.5×10^{-5}	36.9×10^{-5}	~ 0
t_{FM} (300 K)	5.97×10^{-5}	47.7×10^{-5}	0.0026

each material series. While the $Ni_{81}Fe_{19}$ and $Co_{60}Fe_{20}B_{20}$ samples show mostly a *resistivity*-like damping, consistent with the observations in the room temperature t_{FM} dependent measurements, the Co samples show a *conductivity*-like trend for both the thin and the thick films. If we plot these T-dependent data together with the t_{FM} series as in Fig. 5.12, striking discrepancy occurs for the 3.5 nm Co film. We attribute this to the strong SOC in the thin Co film as discussed in the $4\pi M_s^{eff}(T)$ and $K^{(n)}(T)$ study. Because of this strongly increased SOC with reduced T, the 'breathing' Fermi surface shows higher fluctuation amplitude and therefore more *intraband* electron-hole pairs are generated and annihilated, leading to a *conductivity*-like damping behavior. Meanwhile, the band gap between bands j and j' increases due to the increased SOC. The probability of generating *interband* electron-hole pairs is thus limited.

We summarize the fitting parameters c_σ, c_ρ and α_0 in Eq. 5.19 for the t_{FM} and T series of the three materials in Tables 5.2, 5.3 and 5.4 respectively. According to Table 5.4, the experimental results for $Co_{60}Fe_{20}B_{20}$ agree with the simple resistivity-like theoretical model well, with no artificially introduced α_0 and reasonable consistency among the fitting parameters obtained from the T and t_{FM} series. We also conclude that the SOC does not play a significant role in the Gilbert damping of the $Co_{60}Fe_{20}B_{20}$. The interpretation is

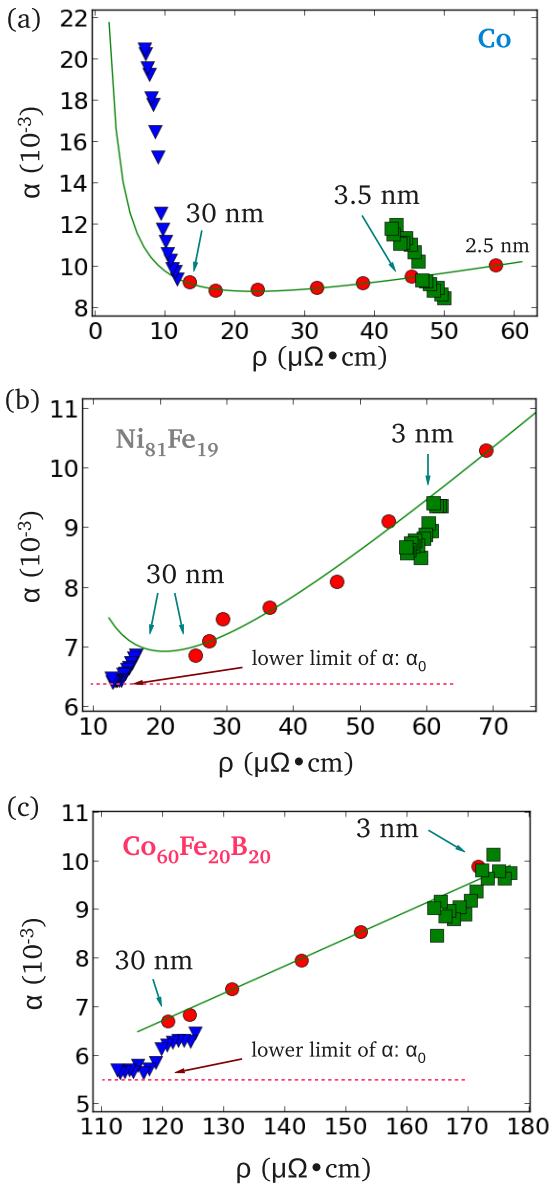

Figure 5.12: α as a function of ρ, combining the T and t_{FM} series. (a) Co; (b) $Ni_{81}Fe_{19}$; (c)$Co_{60}Fe_{20}B_{20}$. The green fitted curve is for the t_FM series only.

Table 5.4: Fitting parameters for $Co_{60}Fe_{20}B_{20}$.

Sample	$c_\rho(\mu\Omega^{-1}\cdot\mathrm{cm}^{-1})$	$c_\sigma(\mu\Omega\cdot\mathrm{cm})$	α_0
3 nm (T)	5.45×10^{-5}	~ 0	~ 0
30 nm (T)	5.03×10^{-5}	~ 0	~ 0
t_{FM} (300 K)	5.61×10^{-5}	~ 0	~ 0

more complicated in the cases of Co and $Ni_{81}Fe_{19}$, as we could see from Tables 5.2 and 5.3. First we notice a non-zero α_0 for the t_{FM} series, which does not exist in the theoretical model. Second, the fitting parameters do not agree well in the different series. We also observe from Fig. 5.11 that the fitted line does ot reflect the trends in the experimental data adequately. This might arise from the T and t_{FM} dependence of the coefficients c_1 and c_2 in Eq. 5.17, mostly due to the T dependence of anisotropy and SOC, which needs more careful experiments and analysis to interpretate quantitatively. Another aspect is the artifacts introduced by the experimental details, such as the elevated temperature during soldering which might have annealed the soft magnetic materials, and the finite size of the electrical contacts for the T-dependent measurements.

5.3 Summary and outlook

We have discussed in this chapter the electron-scattering mechanism of the direct Gilbert damping in itinerant ferromagnets, demonstrated our experimental techniques for measuring the resistivity and the damping paramter in thin film samples in the temperature range of 25 K - 300 K, and presented the data of the damping α as a function of resistivity ρ in three most representative modern thin-film metallic ferromagnetic materials, Co, $Ni_{81}Fe_{19}$ and $Co_{60}Fe_{20}B_{20}$, to verify the theoretical models. This is the first temperature-dependent study of Gilbert damping in these materials in thin-film form. Reasonable agreement between the model and the experimental results was found in $Co_{60}Fe_{20}B_{20}$, and we observed for the first time a clear cross-over from conductivity-like damping to resistivity-like damping in Co.

The interpretation of the discrepancies between the T series data and the t_{FM} series

data remains an open issue. It might be resolved through a more complete set of cryogenic measurements on the thickness series, in addition to the six samples at extremes of thickness. Ideally the measurements should include the t_{FM} series at each T point, or equivalently the T series at each t_{FM}. More insightful discussions could be carried out if we could plot the fitting parameters, extracted from the t_{FM} series at each T point, as a function of T, or vice versa. Connections could then be established between the surface anisotropy (either T-dependent or T-independent), the SOC and the damping, and more detailed calculations could be carried out to find the relationship between the fitting parameters c_ρ and c_σ and the coefficients in the model, c_1 and c_2, according to the intrinsic properties of the FM material.

Chapter 6

Nonlinear effect of LLG at small angle precession: high-efficiency GHz frequency doubling without power threshold in thin-film $Ni_{81}Fe_{19}$

With the discussions carried out the in the previous two chapters, we established the understanding of the linearized LLG equatation under in-plane ferromagnetic resonance (FMR) with linearly polarized, transverse driving field h_y^{rf}. We now proceed to the more complicated case based on in-plane FMR, adding to the system a longitudinal rf field component h_z^{rf}, where nonlinear effects could be observed in the small-angle limit. We demonstrate efficient second-harmonic generation at moderate input powers for thin film $Ni_{81}Fe_{19}$ under FMR. Powers of the generated second-harmonic are shown to be quadratic in input power, with an upconversion ratio three orders of magnitude higher than that demonstrated in ferrites [64], defined as $\Delta P^{2\omega}/\Delta P^{\omega} \sim 4 \times 10^{-5}/W \cdot P^{\omega}$, where ΔP is the change in the transmitted rf power and P is the input rf power. The second harmonic signal generated

exhibits a significantly lower linewidth than that predicted by low-power Gilbert damping, and is excited without threshold. Results are in good agreement with an analytic, approximate expansion of the Landau-Lifshitz-Gilbert (LLG) equation.

6.1 Introduction: nonlinearity in LLG equation

Nonlinear effects in magnetization dynamics, apart from being of fundamental interest [64–67], have provided important tools for microwave signal processing, especially in terms of frequency doubling and mixing [68, 69]. Extensive experimental work exists on ferrites [64, 67, 69], traditionally used in low-loss devices due to their insulating nature and narrow ferromagnetic resonance (FMR) linewidth. Metallic thin-film ferromagnets are of interest for use in these and related devices due to their high moments, integrability with CMOS processes, and potential for enhanced functionality from spin transport; though having higher damping than ferrites, low FMR linewidth has been demonstrated recently in metals through compensation by the spin Hall effect [70]. While some recent work has addressed nonlinear effects [71–73] and harmonic generation [74–76] in metallic ferromagnets and related devices [77–79], these studies have generally used very high power or rf fields, and have not distinguished between effects above and below the Suhl instability threshold. In this chapter, we demonstrate frequency doubling below threshold in a metallic system ($Ni_{81}Fe_{19}$) which is three orders of magnitude more efficient than that demonstrated previously in ferrite materials [64]. The results are in good quantitative agreement with an analytical expansion of the Landau-Lifshitz-Gilbert (LLG) equation.

6.2 Experiment: detecting FMR and second harmonic generation using spectrum analyzer

6.2.1 Experimental setup

For all measurements shown, we used a metallic ferromagnetic (FM) thin film structure, Ta(5 nm)/Cu(5 nm)/$Ni_{81}Fe_{19}$ (30 nm)/Cu(3 nm)/Al(3 nm). The film was deposited on an oxidized silicon substrate using magnetron sputtering at a base pressure of 2.0×10^{-7} Torr by S. Auffret at SPINTEC; it has no special features compared with those deposited in our UHV sputtering chamber, except its ready availability with photoresist already spun on, for another study. The bottom Ta(5 nm)/Cu(5 nm) layer is a seed layer to improve adhesion and homogeneity of the film and the top Cu(3 nm)/Al(3 nm) layer protects the $Ni_{81}Fe_{19}$ layer from oxidation. A diagram of the measurement configuration, adapted from a basic broadband FMR setup, is shown in Fig. 6.1. The microwave signal is conveyed to and from the sample through a coplanar waveguide (CPW) with a 400 μm wide center conductor and 50 Ω characteristic impedance, which gives an estimated rf field of 2.25 Oe rms with the input power of +30 dBm. We examined the second harmonic generation with fundamental frequencies at 6.1 GHz and 2.0 GHz. The cw signal from the rf source is first amplified by a solid state amplifier, then the signal power is tuned to the desirable level by an adjustable attenuator. Harmonics of the designated input frequency are attenuated by the bandpass filter to less than the noise floor of the spectrum analyzer (SA). The isolator limits back-reflection of the filtered signal from the sample into the rf source. From our analysis detailed in a later section of this chapter, we found the second harmonic magnitude to be proportional to the product of the longitudinal and transverse rf field strengths, and thus place the center conductor of CPW at 45° from H_B to maximize the $H_y^{rf}H_z^{rf}$ product. The rf signal finally reaches the SA for measurements of the power of both the fundamental frequency and its second harmonic.

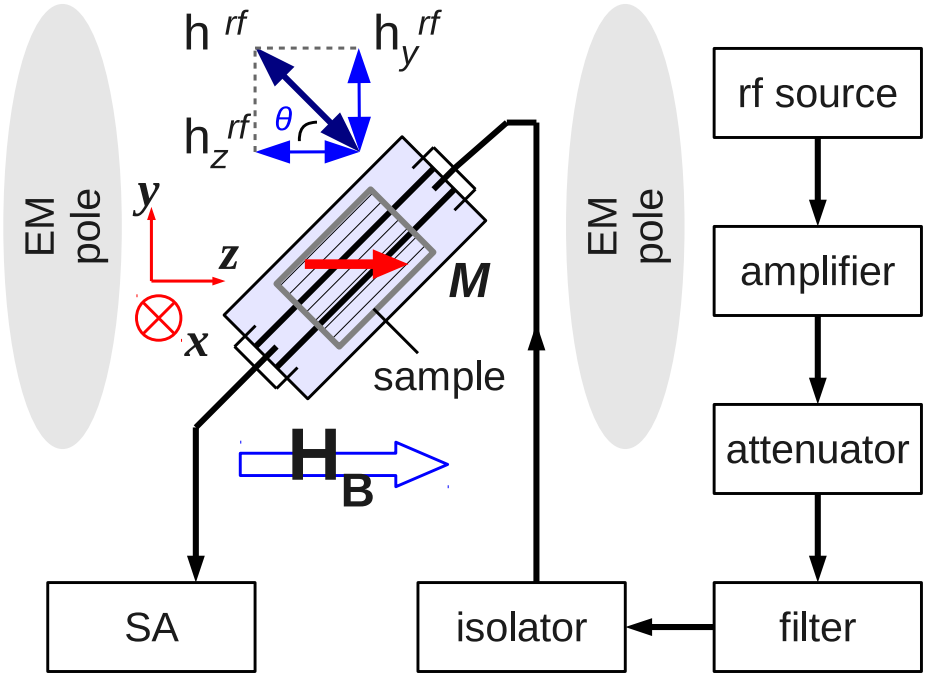

Figure 6.1: Experimental setup and the coordinate system, $\theta = 45°$. EM: electromagnet; SA: spectrum analyzer. Arrows indicate the transmission of rf signal.

6.2.2 Experimental data: power absoprtion at FMR and emission at the second harmonic

Fig. 6.2 (a) demonstrates representative field-swept FMR absorption and the second harmonic emission spectra measured by the SA as 6.1 GHz and 12.2 GHz peak intensities as a function of the bias field H_B. We vary the input rf power over a moderate range of +4 - +18 dBm, and fit the peaks with a Lorentzian function to extract the amplitude and the linewidth of the absorbed (ΔP^{ω}) and generated ($\Delta P^{2\omega}$) power. Noticeably, the second harmonic emission peaks have a much smaller linewidth, $\Delta H_{1/2} \sim 10$ Oe over the whole power range, than those of the FMR peaks, with $\Delta H_{1/2} \sim 21$ Oe. Though a linewidth of ~10 Oe at 12.2 GHz is one order of magnitude larger than the measured X-band linewidth (~ 1 Oe) in bulk single-crystal YIG [80], it is about 1/5 of the 12.2 GHz FMR linewidth (~ 60 Oe) in the 30 nm $Ni_{81}Fe_{19}$ film. Plots of the absorption and emission peak amplitudes as a function of the input 6.1 GHz power, shown in Fig. 6.2 (b), clearly indicate a linear

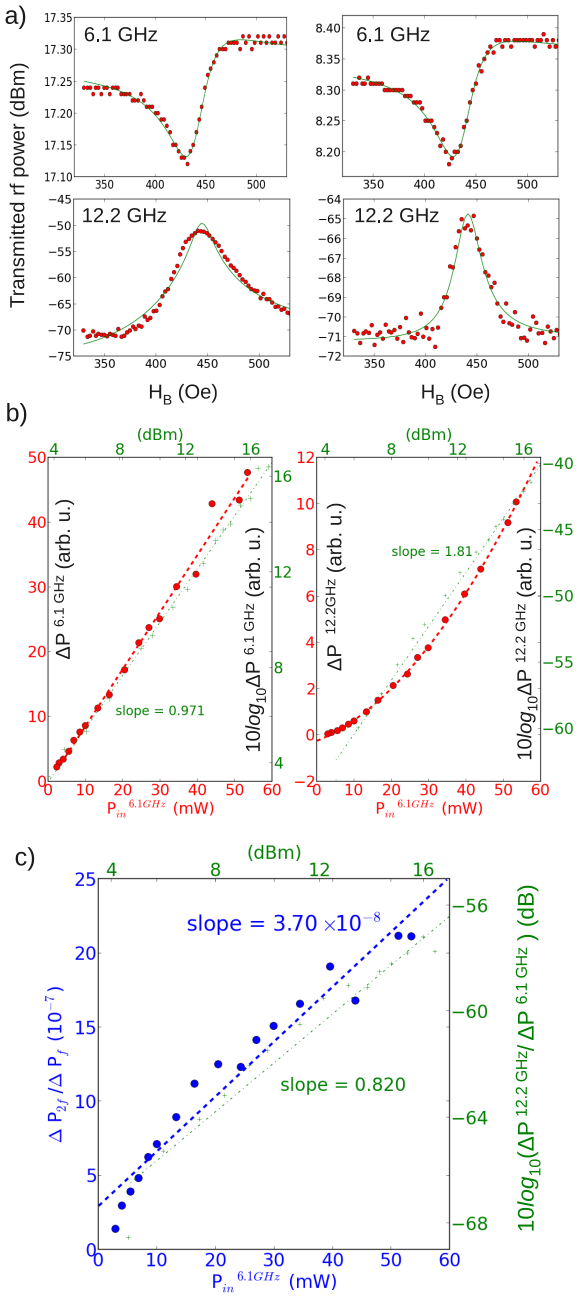

Figure 6.2: Second harmonic generation with $\omega/2\pi = 6.1$ GHz. (a) *left panel*: 6.1 GHz input power +17.3 dBm; *right panel*: 6.1 GHz input power +8.35 dBm. (b) amplitudes of the ω (FMR) and generated 2ω peaks as a function of input power P^{ω}; right and top axes represent the data set in log-log plot (green), extracting the power index; (c) ratio of the peak amplitudes of FMR and second harmonic generation as a function of the input 6.1 GHz power; green: log scale.

dependence of the FMR absorption and a quadratic dependence of the second harmonic generation on the input rf power. Taking the ratio of the radiated second harmonic power to the absorbed power, we have a conversion rate of 3.7×10^{-5}/W, as shown in Fig. 6.2(c).

6.3 Analysis: first-order expansion of LLG with longitudinal rf field

6.3.1 The equation of motion for perturbation terms

Since the phenomenon summarized in Fig. 6.2 is clearly not a threshold effect, we look into the second-harmonic analysis of the LLG equation with small rf fields, and found that the second harmonic generation is determined by the longitudinal rf field in addition to the transverse rf field. The method for the expansion of LLG equation with small rf fields is readily described in Gurevich and Melkov's text for circular precession relevant in the past for low-M_s ferrites [81]. For metallic thin films, we treat the elliptical case as follows. As illustrated in Fig. 6.1, the thin film is magnetized in the yz plane along $\widehat{\mathbf{z}}$ by the bias field H_B, with film-normal direction along $\widehat{\mathbf{x}}$. The CPW exerts both a longitudinal rf field h_z^{rf} and a transverse rf field h_y^{rf} of equal strength. First consider only the transverse field h_y^{rf}. In this well established case described in Chap. 4, the LLG equation $\dot{\mathbf{m}} = -\gamma\mathbf{m}\times\mathbf{H}_{eff} + \alpha\mathbf{m}\times\dot{\mathbf{m}}$ is linearized and takes the form

$$\begin{bmatrix} \dot{\widetilde{m_x}} \\ \dot{\widetilde{m_y}} \end{bmatrix} = \begin{bmatrix} -\alpha(\omega_H+\omega_M) & -\omega_H \\ \omega_H+\omega_M & -\alpha\omega_H \end{bmatrix} \begin{bmatrix} \widetilde{m_x} \\ \widetilde{m_y} \end{bmatrix} + \begin{bmatrix} \widetilde{\gamma h_y^{rf}} \\ 0 \end{bmatrix} \tag{6.1}$$

, where γ is the gyromagnetic ratio, α is the Gilbert damping parameter, $\omega_M \equiv \gamma 4\pi M_s$, and $\omega_H \equiv \gamma H_z$. Introducing first order perturbation to $m_{x,y}$ under additional longitudinal h_z^{rf} and neglecting the second order terms, we have

$$\begin{bmatrix} \dot{\widetilde{m_x}} + \dot{\widetilde{\Delta m_x}} \\ \dot{\widetilde{m_y}} + \dot{\widetilde{\Delta m_y}} \end{bmatrix} = \begin{bmatrix} -\alpha(\omega_H+\omega_M) & -\omega_H \\ \omega_H+\omega_M & -\alpha\omega_H \end{bmatrix} \begin{bmatrix} \widetilde{m_x} + \widetilde{\Delta m_x} \\ \widetilde{m_y} + \widetilde{\Delta m_y} \end{bmatrix} + \begin{bmatrix} \widetilde{\gamma h_z^{rf}}\widetilde{m_y} \\ -\widetilde{\gamma h_z^{rf}}\widetilde{m_x} \end{bmatrix} + \begin{bmatrix} \widetilde{\gamma h_y^{rf}} \\ 0 \end{bmatrix} \tag{6.2}$$

Subtracting Eq. 6.1 from Eq. 6.2 and taking

$$\widetilde{h^{rf}}_{y,z} = H^{rf}_{y,z} e^{-i\omega t},$$

$$\widetilde{m}_{x,y} = (H^{rf}_{y}/M_s) e^{-i\omega t} \widetilde{\chi}_{\perp,\parallel}(\omega) \tag{6.3}$$

the equation for the perturbation terms is

$$\begin{bmatrix} \dot{\widetilde{\Delta m_x}} \\ \dot{\widetilde{\Delta m_y}} \end{bmatrix} = \begin{bmatrix} -\alpha(\omega_H + \omega_M) & -\omega_H \\ \omega_H + \omega_M & -\alpha\omega_H \end{bmatrix} \begin{bmatrix} \widetilde{\Delta m_x} \\ \widetilde{\Delta m_y} \end{bmatrix} + H^{rf}_z \frac{H^{rf}_y}{M_s} e^{-i2\omega t} \begin{bmatrix} \gamma\widetilde{\chi_\parallel}(\omega) \\ -\gamma\widetilde{\chi_\perp}(\omega) \end{bmatrix} \tag{6.4}$$

Since $\chi_\perp$ is one order of magnitude smaller than $\chi_\parallel$, we neglect the term $-\gamma\widetilde{\chi_\perp}(\omega)$. In complete analogy to Eq. 6.1, the driving term could be viewed as an effective transverse field of

$$H^{rf}_z (H^{rf}_y/M_s)\widetilde{\chi_\parallel}(\omega) e^{-i2\omega t}, \tag{6.5}$$

and the solutions to Eq. 6.4 would be

$$\begin{aligned} \widetilde{\Delta m_x} &= (H^{rf}_z H^{rf}_y / M_s^2)\widetilde{\chi_\parallel}(\omega)\widetilde{\chi_\perp}(2\omega) e^{-i2\omega t}, \\ \widetilde{\Delta m_y} &= (H^{rf}_z H^{rf}_y / M_s^2)\widetilde{\chi_\parallel}(\omega)\widetilde{\chi_\parallel}(2\omega) e^{-i2\omega t}. \end{aligned} \tag{6.6}$$

We can compare the power at frequency f and $2f$ now that we have the expressions for both the fundamental (Eq.6.3) and second harmonic components (Eq.6.6) of the precessing **M**. The time-averaged power per unit volume could be calculated as

$$\langle P \rangle = [\int_0^{\frac{2\pi}{\omega}} P(t)dt]/(2\pi/\omega),$$

where

$$P(t) = -\partial U/\partial t = 2\mathbf{M}\partial\mathbf{H}/\partial t.$$

as mentioned in the last section of Chap. 4. Only the transverse components of **M** and **H** contribute to P(t). Using the expression for $\langle P \rangle$, **M** and **H**, we have

$$P^\omega = \omega H^2_{y,rf} \chi(\omega)''_\parallel \tag{6.7}$$

which is derived in the last section of Chap. 4. Next we look into the power in the second harmonic generation case in detail.

6.3.2 Power of the second harmonic generation

In this section we are going to derive the power of the second harmonic generation, which is done the first time for the highly elliptical precession relevant for a metallic FM film. We start with the expression of the transverse magnetization

$$\tilde{M}_T(t) = H_y e^{i\omega t}\tilde{\chi}(\omega)_{\parallel} h_z e^{i\omega t}\tilde{\chi}(2\omega)_{\parallel}$$

$$= H_y h_z e^{i2\omega t}[\chi(\omega)'_{\parallel} + i\chi(\omega)''_{\parallel}][\chi(2\omega)'_{\parallel} + i\chi(2\omega)''_{\parallel}]$$

$$= H_y h_z e^{i2\omega t}\{[\chi(\omega)'_{\parallel}\chi(2\omega)'_{\parallel} - \chi(\omega)''_{\parallel}\chi(2\omega)''_{\parallel}] + i[\chi(\omega)''_{\parallel}\chi(2\omega)'_{\parallel} + \chi(\omega)'_{\parallel}\chi(2\omega)''_{\parallel}]\}$$

$$= H_y h_z[\cos(2\omega t)+i\sin(2\omega t)]\{[\chi(\omega)'_{\parallel}\chi(2\omega)'_{\parallel}-\chi(\omega)''_{\parallel}\chi(2\omega)''_{\parallel}]+i[\chi(\omega)''_{\parallel}\chi(2\omega)'_{\parallel}+\chi(\omega)'_{\parallel}\chi(2\omega)''_{\parallel}]\}$$

Take the real part,

$$M_T(t) = H_y h_z[\chi(\omega)'_{\parallel}\chi(2\omega)'_{\parallel} - \chi(\omega)''_{\parallel}\chi(2\omega)''_{\parallel}]\cos(2\omega t)$$

$$-H_y h_z[\chi(\omega)''_{\parallel}\chi(2\omega)'_{\parallel} + \chi(\omega)'_{\parallel}\chi(2\omega)''_{\parallel}]\sin(2\omega t) \tag{6.8}$$

The driving force is not H^{ω}_{rf} (if we calculate the time integral of $2M_T\frac{\partial H^{\omega}_T}{\partial t}$ it is 0). According to Eq.6.5 the effective driving field is

$$\tilde{H}_T(t) = H_y h_z \tilde{\chi}(\omega)_{\parallel} e^{i2\omega t}$$

$$= H_y h_z[\chi(\omega)'_{\parallel} + i\chi(\omega)''_{\parallel}][\cos(2\omega t) + i\sin(2\omega t)]$$

where $h_z = H_z/M_s$. Take the real part of the complex expression,

$$H_T(t) = H_y h_z[\chi(\omega)'_{\parallel}\cos(2\omega t) - \chi(\omega)''_{\parallel}\sin(2\omega t)] \tag{6.9}$$

$$\frac{\partial H_T(t)}{\partial t} = H_y h_z[-2\omega\chi(\omega)'_{\parallel}\sin(2\omega t) - 2\omega\chi(\omega)''_{\parallel}\cos(2\omega t)]$$

$$= -2\omega H_y h_z[\chi(\omega)'_{\parallel}\sin(2\omega t) + \chi(\omega)''_{\parallel}\cos(2\omega t)] \tag{6.10}$$

Now the instantaneous power is $2M_T\frac{\partial H_T}{\partial t}$, putting eq.(9) and (11) together, and remember the time integral of $\sin(2\omega t)\cos(2\omega t)$ goes to 0, and the averaged time integral of $\sin^2(2\omega t)$ and $\cos^2(2\omega t)$ is $\frac{1}{2}$.

$$P(t)' = -4\omega H_y^2 h_z^2[A\cos^2(2\omega t) - B\sin^2(2\omega t)],$$

where P(t)' is the part of P(t) which yields non-zero time integral,

$$A = \chi(\omega)'_{\parallel}\chi(\omega)''_{\parallel}\chi(2\omega)'_{\parallel} - [\chi(\omega)''_{\parallel}]^2\chi(2\omega)''_{\parallel}$$

$$B = \chi(\omega)'_{\parallel}\chi(\omega)''_{\parallel}\chi(2\omega)'_{\parallel} + [\chi(\omega)'_{\parallel}]^2\chi(2\omega)''_{\parallel}$$

The first term in A and B cancel out, because of the equal averaged time integral of $\sin^2(2\omega t)$ and $\cos^2(2\omega t)$.

Finally,

$$\begin{aligned}\langle P\rangle &= -4\omega H_y^2 h_z^2 \frac{1}{2}\{-[\chi(\omega)''_{\parallel}]^2\chi(2\omega)''_{\parallel} - [\chi(\omega)'_{\parallel}]^2\chi(2\omega)''_{\parallel}\} \\ &= 2\omega H_y^2 h_z^2\{[\chi(\omega)''_{\parallel}]^2 + [\chi(\omega)'_{\parallel}]^2\}\chi(2\omega)''_{\parallel} \\ &= 2\omega H_y^2 h_z^2|\tilde{\chi}(\omega)_{\parallel}|^2\chi(2\omega)''_{\parallel}, \end{aligned} \tag{6.11}$$

or

$$P^{2\omega} = 2\omega H_{z,rf}^2 (H_y^{rf}/M_s)^2|\tilde{\chi}(\omega)_{\parallel}|^2\chi(2\omega)''_{\parallel} \tag{6.12}$$

Since $H_{y,rf}^2$ and $H_{z,rf}^2$ are proportional to the rf power, the P^{ω} and $P^{2\omega}$ terms should be linearly and quadratically dependent on the input rf power, respectively, which explains the data presented in Fig. 6.2 (b).

Examining Eq. 6.12, we notice that there should be two peaks in the field-swept $2f$ emission spectrum: the first coincides with the FMR but with a narrower linewidth due to the term $|\tilde{\chi}(\omega)_{\parallel}|^2$, and the second positioned at the H_B for the FMR with a $2f$ input signal due to the term $\chi(2\omega)''_{\parallel}$. The second peak should have a much smaller amplitude. Due to the field limit of our electromagnet, we could not reach the bias field required for FMR at 12.2 GHz under this particular configuration and continued to verify Eq. 6.12 at a lower frequency of 2.0 GHz. Fig. 6.3 demonstrates the typical line shape of the 4 GHz spectrum, in which the input 2 GHz power being +18.9 dBm. A second peak at the H_B for 4 GHz FMR is clearly visible with a much smaller amplitude and larger linewidth than the first peak, qualitatively consistent with Eq. 6.12. A theoretical line (dashed green) from Eq. 6.12 with fixed damping parameter $\alpha = 0.007$ is drawn to compare with the experimental data.

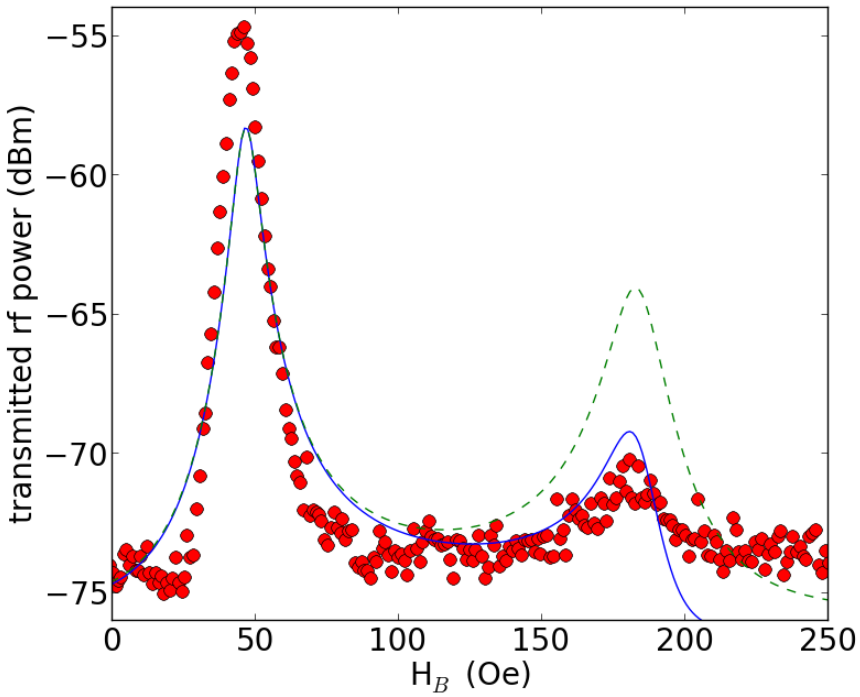

Figure 6.3: 4 GHz generation with input signal at 2 GHz, +18.9 dBm. A second peak at the bias field for 4 GHz FMR is clearly present; red dots: experimental data; dashed green: theoretical; blue: adjusted theoretical with input rf impurity.

The observed second peak at the $2f$ resonance H_B shows a much lower amplitude than expected. We contribute this difference to the possible $2f$ component in the rf source which causes the $2f$ FMR absorption. The blue line shows the adjusted theoretical line with consideration of this input signal impurity.

6.3.3 Power ratio between FMR and the second harmonic

From the P^{ω} (Eq. 6.7) and $P^{2\omega}$ (Eq. 6.12) expressions, we conclude that under H_B for FMR at frequency $f = \omega/(2\pi)$, we should see a power ratio

$$P^{2\omega}/P^{\omega} = 2(H_z^{rf}/M_s)^2 \chi(\omega)''_{\parallel} \chi(2\omega)''_{\parallel} \tag{6.13}$$

With $M_s = 844$ Oe, $\alpha = 0.007$ as measured by FMR for our $Ni_{81}Fe_{19}$ 30 nm sample and 2.25 Oe rf field amplitude at input power of 1 W for the CPW, we have a calculated $2f/f$ power ratio of 1.72×10^{-5}/W, which is in reasonable agreement with the experimental data 3.70×10^{-5}/W as shown in Fig. 6.2(c). To compare this result with the ferrite experiment in Ref. [64], we further add the factor representing the ratio of FMR absorption to the input rf power, which is 3.9×10^{-2} in our setup. This leads to an experimental upconversion ratio of 1.44×10^{-6}/W in Ref. [64]'s definition ($\Delta P^{2\omega}/P_{in}^{\omega\,2}$), compared with 7.1×10^{-10}/W observed in $Mg_{70}Mn_8Fe_{22}O$ (Ferramic R-1 ferrite). We carried out an identical experiment and analysis at 2.0 GHz input, and observed an upconversion efficiency of 0.39×10^{-3}/W for the 4.0 GHz signal generation, again in reasonable agreement with the theoretical prediction 1.17×10^{-3}/W and shows even higher efficiency. Since χ decreases with increasing frequency, this enhanced upconversion efficiency at low input frequencies is expected.

6.4 Summary

We have demonstrated a highly efficient frequency doubling effect in thin-film $Ni_{81}Fe_{19}$ for input powers well below the Suhl instability threshold [66]. An analysis of the intrinsically nonlinear LLG equation interprets the observed phenomena quantitatively. The results explore opportunities in the field of rf signal manipulation with CMOS compatible thin film structures.

Chapter 7

X-ray magnetic circular dichroism and pump-probe technique

The *time-resolved* detection of *element-specific* magnetization in a thin-film sample under ferromagnetic resonance (FMR) is a powerful tool for understanding the relationship between the rf excitation and the magnetization dynamics. Soft x-rays (0.1 nm $\lesssim \lambda \lesssim$ 10 nm, or 10 keV $\gtrsim \hbar\nu \gtrsim$ 100 eV) can be absorbed with element-specificity by $L_{2,3}$ edges of $3d$ transition metals. Because these absorption edges are well-separated ($\sim$ 70 eV) compared with their spectral width ($\sim$ 2 eV), x-ray absorption spectroscopy (XAS) can be used to quantify composition in alloys. In magnetically ordered solids, the XAS can exhibit a circular dichroism (x-ray photon helicity dependence) which yields different absorption rates for *left*-hand circularly polarized light and *right*-hand circularly polarized light. This leads to element-specific *magnetic* contrast with spatial resolution up to less than 15 nm, depending on the x-ray optics. The stroboscopic technique could be applied to the ferromagnetic (FM) system for time-resolved recording of the x-ray magnetic contrast. In this chapter, we will look into x-ray mangetic circular dichroism (XMCD), the origin of magnetic contrast, the principles of the pump-probe technique, and the sample preparation for x-ray spectroscopy and microscopy.

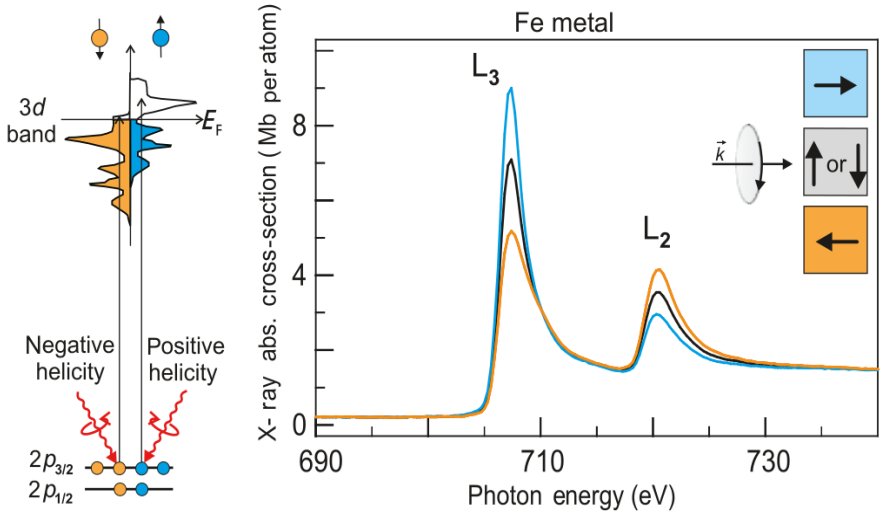

Figure 7.1: *from Ref. [61, chap.9.6].* The XMCD effect illustrated for the L-edge absorption in Fe metal.

7.1 X-ray mangeitc circular dichroism (XMCD)

Fig. 7.1 illustrates the XMCD effect in Fe at the L-edge. The experimental data in the right panel are from Ref. [82]. **k** is the wavevector of the circularly polarized x-ray. For *right*-hand circularly polarized (RCP) x-rays, the photon has angular momentum $\boldsymbol{\sigma}$ pointing to the right, parallel to the beam propagation direction **k** in the figure; for *left*-hand circular polarization (LCP), the photon angular momentum points to the left, antiparallel with **k**. In the blue, gray and yellow squares, the arrow indicates the orientation of the magnetization in the sample. From the blue and the yellow x-ray absorption curves, we observe that for the x-ray photons with angular momentum pointing to the right, the absorption rate at the L_3 edge is the highest if the magnetization also points to the right. In the case of antiparallel alignment of the photon angular momentum and the magnetic moment, the absorption rate is the lowest. We could explain this phenomenon as illustrated in the left panel of Fig. 7.1. For absorption at the L_3 edge, the electron in the $2p_{3/2}$ shell absorbs the x-ray photon and is excited, into the empty d-states above the Fermi level. The L_3 ($2p_{3/2}$)

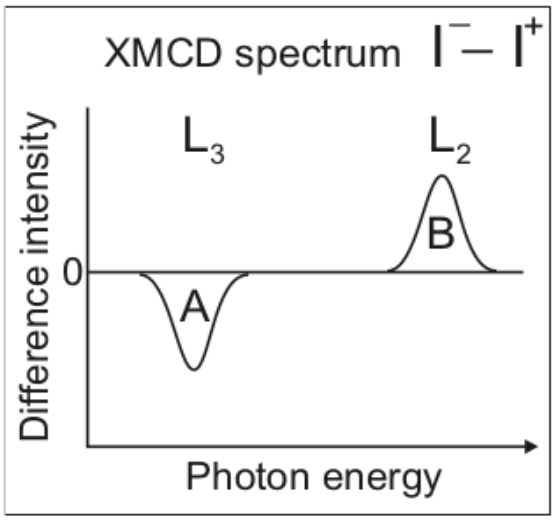

Figure 7.2: *from Ref. [61, chap.9.6]* Illustration of the differential XMCD spectrum; $I^-(I^-)$: absorbed x-ray intensity under antiparallel (parallel) alignment of the magnetization and the photon helicity

absorption is most efficient if the angular momentum of the photon is parallel with the spin of the electron. The excitation rate is also determined by the density of the available electron states near the Fermi level. For the minority spin-up (blue) electrons in the figure, the density of states near the Fermi level is larger than that of the majority spin-down (yellow) electrons. Therefore, the excitation rate for the spin-up electrons is higher than for the spin-down electrons at L_3 edge, enhancing the absorption for $\sigma = +1$ (RCP) aligned with $\mathbf{M}$ at L_3. If magnetization $\mathbf{M}$ reverses, absorption for $\sigma = +1$ (RCP) is reduced at L_3. This is the origin of the magnetic circular dichroism (MCD) effect. The effect is reversed at L_2 because absorption here is most efficient for helicity $\boldsymbol{\sigma}$ antiparallel with the spin. The MCD effect explains the difference in the x-ray absorption rates represented by the blue and the yellow curves. We express the magnetic contrast, the x-ray absorption rate A as

$$A \propto \mathbf{M} \cdot \boldsymbol{\sigma}$$

where $\mathbf{M}$ is the magnetization and $\boldsymbol{\sigma}$ is the helicity of the circurlarly polarized x-ray.

Taking the difference between the transmitted x-ray intensities for the cases where the

magnetization and the x-ray helicity are antiparallel($\uparrow\downarrow$) and parallel ($\uparrow\uparrow$),

$$\Delta I = I^{\uparrow\downarrow} - I^{\uparrow\uparrow}$$

we have the XMCD spectrum as shown in Fig. 7.2.

7.2 The pump-probe technique

At synchrotron facitilies, operating modes often exist in which orbiting electrons fill the storage ring at regular intervals, grouped together into evenly spaced "bunches". If the bunches are highly packed in space, the light they generate when traversing an insertion device (magnet array) has a short pulse duration. These light flashes, $\sim$ 30 ps RMS at modern synchrotrons, are used as the stroboscopic "probe" in a *pump-probe* experiment. Their closest spacing in time is given by the inverse bunch-clock frequency, dependent on the fill pattern. This is 88 MHz for special mode four (SOM-4) at the Advanced Photon Source (APS) and 500 MHz for normal operation at the Canadian Light Source (CLS).

The bunch-clock signal can be used as a seed for a phase-locked rf excitation to the FM system for FMR. Since the bunch clock and the x-ray bunches are phase-locked, by introducing a picosecond-resolution delay line in the rf circuit, we can vary the delay between rf pump and x-ray probe. Thus we place the x-ray pulse at a fixed time point within the rf excitation period. At the instant when the x-ray pulse illuminates the sample with the magnetization precessing, the magnetic contrast at that specific time point is recorded.

Fig. 7.3 presents the typical rf excitation and timing electronics of the *pump-probe* time-resolved (TR) XMCD technique [59]. We generate harmonics from the delayed x-ray bunch-clock signal, and amplify them to form the *pump* which excites the FMR in the sample. The phase-locked x-ray is the *probe*. For the work presented here, the x-ray bunches are given by the special operating mode-4 (SOM-4) at the Advanced Photon Source (APS) in Argonne, IL, which repeats at the frequency of 88 MHz. A delay line with minimum resolution of 2 ps introduces the delay between the pump and the probe, which defines the time point in the precession period at which we record the magnetization. The RF switch is

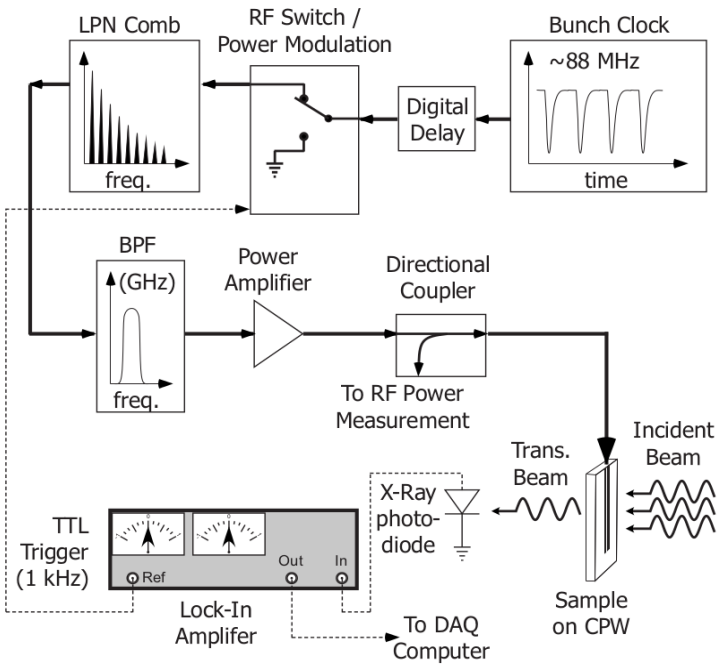

Figure 7.3: *from Ref. [59]*Rf excitation and timing electronics for the pump-probe technique in the special operating mode-4(SOM-4) at the Advanced Photon Source (APS). The generation of the phase-locked rf excitation follows the heavy solid lines while the detection of the x-ray signal proceeds along the light dashed lines.

controlled by the TTL output of the lock-in amplifier (LIA) which switches the rf power on and off at the reference frequency of the LIA, typically 1 kHz. The $f_0 = 88$ MHz bunch clock goes through a low phase noise (LPN) comb generator and its harmonics ($f_n = nf_0$) are generated, with intensities extending into high harmonics (n = 20 - 40). A band pass filter (BPF) selects the designated frequency $f_N = Nf_0$ from the harmonics of 88 MHz. After amplification, the rf signal at frequency f_N is sent to the sample via an SMA end launcher and a coplanar waveguide (CPW). For comparison with conventional FMR measurements, the rf signal is reflected back from the sample/CPW assembly using a directional coupler, synchronously with the rf power modulation at the LIA. For the x-ray measurements, the x-ray photons transmit through the sample on the CPW, which has a small hole drilled into the center conductor, under FMR and the intensity of the transmitted x-ray is recorded by a photo-diode, and then the signal from the photo-diode is sent to the LIA to improve the signal-noise ratio.

Fig. 7.4 demonstrates our sample mount assembly for the pump-probe XMCD experiments. There are two electromagnets on the assembly, one vertical coils pair to apply the bias field H_B for the FMR, and one transverse electromagnet to switch the magnetization in the horizontal direction for detecting static XMCD signals. The inset at the upper right corner shows the custom designed CPW for our x-ray spectroscopy and microscopy experiments. The hole (~ 125 μm diameter) in the center conductor is for the transmission of the x-ray, and is small enough not to disturb the overall distribution of the h^{rf} from the CPW. Details about the design could be found in Ref. [59].

7.3 Sample preparation

7.3.1 The substrate

Since the x-ray magnetic contrast requires the transmission of the soft x-ray through the magnetic thin film, we have to fabricate the sample on a substrate which is transparent to the x-ray with photon energies in the range of several hundred eV. The most commonly

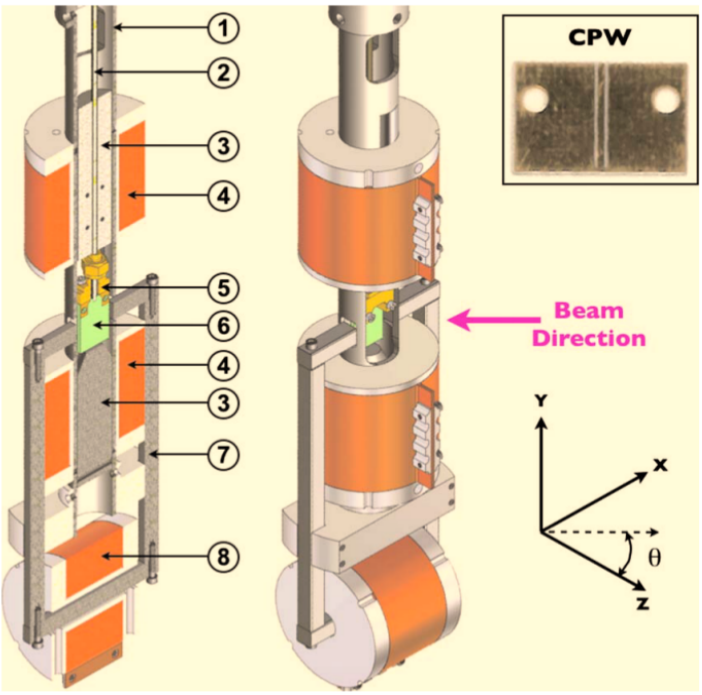

Figure 7.4: *from Ref. [59]* View of vector magnet and sample environment. *Right* panel: perspective with coordinate axes and indicating beam direction. *Left* panel: cross section through the sample plane: 1. support tube; 2. high frequency coaxial cable with SMA termination; 3. top and bottom vertical pole pieces; 4. top and bottom electromagnet coils; 5. end launcher; 6. sample; 7. yoke for horizontal magnetic field; and 8. electromagnet coil for horizontal field.

used substrates for this purpose are the Si_3N_4 membranes, commercially available with various Si_3N_4 thicknesses ($\sim$ 50 - 200 nm) and membrane window sizes (several hundred μm square). Although a thinner and wider membrane window can enhance the incident x-ray flux on the FM layer for imperfect alignment at larger x-ray spot sizes, it is much more fragile. Nominal x-ray spot sizes at beamline 4-ID-C at APS, after the refocusing mirror before the end chamber, are $\sim$ 100 μm.

For extended thin films intended for time-resolved FMR-XMCD measurements, commercial Si_3N_4 grids do not impose extra difficulty for sample preparation since only one step of magnetron sputtering is required. However, if the sample is intended for scanning transmission x-ray microscopy (STXM), with nanoscale elements on the membrane, it is advisable to fabricate the Si_3N_4 grids from whole Si_3N_4/Si/Si_3N_4 wafers. The commercially available Si_3N_4 grids have a small frame size, typically 5 mm $\times$ 5 mm. A smaller substrate area introduces a severe edge-bead problem during the spin-coating of photoresist (for photolithography) or PMMA (for ebeam lithography). Also, the narrow frame is difficult to handle during the multistep nanofabrication process, which requires constant transferring of the sample from one environment to another. Maintaining sample yield is much more difficult with a relatively large Si_3N_4 window in the center.

For the STXM experiments, to fabricate the Si_3N_4 membrane with arbitrary frame and window sizes, we start with a low-stress Si_3N_4/Si/Si_3N_4 wafer which is polished on both sides. On one side of the wafer, we define an area where the Si_3N_4 membrane window would appear, by either photolithography and subsequently plasma etching the Si_3N_4 layer, or simply scratching away the Si_3N_4 coating with a scriber. Next we prepare a warm ($\sim$ 65-70°C) solution of KOH and soak the wafer in the solution. Without the protection of the Si_3N_4 layer, in the area that we defined in the previous step, the Si layer would be attacked by the KOH and etched away. The etching of the Si would occur both vertically and horizontally; after the vertical etching stops at the Si_3N_4 layer on the other side of the wafer, the horizontal etching still progresses. It is necessary to pay attention to the soaking time of the wafer in the KOH solution to control the ultimate size of the Si_3N_4 membrane

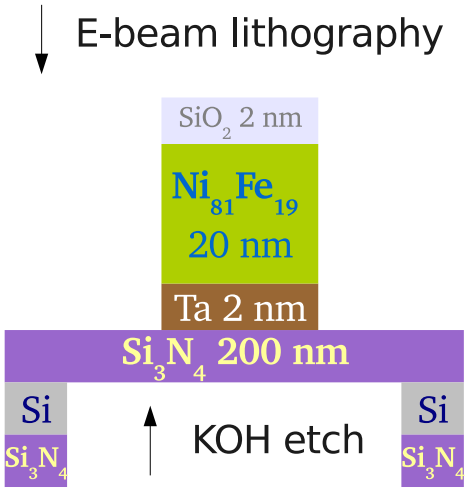

Figure 7.5: E-beam sample on Si_3N_4 membrane. The Si_3N_4 membrane window is fabricated by etching away the Si layer by KOH from a Si_3N_4/Si/Si_3N_4 wafer; the pattern is defined by e-beam lithography; the film is deposited by UHV sputtering; the elements emerge after the liftoff.

window. A relatively large frame with small membrane window is often desirable for a robust substrate which would survive the nanofabrication process with regular handling of the sample.

7.3.2 The FM thin film

The preparation of the FM thin film samples is identical to samples on a regular Si substrate, *i.e.* UHV magnetron sputtering for extended films, photolithography-sputtering-liftoff for thin film elements with the lateral dimensions in the μm regime, and e-beam lithography-sputtering-liftoff for elements in the nm regime. An example is given in Fig. 7.5.

Chapter 8

Detection of microwave phase variation in nanometer-scale magnetic heterostructures

In this section, we present time-resolved (TR) x-ray magnetic circular dichroism (XMCD) measurements of extened films which reveal a surprising gradient of the rf phase through a ferromagnetic (FM) heterostructure. The internal phase profile of electromagnetic (EM) radiation determines many functional properties of metal, oxide, or semiconductor heterostructures. In magnetic heterostructures, emerging spin electronic phenomena depend strongly upon the phase profile of the magnetic field $\tilde{H}$ at gigahertz frequencies. In this chapter, we will demonstrate nanometer-scale, layer-resolved detection of EM phase through the rf magnetic field $\tilde{H}_{\rm rf}$ in magnetic heterostructures. Time-resolved x-ray magnetic circular dichroism (XMCD) reveals the local phase of $\tilde{H}_{\rm rf}$ acting on individual magnetizations $\tilde{M}_i$ through the susceptibility as $\tilde{M} = \tilde{\chi}\tilde{H}_{\rm rf}$. An unexpectedly large phase variation, $\sim 40°$, is detected across spin-valve trilayers driven at 3 GHz. The results have implications for the identification of novel effects in spintronics and suggest general possibilities for EM phase profile measurement in heterostructures.

8.1 Introduction

Many functional properties of heterostructures require a known phase relationship between electromagnetic fields throughout the structure. Lasing [83–85], superconducting microwave properties [86, 87], negative refraction [88, 89], and stimulated phonon emission ("sasing") [90, 91] all require some degree of coherence in the EM phases across layers. Phase-sensitive electric fields have been measured for short light pulses in ionized gases [92]; interferometric (wave mixing) techniques have been used to resolve the complex polarization $\tilde{P}$ of near band-edge absorption in single semiconductor quantum wells or thick films [93]. Nevertheless, these techniques have not been and perhaps cannot easily be applied to localize the phase of EM radiation in heterogeneous media. Layer- and interface-specific optical measurements, such as optical second harmonic generation [94] and photoluminescence [95], have been limited to measurements of intensity ($\propto |E|^2$), losing information on the phase.

Just as complex polarization $\tilde{P}$ can be used to investigate the complex electric field $\tilde{E}$ through dielectric susceptibility $\tilde{\chi}_{\rm e}$, magnetization $\tilde{M}$ can be used as a probe of complex magnetic fields $\tilde{H}$ through the magnetic susceptibility $\tilde{\chi}_{\rm M}$. Measurement of the complex rf magnetic field profile $\tilde{H}_{\rm rf}(z)$ is essential for interpretation of GHz phenomena in ferromagnetic heterostructures [96–99]. Asymmetric ferromagnetic resonance (FMR) lineshapes, which mix real and imaginary susceptibilities as $\tilde{\chi} = \chi^{'} + i\chi^{"}$, have been interpreted in terms of imaginary effective field terms in the Landau-Lifshitz Gilbert (LLG) equation, attributed to novel spin transport mechanisms in heterostructures [97–99]. These interpretations typically rely on the assumption that there is no variation in the phase of $\tilde{H}_{\rm rf}$ reaching different F layers in a heterostructure. The use of "ultrathin" ferromagnetic (F or FM) and normal metal (N) films, much thinner than the metal skin depths as $t_{\rm F,N} \ll \delta$, is widely believed to make propagation effects negligible, creating a constant, real-valued magnetic field profile $\tilde{H}_{\rm rf}(z) = H_0$. Recent analysis has called this assumption into question [100].

In this chapter, we resolve the rf signal phase to 15 nm layers in a $F_1/N/F_2$ heterostructure, demonstrating phase resolution of electromagnetic radiation inside a layered system. Time-resolved x-ray magnetic circular dichroism (TR-XMCD) [59, 101] provides

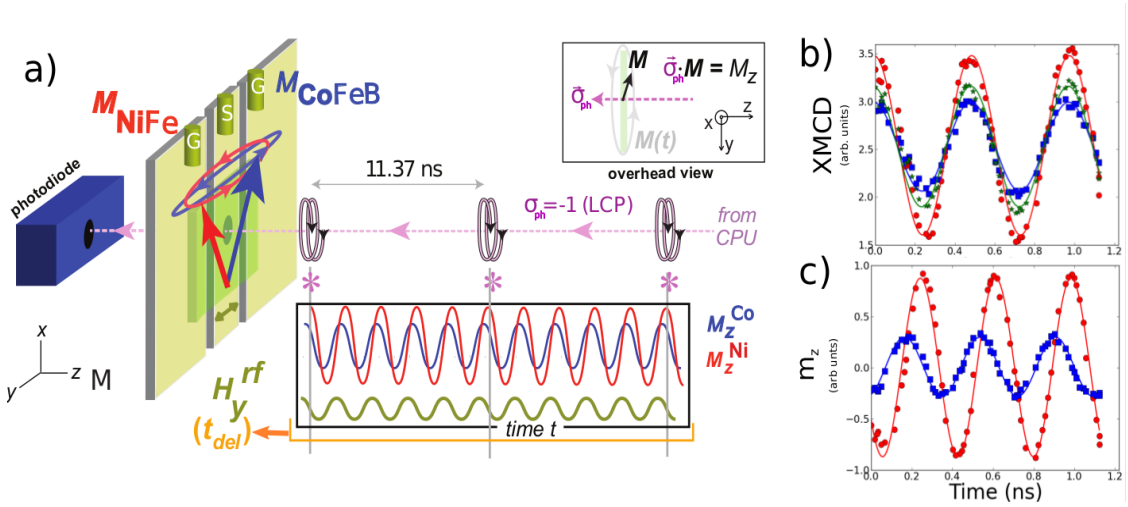

Figure 8.1: **Experimental method:** (a) Illustration of the time-resolved x-ray magnetic circular dichroism (TR-XMCD) technique. Stroboscopic x-rays, flashing at 40 ps, capture the precessional dynamics of individual magnetic layers in a heterostructure, through the Ni and Co circular dichroism signals at 854 and 779 eV, respectively, under continuous excitation at $\sim$ 3 GHz. Variable delay time for rf excitation maps the temporal dependence ($t = -t_{\rm del}$). (b) Dynamics in a $[Ni_{81}Fe_{19}/Co_{60}Fe_{20}B_{20}]_{\times 5}$ multilayer, showing negligible phase difference between $Ni_{81}Fe_{19}$ (Py) and $Co_{60}Fe_{20}B_{20}$ (CoFeB) layers. *Red circles:* Ni, *Blue quares:* Co, *Green stars:* Fe. Solid lines are sinusoidal fits. (c) Py(15nm)/Cu(10nm)/CoFeB(15nm) sample, showing the bottom Py precession lagging, with higher phase ϕ as $m_z^0 \cos\phi - \omega t$, that of the top CoFeB layer: $\phi_{\rm Py} - \phi_{\rm Co} > 0$. Magnetization precession amplitude m_z^0 for Py is estimated $\sim 10^{-3}$ rad.

a phase- and layer-specific measurement of magnetization M for structures excited near ferromagnetic resonance. Based on $\tilde{M}$, for known $\tilde{\chi}$ of a single ferromagnetic layer, we determine the depth-dependent magnetic field $\tilde{H}_{\rm rf}(z)$. Even for thin N layers, for which $k_{\rm N}t_{\rm N} < 0.01$, we find that the rf phase reaching ferromagnetic films F_1, F_2 differs by as much as ~ 0.7 rad (40°). Comparison with a classical transfer-matrix model shows that moderate conductivity loss in the substrate, present in typical device structures, is enough to generate the observed layer-dependent phase.

8.2 Experiment

8.2.1 The samples

We present data on three heterostructures deposited by UHV sputtering. Two $F_1/N/F_2$ trilayers were deposited as F_1(15)/ Cu(10)/ F_2(15nm), with F_1 on the bottom, closer to the substrate, and F_2 on the top, closer to the rf source. In the first sample ("Py/Cu/CoFeB") F_1 =$Ni_{81}Fe_{19}$, F_2 =$Co_{60}Fe_{20}B_{20}$. In the second sample ("CoFeB/Cu/Py"), the deposition order was reversed: F_1 =$Co_{60}Fe_{20}B_{20}$, F_2 =$Ni_{81}Fe_{19}$. Reversal of deposition order reverses any rf propagation delay experienced by a given layer. A third multilayer sample was deposited as a control, with a directly-exchange coupled $[Ni_{81}Fe_{19}(5nm)/Co_{60}Fe_{20}B_{20}(5nm)]_{\times 5}$ multilayer substituted for the trilayer. For this sample, we expect all F layers, strongly coupled through direct exchange, to precess in phase. All layers were deposited on the flat side of Si_3N_4 membrane windows, seeded by Ta(5nm)/Cu(3nm), and capped with Al(3nm) to protect the layers beneath from oxidation. The AlO_x side is placed closest to the coplanar waveguide (CPW) center conductor (rf source) during TR-XMCD measurement. The commercial Si_3N_4 membranes used doped Si 200 μm thick frames, rated at 1-30 $\Omega \cdot$ cm resistivity. The Si_3N_4 membrane thickness, transparent to soft x-rays in transmission, is 100 nm. A small (100 μm) hole has been drilled in the CPW center conductor where the membrane is mounted during measurement; see Ref. [59], Figure 1.

8.2.2 TR-XMCD measurements

TR-XMCD measurements were performed at Beamline 4-ID-C of the Advanced Photon Source, Argonne IL. XMCD enables measurement of *element-specific* magnetic moments through the circular dichroism of absorption at transition metal $L_{2,3}$ edges [102], taking the projection of moments along the beam helicity direction $\sigma_{\rm ph}$ as $\mathbf{M} \cdot \sigma_{\rm ph}$. For elements which are not common between layers in a heterostructure, true for Ni and Co here, XMCD is a probe of *layer-specific* magnetization, able to characterize buried layers as pictured in Figure 8.1, (a).TR-XMCD adds temporal resolution as a rf-pump / synchrotron-probe measurement of magnetization dynamics, taking advantage of the < 50 ps FWHM bunch length of the synchrotron. For continuous-wave (cw)-rf magnetic field excitation delivered through a coplanar waveguide (CPW), synchronous with the photon bunch clock, we determine the layer-specific phase and amplitude response of the magnetization $\tilde{m^0}$, as $m(t) = \tilde{m^0} \exp -i\omega t$.

The measurements were carried out at fixed helicity $\sigma_{\rm ph}$ from the APS-4ID-C circularly polarizing undulator ("CPU"; see Figure 8.1a). Samples were aligned to normal incidence by minimizing the XMCD signal in field-swept measurements ($\mathbf{H} = H\hat{\mathbf{y}}$). The out-of-plane magnetization amplitude during precession was not calibrated directly. In prior measurements at comparable input powers, slightly lower frequencies (2.2 GHz), and with $\sim 30^\circ$ incidence from normal, we measured an in-plane precessional angle 0.8° [101], or $m_y^0 \sim 0.01$ rad. For improved signal recovery, here we use lock-in detection of the XMCD signal, synchronous with rf power modulation at 5 kHz, as in Ref [59]. Given the expected ellipticity η of the Py precession, $\eta \equiv |m_y^0/m_z^0| = \sqrt{4\pi M_{\rm s}^{\rm eff}/H_{\rm B}}$, we estimate the Py precession (units of ~ 1 in Fig 8.1c) at 0.07°, or $1.2{\times}10^{-3}$ rad.

In the measurements presented, unlike those in ref. [59], we record only the (smaller) XMCD signal due to out-of-plane magnetization M_z by measuring with incident x-rays (and helicity $\sigma_{\rm ph}$) normal to the xy film plane, as pictured in Fig. 8.1a), *inset*. Normal-incidence

measurements exclude effects of ellipticity (differing m_y^0/m_z^0 ratio) on the phase of the TR-XMCD signal.

In Figure 8.1(b), we show validation and an estimate of uncertainty for the measurement of magnetization phase. In the $[Ni_{81}Fe_{19}(5nm)/Co_{60}Fe_{20}B_{20}(5nm)]_{x5}$ multilayer sample, because the thicknesses are close to the exchange lengths ($\delta_{ex} \sim 5$ nm) [103] and FMR properties are not very different for the layers, we expect mostly in-phase precession. In-phase precession is verified here to a resolution of 0.02 rad. (6 ps). To calibrate the XMCD scale, we assume that the film-normal magnetization component m_z is the same across interfaces during precession, inferring a Ni:Co XMCD signal ratio of 2:1 for equal $m_z = M_z/M_s$. This relative calibration has been applied to the data presented in Figures 8.1(c), 8.2, and 8.3a).

Layer-dependent magnetization dynamics for the Py/Cu/CoFeB sample, measured at 2.694 GHz, are shown in Figure 8.1(c). The precession of the $Ni_{81}Fe_{19}$ (Py) layer (at the bottom of the trilayer, closer to the substrate) is shown to *lag* the precession of the $Co_{60}Fe_{20}B_{20}$ (CoFeB) layer (on the top, closer to the rf source). Taking the temporal dependence as $m_z = m_z^0 \cos(\phi - \omega t)$, with $\phi = +|k|z$ for a single propagating wave incident from the CPW, we see that the magnetization phase lag ϕ for the Py layer, further away from the rf source, is greater than that for the CoFeB layer, closer to the rf source. Additionally, the precessional amplitude for the Py layer is larger, roughly twice that of the CoFeB layer. Figure 8.2 shows the layer-resolved dynamics as a function of applied magnetic field H_B. The bottom layer lags the top for all fields swept across resonance. The sweep goes from high field (driving frequency less than the resonant frequency, $\omega < \omega_0$) to resonance, with a maximum amplitude response, to low field ($\omega > \omega_0$). In the downward field sweep, the phase (lag) of each layer advances by $\sim \pi$, as expected, each maintaining an offset with respect the other.

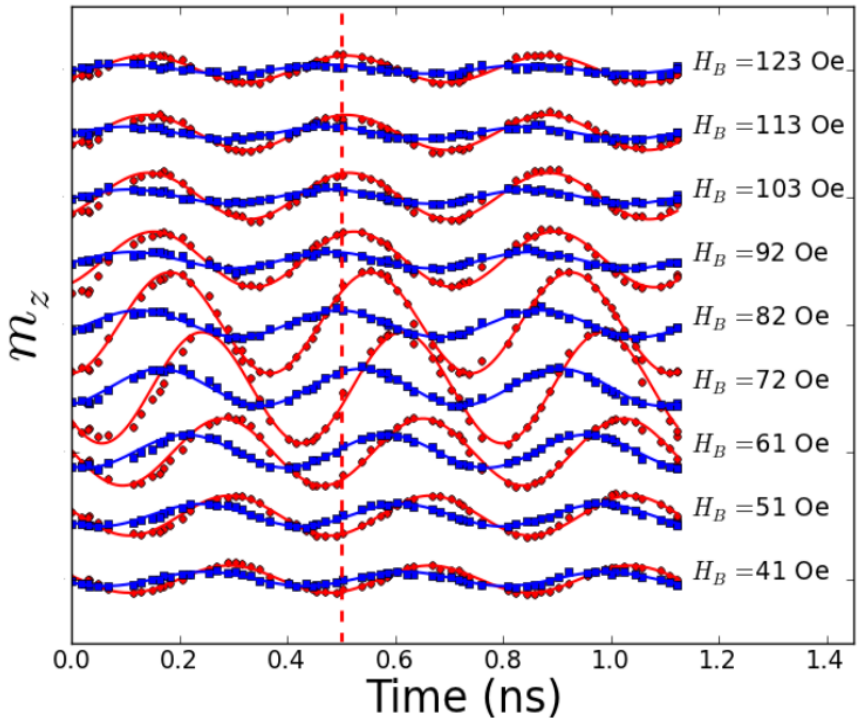

Figure 8.2: **Magnetic field bias dependence of layer-specific precession:** Time-resolved x-ray magnetic circular dichroism (TR-XMCD) data, continuously driven precession at 2.694 GHz, for substrate/Py(15)/Cu(10)/CoFeB(15nm)[top] trilayer sample. Variable magnetic field bias H_B as indicated; data are offset for clarity. Blue squares: Co XMCD. Red circles: Ni XMCD. Lines: cosine fits with variable phase ϕ and amplitude m_z^0.

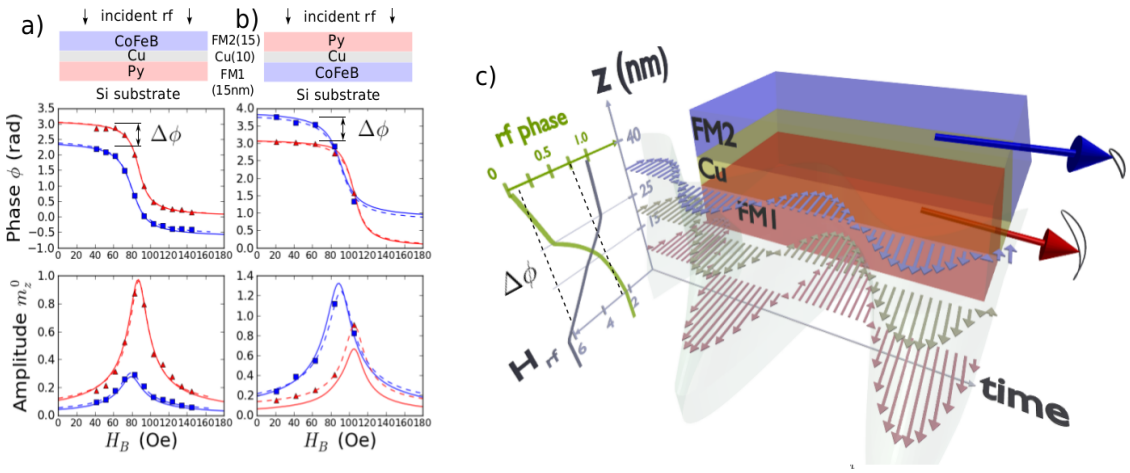

Figure 8.3: **Phase and amplitude of magnetization precession in the two layers** (a) Experimental magnetization phase ϕ and amplitude m_z^0 for substrate/Py(15)/Cu(10)/CoFeB(15nm)[top] heterostructure, driven at 2.694 GHz, after sinusoidal fits in Figure 8.2, (b) for reversed-order substrate/CoFeB(15)/Cu(10)/Py(15nm)[top] heterostructure, driven at 2.961 GHz (fits not shown), indicating phase offset $\Delta\phi$. Red: Ni (Py) resonance, blue: Co (CoFeB) resonance. *Dashed lines:* single-domain Landau-Lifshitz-(Gilbert) (LLG) fit, parameters after ref. [60]. c): Calculated rf magnetic field $\tilde{H}_{\rm rf}$ phase profile $\phi(z)$ from transfer-matrix model, indicating phase offset $\Delta\phi$ (green line, projected on left of Figure). Field amplitude ($H_{\rm rf}$, grey line) is normalized to the incident wave field H_i; magnetization motion is indicated (not to scale). Solid lines in (a), (b): magnetization response calculated self-consistently from fields as shown in (c).

8.3 Results

Extracted values of the layer-dependent magnetization phase ϕ and amplitude m_z^0, as a function of applied field H_B, are shown in Figure 8.3 (a). The variation of phase and amplitude, fitted according to the single-domain model in ref. [104] with layer-specific parameters constrained from ref. [60], is shown in dashed lines. There is a rigid positive offset in precessional phase lag $\Delta\phi = \phi_{\mathrm{Py}} - \phi_{\mathrm{CoFeB}} \sim 0.7$ rad, and roughly twice the precessional amplitude $m_z^{0,\mathrm{Py}} \sim 2\, m_z^{0,\mathrm{CoFeB}}$ for the bottom Py layer compared with that of the top CoFeB layer.

We compare the behavior of Py(15nm)/Cu(10nm)/CoFeB(15nm) with that of a reversed deposition-order CoFeB(15nm)/Cu(10nm)/Py(15nm) structure in Figure 8.3 (b). The roles of the two layers reverse: the bottom CoFeB layer is now phase-lagged compared with the top Py layer, as $\Delta\phi = \phi_{\mathrm{Py}} - \phi_{\mathrm{CoFeB}} =$ -0.62 rad, and its precessional amplitude is increased, as $m_z^{0,\mathrm{CoFeB}} \sim 2\, m_z^{0,\mathrm{Py}}$. In this sample, we have measured TR-XMCD delay scans at five field values on the low-field side of resonance, compared with eleven field values on either side of resonance for the Py/Cu/CoFeB sample. The rf field amplitudes in CoFeB/Cu/Py are thus determined with lower precision than in Py/Cu/CoFeB, reflected in the somewhat poorer fit to the model. We fitted a 5 Oe shift in resonance position for the CoFeB layer using a reduced surface anisotropy for the CoFeB/Cu interface. Again, however, the bottom ferromagnetic layer, further away from the rf source and closer to the substrate, has both a higher phase lag ϕ and a higher precessional amplitude, by comparable magnitudes.

The phase offset of rf magnetization response, primarily dependent upon depth z in the heterostructure, is most plausibly interpreted as an offset in the phase $\phi(z)$ of the driving field, $\tilde{H}_{\mathrm{rf}}(z,t) = |H_{\mathrm{rf}}(z)| \exp i\,(\phi(z) - \omega t)$. Similarly, the depth-dependent amplitude of the magnetization response suggests a depth-dependent rf field amplitude $|H_{\mathrm{rf}}(z)|$. Both features are reproduced through electromagnetic simulation of the rf field profile, illustrated in Figure 8.3 (c). The rf field profile, showing both phase $\phi(z)$ (green, top axis) and amplitude $H_{\mathrm{rf}}(z)$ (grey, bottom axis), is projected to the left grid, as calculated for an applied field H_B above the ferromagnetic resonance fields for the two layers. Time-dependent rf

magnetic fields at the midpoint of each layer, FM1(15nm), Cu(10nm), FM2(15nm), are illustrated with red, yellow, and blue arrows, respectively; elliptical magnetization motion is indicated, exaggerated in scale by two orders of magnitude for visibility. Calculations at fields below or between the layer resonances differ only slightly, by less than 15% in amplitude or phase. The magnetization response calculated self-consistently with the field profile $\tilde{H}_{\rm rf}(z)$ shown in Figure 8.3c) is shown with solid lines in Figure 8.3 (a), (b). Good agreement is found: the simulation reproduces the salient rigid phase offset $\Delta\phi$ and larger rf magnetic field amplitude nearer the substrate.

8.4 Calculations: response of magnetization to incident rf fields

The response of magnetization to incident rf fields has been calculated using a transfer-matrix approach, suggested in Ref. [104]. Kostylev [105] has investigated freestanding, conductive ferromagnetic bilayers excited by a single-sided stripline. The calculations shown in Figure 8.3 are summarized here briefly.

We assume plane-wave microwaves, linearly polarized with $\mathbf{E}$ parallel to static magnetization $\mathbf{M} \sim M_{\rm s}\hat{\mathbf{x}}$, incident normal to the "top" film side only. For the incident wave, electric field $\mathbf{E} = E_{\rm i}\hat{\mathbf{x}}$, magnetic field $\mathbf{H}_{\rm i} = E_{\rm i}\hat{\mathbf{y}}$ ($E_{\rm i} = H_{\rm i}$ for free-space propagation), and wavevector $\mathbf{k} = k\hat{\mathbf{z}}$. For the reflected wave, $H_{\rm r} = -E_{\rm r}$. In Figure 8.3 (c), left ($H - z$ plane), $H_{\rm rf}/H_{\rm i} = H_{\rm rf}/E_{\rm i} \sim 2$ since $E_r/E_i \sim -1$ for the highly reflective film stack. At the opposite side (not film-side) of the substrate, we assume a single transmitted wave propagating away from the surface into free space ($E_{\rm t} = H_{\rm t}$, $E_{\rm t}/E_{\rm i} = t$), where t is the calculated (order 10^{-3} or less) transmission coefficient $t = E_{\rm t}/E_{\rm i}$ of the full heterostructure with substrate. The assumption of plane-wave rf radiation, incident from a single (conductor) side and decaying to near zero intensity on the opposite side, is compatible with microstrip excitation and an approximation to excitation by a coplanar waveguide, as discussed in Ref. [105].

Transfer matrices M_i for layers i link E and H fields at the top ($z = 0$) and bottom

($z = d_i$) surfaces, where the individual film is bounded by $0 \leq z \leq d_i$, as (cgs units)

$$\begin{bmatrix} E(d_i) \\ H(d_i) \end{bmatrix} \equiv M_i \begin{bmatrix} E(0) \\ H(0) \end{bmatrix} \qquad M_i = \begin{bmatrix} \cos kd_i & (j/p)\sin kd_i \\ jp\sin kd_i & \cos kd_i \end{bmatrix} \tag{8.1}$$

where the given, single wavenumber k form for M_i is valid for diamagnetic or paramagnetic (not ferromagnetic) layers. In this formula, $j = \sqrt{-1}$ and the propagation constant $p = H/E = k/k_0$ is given in terms of the free-space wavenumber $k_0 = \omega/c$. For the normal-metal Cu layers, the wavenumber k is given by the skin depth δ_0, $k = (j+1)/\delta_0$, $\delta_0 = c/\sqrt{2\pi\sigma\omega}$, where σ is the material conductivity in s^{-1}. For the Si substrate, we include the full Drude form with frequency-dependent effective dielectric constant ϵ_{eff}, $k = \sqrt{\epsilon_{\text{eff}}}k_0$, $\epsilon_{\text{eff}} = \epsilon_{\text{r}} + 4\pi j\sigma_0/\omega\,(1 - j\omega\tau)^{-1}$. We took $\epsilon_{\text{r}} = 11.7$ and $\tau = 100$ fs, after (higher-frequency, W-band) experimental investigation of doped Si microwave properties. Both these matrices M have been validated against experimental data from the literature.

For the conductive ferromagnetic layer, the determination of of the transfer matrix M_i is more involved and not easily written in closed form. The Rado-Ament analysis [106] requires that the fields in the conductive ferromagnet satisfy both microwave screening through the susceptibility-reduced skin depth,

$$k^2 = \frac{2j}{\delta_0^2}\left(1 + 4\pi\chi_{\parallel}\right) \tag{8.2}$$

and the in-plane susceptibility $\chi_{\parallel}$ according to the LLG equation,

$$4\pi\chi_{\parallel} = \frac{4\pi M_y}{H_y} = \frac{h_{\text{eff}} + 1}{h_{\text{eff}}\left(h_{\text{eff}} + 1\right) - \Omega^2} \tag{8.3}$$

$$h_{\text{eff}} = h - j\alpha\Omega + K^2 \tag{8.4}$$

where the normalized field, frequency, and (spin-wave) wavenumber units are given in terms of the magnetization, gyromagnetic ratio γ, and exchange length δ_{ex}, as $h = H/4\pi M_{\text{s}}$, $\Omega = \omega/\gamma 4\pi M_{\text{s}}$, and $K = k\delta_{\text{ex}}$. Generally, the skin depth expression, Eq. 8.2, favors the buildup of shorter-wavelength spin waves in the ferromagnet and the LLG expression, Eq. 8.3, favors longer wavelengths near the (uniform-mode) FMR frequency, tending to reduce the susceptibility near resonance for finite k. The Gilbert damping is represented as α.

Equating $\chi_{\|}$ in Eqs. 8.2 and 8.3 and substituting for $h_{\rm eff}$ in terms of K^2 from Eq. 8.4 leads to a bicubic expression for wavenumber k. There are then *three* combined spin-wave / microwave modes which can propagate in either direction (or form odd and even combinations) through the film thickness.

Assuming that no boundary conditions are given, the six mode amplitudes, with the four top and bottom electric and magnetic fields $E(0), H(0), E(d), H(d)$, as in Eq 8.1, together pose ten unknowns. Four constraints are given by continuity of electric and magnetic fields at the top and bottom surfaces; four additional constraints are given by torques on magnetization due to surface anisotropies (here taken as zero). The foregoing gives a system of ten (10) linear, homogeneous equations in eight (8) unknowns. Using LU decomposition, we reduce the system to the M matrix form in Eq. 8.1, two equations in four unknowns.

The full transfer matrix of the stack, relating the electric and magnetic fields at the far side of the substrate to those at the top surface of the film, is given by the reverse-order product of the individual layer transfer matrices, $M = M_{N-1}M_{N-2}...M_1M_0$, where $i = 0$ is the first layer adjacent to the CPW (top side) and layer $i = N - 1$ is the substrate, in this case Si, with substrate thickness $t_{\rm S} = 200$ μm. The far-side boundary-condition is given by $E/E_{\rm i} = H/E_{\rm i} i = t$, where $t = E_{\rm t}/E_{\rm i}$ is the transmissivity of the full stack.

For the calculations, we used the following parameters. The values of $4\pi M_s$,$\gamma = (g_{\rm eff}/2)2\pi \cdot 2.799$ MHz/Oe, and surface anisotropy $K_{\rm s}$ (used in $4\pi M_{\rm s}^{\rm eff} = 4\pi M_{\rm s} - 2K_{\rm s}/M_{\rm s}$) for the Py and CoFeB layers, deposited as Py/Cu/CoFeB, were constrained to the values given in Ref [60], in which the layers were deposited identically. For 15 nm layers, these values yield $4\pi M_{\rm s}^{\rm eff} = 9.604$ kG (10.81 kG) for Py (CoFeB) and $g_{\rm eff} = 2.09$ (2.07). Variations in effective damping α are allowed in the simulation for best fit, obtained for $\alpha = 0.0095$ for Py and 0.0125 for CoFeB. For the CoFeB/Cu/Py structure, deposited with reverse order, the surface anisotropy for the CoFeB layer was taken to be roughly half that in the reversed configuration.

Electrical resistivites are also important for the EM simulation. We have taken representative values, not fitted, for ferromagnetic metal layers: $\rho = 20\mu\Omega \cdot$ cm for Py,

$\rho = 100\mu\Omega \cdot \text{cm}$ for (amorphous) CoFeB. For Cu, we take $\rho =$ 10-12$\mu\Omega \cdot$ cm; the lower bound of Cu resistivity was used for the CoFeB/Cu/Py structure, the upper bound for Py/Cu/CoFeB, possibly reflective of growth variation. Any influence of boundary scattering / resistivity size effect has been lumped into these parameters. The resistivity of the Si substrate was an important fit parameter; the phase offset is responsive to the substrate resistivity. This value was specified only as a range by the manufacturer of the x-ray transparent membrane, 1-30 $\Omega \cdot$ cm; we have taken 0.1 $\Omega \cdot$ cm, slightly out of the specified range, for a fit to the experimental data. The effects of the seed, cap, and nitride layers have been excluded from the simulation for simplicity; these were not found to make important differences.

Simulated results for the phase offset $\Delta\phi$ as a function of substrate resistivity ρ_{Si} are shown in Figure 8.4. For fixed substrate thickness t_S, the largest deviations of phase shift from 0 and π are found for two regions of resistivity: one narrow region at higher ρ_{Si} and one broader region at low ρ_{Si}. Note that as the substrate becomes perfectly insulating, the phase offset predicted by the simulation tends towards zero.

The conductive substrate (Si, or Si+other conductor) creates a magnetic-field minimum at the incident surface for a specific ratio of thickness t_{S} to skin depth δ_0. Application of the transfer matrix, Eq. 8.1, predicts that $\tilde{H}(0)$ is minimized for $m_{21} = m_{22}$ (row-major) for unit transmission. Top-surface magnetic fields, nearer the rf source, are then minimized for substrate thickness $t_S \sim \delta_0\,(k_0\delta_0/2)$. Note that this magnetic field minimum does *not* occur for a substrate thickness equal to the skin depth, but rather for substrate thicknesses substantially thinner, in this case $\sim 0.08\delta_0$, corresponding to $\rho_{\text{S}} =$7.4Ωcm. Near this minimum, the phase of $\tilde{H}(0)$ varies rapidly as a function of conductivity for fixed thickness t_{S}.

If a more conductive layer is introduced in contact with the substrate, on the same side as the rf source, the substrate resistivity ρ_{S} for which the magnetic field is minimized shifts to lower values. The high-ρ_{S} region of large $\Delta\phi$ occurs where the field at this surface is minimized, as the real part of H changes sign. Note that the position is sensitive to the bottom (F_1) layer resistivity, here Py, and shifts to lower ρ_{S} for lower ρ_{Py}. The phase vari-

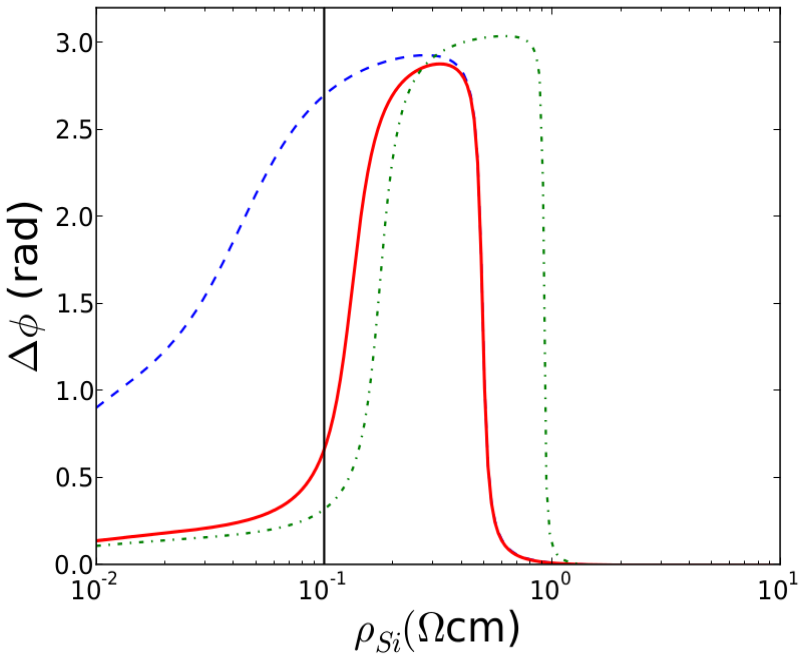

Figure 8.4: **Calculated phase offset:** Calculated phase offset $\Delta\phi$ as a function of the Si substrate resistivity ρ_{Si}. Solid line, with fitted ρ_{Si} =0.1Ωcm (vertical line), shows the configuration treated in Figure 8.3 (a); calculations for decreased Cu layer resistivity ($\rho_{\mathrm{Cu}} = 2.0\mu\Omega \cdot \mathrm{cm}$) and increased bottom Py layer resistivity (F_1), ($\rho_{\mathrm{Py}} = 40.0\mu\Omega \cdot \mathrm{cm}$) are shown in blue dashed and green dot-dashed lines, respectively.

ation in the top layer (F_2) is shifted to even lower values of ρ_{S}, due to the larger thickness of conductive metal beneath it; we show that the breadth of this region is controlled by the Cu resistivity in the simulation, much broader for 2 $\mu\Omega$cm (near the lower bound for Cu) than for 15 $\mu\Omega$cm. The fields can thus become out of phase at different positions in the heterostructure, as found through the TR-XMCD measurements and reproduced in the simulations.

8.5 Discussion

The physical content of the simulations consists solely of Maxwell's equations for the conductors and the Landau-Lifshitz-Gilbert (LLG) equation for the ferromagnets, as outlined in classic work by Rado and Ament [106]. The layer-specific magnetization response is interpreted as a *local* measurement of complex, thickness-averaged magnetic fields $\tilde{H}$ in the layers.

In the experiment, the layer magnetizations respond to time-dependent effective magnetic fields, not simply the *rf* auxillary fields sourced by the waveguides. Known sources of time-dependent effective fields include interlayer coupling: either magnetostatic / Neel, or dynamical / spin pumping [107]. Neither type of coupling will reproduce the phase offset observed and coupling has been neglected in the simulation. For effective fields from coupling alone, the influence on dynamics of layer i will be maximized near the ferromagnetic resonance of layer j and become negligible at much higher or lower fields. While we cannot exclude the possibility that the phase offset arises in part from yet-unidentified terms to the LLG, propagation effects alone provide a sufficient and plausible interpretation of the results.

Conductivity of the moderately doped Si substrate, supplied as a support for the membrane used in the experiment, plays the most important role in generating the inhomogeneous fields and phase offset $\Delta\phi$, according to the simulation. The simulation (see *Calculations*) shows that maintaining F, N, and substrate layers much thinner than the skin depth, $t_i \ll \delta_0$, does *not* ensure a homogeneous rf magnetic field through the film thickness, consistent with the results presented here.

It is not clear to what extent the measured $\Delta\phi$ ~0.6-0.7 rad is typical for spin-valve-type structures at frequencies near 3 Ghz. We may comment that we have observed similar phase offsets $0.4 < \Delta\phi < 1.0$ rad, never less, in a larger and less well-controlled set of spin-valve samples than those presented here. These structures have had thinner F layers (to 5 nm), thicker Cu layers (to 20 nm), different compositions of Co-rich layers, membrane supports used from two different manufacturers, film depositions carried out in three

separate systems by three separate groups, and *rf* frequencies varying from 1.8-4.1 Ghz. Nevertheless, our simulations predict (see *Calculations*), though our experiments have not tested, that an appreciable phase offset, up to π, would be expected for a specific range substrate resistivity, amounting to one or two decades, for a given substrate thickness. Only a negligible phase offset is predicted for an insulating, lossless substrate.

8.6 Conclusions

The experimental results demonstrate that time-resolved, core-level x-ray spectroscopy can be used as a layer-specific, phase-resolved probe of EM radiation in a nanometer-scale heterostructure. We comment finally on perspectives of the technique. The full range of magnetoelectronic heterostructures, including magnetic tunnel junction stacks [108] and layers down to several nm thicknesses, are accessible at sheet level. Phase-resolved $\tilde{H}$ fields might also be probed with layer specificity in sub-micron patterned structures, using analogous focused x-ray techniques such as scanning transmission x-ray microscopy (STXM), applied recently to the study of smaller-angle precessional dynamics [109]. Finally, outside the domain of thin-film magnetism, depth-dependent $\tilde{E}-$fields might be probed in dielectric or ferroelectric heterostructures using x-ray linear dichroism measurements of layer-specific polarization order [110], particularly as novel light sources begin to probe THz and higher frequencies.

Chapter 9

Time-resolved scanning transmission x-ray microscopy for resolving small-angle magnetization dynamics in confined geometries

In this chapter, we look at the magnetization dynamics in ferromagnetic (FM) thin film heterostructures with confined geometries, carried out by time-resolved scanning transmission x-ray microscopy (TR-STXM) at the 10ID-1 SM (soft x-ray microscopy) beamline of the Canadian Light Source (CLS). The origin of the magnetic contrast and the pump-probe technique are identical as discussed in Chapters 7 and 8. The advantage of the STXM is that instead of using a micrometer sized x-ray beam as in XMCD spectroscopy, the x-ray beam is focused to a spot size of $\sim$ 35 nm with a Fresnel zone plate (illustrated in Fig. 9.1); higher resolution up to less than 15 nm [111] is available based on better x-ray optics. Therefore, in contrast to the XMCD spectroscopy which could only access the **M** averaged over the beam cross-section area, localized magnetization dynamics could be detected. In

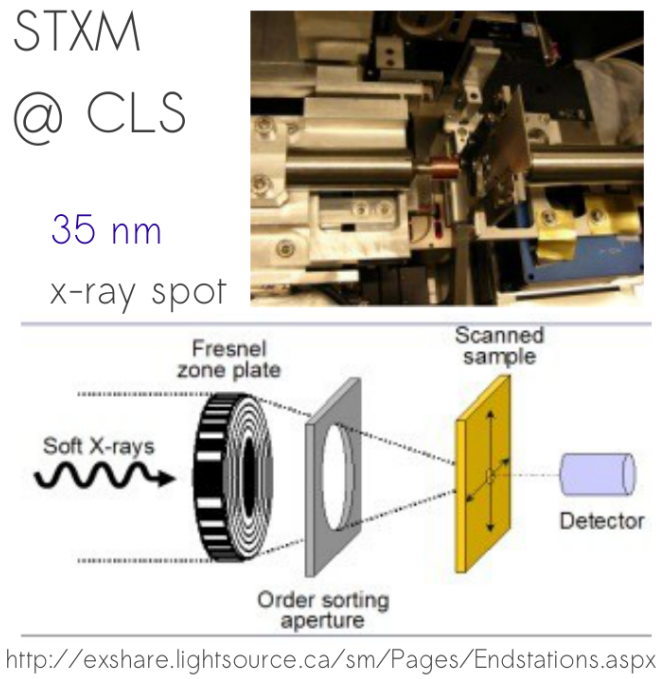

Figure 9.1: STXM at CLS. *Upper* panel: photograph of the STXM end station; *lower* panel: diagram showing the components corresponding to the photograph.

addition, x-ray microscopy techniques, with their enormous resolving power and ability to access buried layer magnetization, have never before been used to probe small-angle GHz dynamics in FM structures. Here we present the first experiments imaging ferromagnetic resonance (FMR) in confined geometries using x-rays.

I will devide this chapter on the TR-STXM work into three parts. The first section concerns the slow (< 2 kHz) dynamics in micron-size $Ni_{81}Fe_{19}$ thin-film elements, showing the magnetization switching behavior and domain wall propagation with the synchronous (lock-in) technique utilizing a dual-gate photon counter, and discusses the limitation of this technique. The second part demonstrates the first x-ray experiment of detecting small-angle ($< 20°$) magnetization dynamics with submicron spatial resolution and ps time resolution, establishing the prototype for the experiment and data analysis of FMR-STXM. The final section is the central result of this chapter, in which we demonstrate the first phase-resolved

imaging of spin-wave eigenmodes in submicron FM thin film ellipses, with $\sim$ 40 nm resolution and the ability to distinguish degenerate modes with different symmetries, long predicted by micromagnetic simulations.

9.1 Stochastic limits in synchronous imaging of sub-micron magnetization dynamics

In this section, we demonstrate a synchronous (lock-in) technique for imaging thin-film magnetization dynamics using STXM. Gated photon counting synchronized with magnetic field modulation allows image acquisition with differential contrast for high and low magnetization. We have applied this technique to 5×12 μm^2 $Ni_{81}Fe_{19}$ ellipses with well defined closure domains at remanence. The stochastic nature of domain wall motion and nucleation is apparent in images recorded during cycling along successive major hysteresis loops. Synchronous imaging shows the clearest enhancement of contrast for small-amplitude domain wall motion, with less obvious benefit at higher fields/displacements. While this technique shows promise for contrast enhancement of magnetization in dynamics in STXM, we did not use it in subsequent experiments due to its instrumental complexity as will be discussed below.

9.1.1 Introduction

Magnetization dynamics of soft FM thin-film patterned structures play a fundamental role in a wide range of applications, including but not limited to magnetic recording devices and emerging spintronic technology [112–114]. Recent research has focused on high frequency dynamics into the GHz range, driven by the demand for faster-operating devices [115–117]. However, low-frequency dynamics are also of interest for other devices such as integrated inductors, which operate at rates below 500 MHz [118, 119]. Low-frequency dynamics are critical for analyzing magnetic reversal and domain wall propagation processes. Time-resolved magnetic microscopy offers the potential to image the domain dynamics, studied

to date through other means [120, 121].

We have developed a technique to provide and ultimately enhance dynamic magnetic contrast in STXM. The simple application of 'pump-probe' techniques [122], where the pump signal is synchronized with the x-ray bunch clock and its higher harmonics, provides a lower limit of several hundred MHz at most synchrotron facilities. Techniques have been developed to characterize pulsed dynamics at repetition rates less than the bunch frequency. Acremann *et al.* implemented a sophisticated software-defined photon counting system to this end [123]. Due to the typically low incident photon flux (10^8ph/s), photon counting is the preferred acquisition mode in current STXM's.

We present a simpler differential photon counting approach for a moderate frequency regime. Using a commercial dual-gate photon counter for image acquisition, we take as the image basis the difference between transmitted photon counts at high and low points on a modulating field cycle. Because the minimum gate width is 2 ns, low-frequency dynamics over a frequency range of 200 MHz to dc can be probed straightforwardly. Here we demonstrate this technique in domain imaging of micron-size $Ni_{81}Fe_{19}$ ellipses with well defined closure domain states. Different domain configurations were observed for identical sweep cycles during the static study. The stochastic nature of domain dynamics in these structures gives an explaination for varied constrast observed in the differential images obtained at $\leq$2 kHz frequencies, with best imaging found for small domain displacements.

9.1.2 Experimental Technique

Two patterned structures, a single layer element and a bilayer element, were investigated. The preparation conditions were chosen to yield materials of optimal soft magnetic properties. Coercive field $H_c < 1$ Oe was seen in identically deposited unpatterned films at 16 Hz. For the first sample, a 15 nm layer of $Ni_{81}Fe_{19}$(Permalloy) was deposited on a 200nm Si_3N_4 membrane using UHV magnetron sputtering, with DC power 200 W and Ar pressure 1.2 mTorr, at a deposition rate of 3.2 Å/sec. 3 nm Ru was sputtered prior to Permalloy as a seed layer to give better soft magnetic properties, and 10 nm MgO serves as a cap to

protect Permalloy from oxidation. Arrays of elliptical elements (5 μm$\times$12 μm) were fabricated using photolithography and a lift-off process. For the bilayer sample, the dimensions of ellipse were changed to 5 μm$\times$24 μm, and a sandwich structure of 15nm Permalloy/ 5nm Ru/15nm Permalloy replaced the sigle 15 nm Permalloy layer, while other conditions remained the same.

The scanning transmission x-ray microscopy (STXM) measurements were carried out at the Canadian Light Source (CLS), soft x-ray spectromicroscopy beamline 10ID-1 (SM), with x-ray photon energy set to the Fe L_3 edge at 707eV for maximal x-ray magnetic circular dicroism (XMCD) signal [124]. The circular polarization of incident x-rays is fixed during each image acquisition. Figure 9.2 shows the configuration of the experiment for dynamic measurements. As illustrated in 1 a), the thin film element lies in the xz plane, with its normal pointing in the y-direction. X-ray is propagating in the xy plane, 30° away from sample plane normal. The projection of the element's in-plane magnetization onto x-ray propagation direction contributes to the contrast at each pixel. The x-ray spot (40 nm at optimal focus) is scanned over the element to form an image [125, 126].

We used a commercial dual-gate photon counter with minimum gate width of 2ns to detect transmitted x-ray intensity. During operation of the dual-gate photon counter, the number of photons detected over a time interval set by a gate width is counted, then integrated over a specified number of counting periods to give adequate signal intensity. The starting point of the counting period is determined by a delay with respect to the trigger signal. To apply magnetic fields, we used wound Cu coils of turn density $\sim$1-10 mm^{-1} with ferrite cores. The core material was tapered and positioned as close as possible to the sample stage of the STXM. The ferrite cores are rated for a flat frequency response to >1 MHz; ac fields were driven in constant voltage mode (square wave) and calibrated by ac gauss probe as a function of frequency. Field values cited have a high ($\sim$50%) uncertainty between Fig. 9.5 (a), (b), (c) because the core was repositioned in each case and could not be calibrated *in-situ*.

Figure 9.2 (b) explains the temporal resolution. A function generator applies a

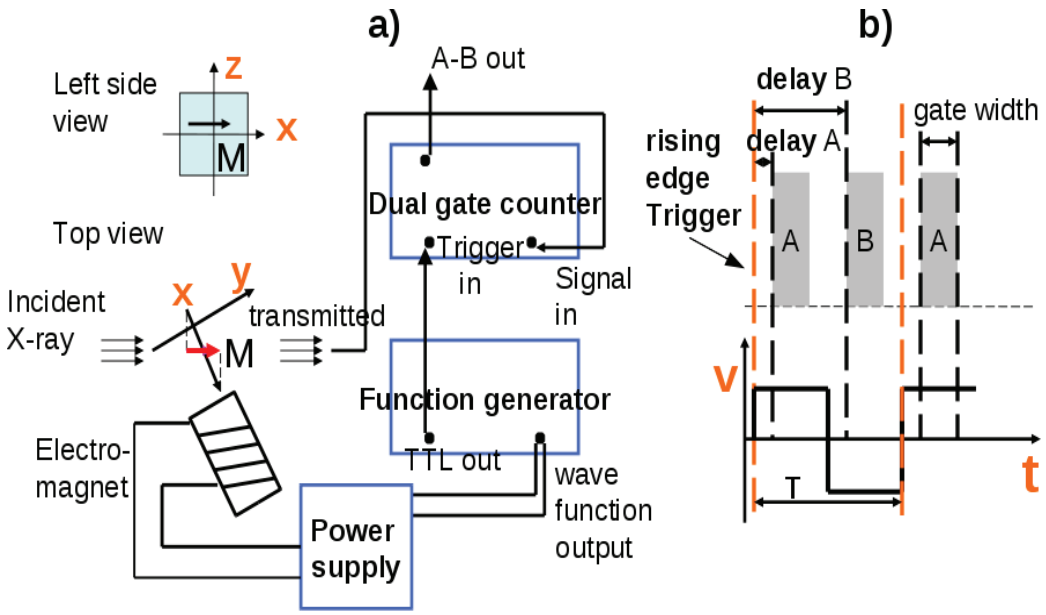

Figure 9.2: Experimental setup at CLS 10ID-1. (a) Configuration of incident x-ray beam, sample plane and photo detector; Equipments setup for photon counter and function generator; (b) The wave function, trigger signal and configurations for the 2 counting gates. See text for details.

square wave voltage to the coils of the ferrite-core electromagnet, exerting alternating in-plane magnetic field to the element. The rising edge of TTL output from function generator triggers the photon counting gates. The widths of the 2 photon counting gates A and B were both set to 1/5 of the square wave period T (ms). The delay of gate A was set to 1/20 T while gate B lagged gate A by a half period. We took the images with 100 pixels in the x-direction and 25 pixels in the z-direction, respectively. The microscope dwelled at each pixel for 120 ms. The number of counting periods N for signal integration was thus set accordingly for each aqcuisition frequency, $N = 60/T$, to allow for 2 data points at each pixel. The differential signal A-B is then converted to an analog voltage and sent through a voltage-to-frequency converter before being recorded by the microscope.

For static hysteresis loop measurements, we cycled the static field between -15 and +15 Oe along both axes of the single-layer ellipse. STXM images with both x-ray helicities at each static field point were taken. Subtracting the 2 images in software gives the differential contrast. The normalized magnetizations were obtained from the area ratio of the

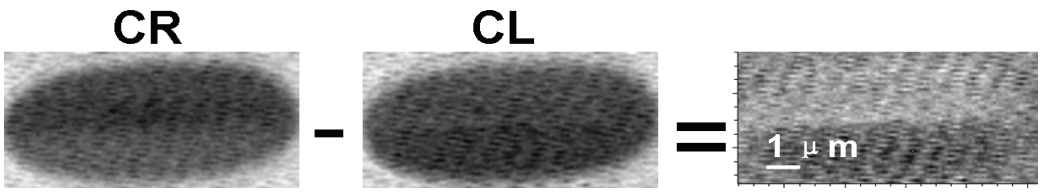

Figure 9.3: The $5\mu m \times 12\mu m$ element, static domain structure at zero field, in the horizontal configuration. Here, CL denotes circular-left polarization, and CR denotes circular-right polarization; the XMCD image is on the right.

domains with the opposite contrasts (dark and bright).

9.1.3 Results and discussion

The static hysteresis loop was measured for the single-layer element in the horizontal configuration, with its short axis lying in the z-direction and the applied field in the x-axis. Figure 9.3 shows the remanent state. At zero applied field, the element appeared to be in a well-defined 2-domain state with equal areas. Note that closure magnetization at the ends, if tangent to the boundary as expected, will show no contrast in this geometry. We cycled the sweeping field twice, starting from saturation at -12 Oe, increased the field to +12 Oe, and looped back to -12 Oe again to complete the cycle. Domain patterns at different field points during the first cycle are displayed in Fig. 9.4 (a), showing the area change in the 2 domains. The overall hysteresis loop for the first cycle is shown in Fig. 9.4 (b) as dots. During the second cycle, represented on the loop by triangles, the element showed a different domain pattern as the applied field decreased from 12 Oe to 0 Oe. This behavior is shown in the upper panel of Fig. 9.4 (c). In the lower panel, the element took a diamond pattern for zero net magnetization, instead of the 2-domain state.

The observed domain images, taken on the major loop, clearly show a stochastic component to the reversal behavior. The different states can be understood through the simulation results obtained by Hong *et al.* [127]; the domain configuration initiated in the *c-state* from saturation in the first cycle, and took the *s-state* in the second cycle. Due to

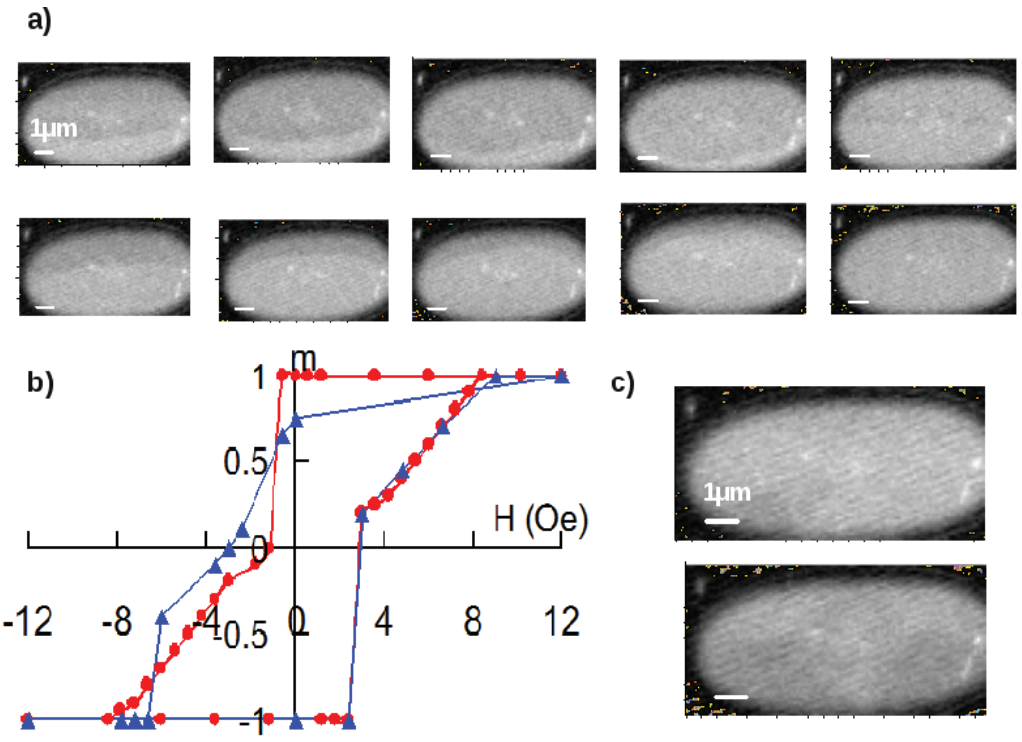

Figure 9.4: 15 nm Permalloy ellipse static hysteresis loops, horizontal configuration. The bar equals 1 μm. a). Field strengths from left to right 3, 5.4, 7.2, 7.8, 8.4 Oe; Opposite direction in upper and lower panels. b) Hysteresis loops by converting relative areas into normalized magnetization; red curve (dots) the first cycle, blue curve (triangles) the second cycle. c) Different domain structures (diamond pattern) in the second cycle. Upper panel 0 Oe, lower panel -5.4 Oe.

the near-degeneracy in lowest energy domain configurations, the same spot in the sample is likely to have opposite magnetization directions during different magnetization cycles from saturation. In dynamic measurements where the transmitted photon counts are integrated over multiple cycles, inconsistency between cycles will lead to reduction in contrast, compared with static imaging.

Figure 9.5 demonstrates the dynamic images. In Fig. 9.5 (a), the bilayer element is fully switched in a 500 Hz square wave external field, reversing at 7 Oe amplitude. The enhanced contrast is compared with the corresponding static XMCD images, acquired by subtracting two images taken at opposite bias field directions with the same x-ray polarization. When the element is not fully switched by the alternating external field during dynamic acquisitions, the area through which the domain wall moves during the cycle will

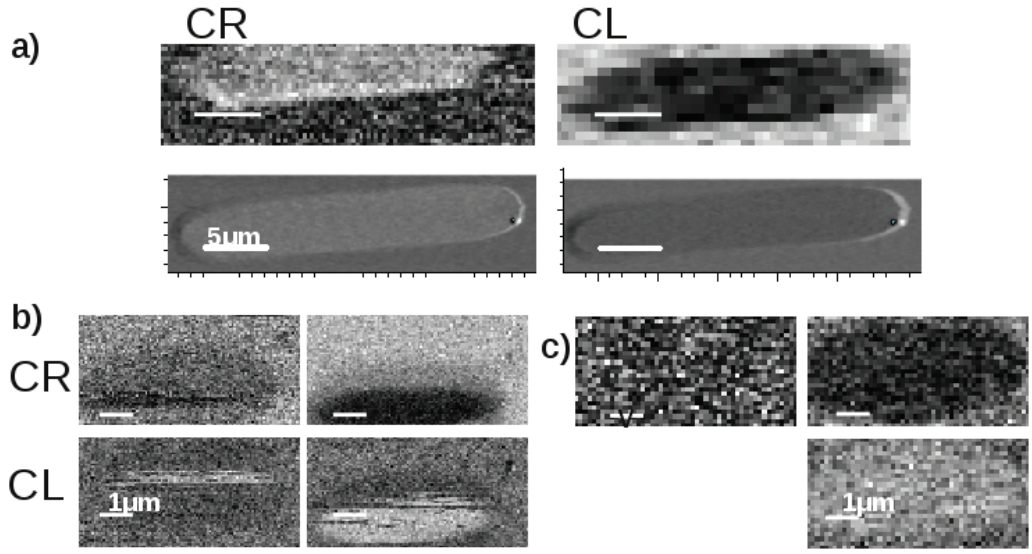

Figure 9.5: Dynamic images, fields are estimated to 50% precision: a) Bilayer $5\mu m \times 24\mu m$ element, applied field 7 Oe along the long axis, fully switched. Upper panel dynamic images, taken at 500 Hz, lower panel static. b) Horizontal configuration for $15nm \times 5\mu m \times 12\mu m$ element, applied field frequency 500 Hz. As the field amplitude goes from 2 Oe to 4 Oe, the switched area in the element grows. c) Horizontal configuration for single layer element at 2 kHz. First column (field amplitude 3.5 Oe) shows an example of no contrast due to stochastic domain motion; second column (field amplitude 21 Oe) shows the contrast for fully switched element.

show contrast. This area is expected to be roughly proportional to the applied field strength. The images in Fig. 9.5 (b), taken at 500 Hz for the single layer element, show such a trend as the field is increased from left to right. In Fig. 9.5 (c), the images were taken at 2 kHz. At field amplitude 3.5 Oe, the picture shows no detectable contrast. We do not expect the dynamic coercivity to play a role at these sweep rates ($dH/dt <\sim 1 \times 10^4$ Oe/s); threshold rates have been measured in the range $10^6 - 10^7$ Oe/s [120]. We attribute the relatively low contrast in Fig. 9.5 (c) to stochastic effects along the major loop. When the field amplitude is 21 Oe, the fully switched element shows contrast.

9.1.4 Summary

In conclusion, we have demonstrated a new approach to time-resolved measurements in x-ray microscopy, not constrained by the bunch clock at synchrotron facilities. Implementing the concept of lock-in detection, the differential signal allows contrast enhancement provided that the process under investigation is reproducible over multiple cycles which are necessary for signal integration. The scope of this technique can also be extended to contrast enhancement in precessional magnetization dynamics of nanostructures. Lock-in amplification of transmitted diode intensity under RF field modulation has provided a 1-2 order of magnitude improvement in signal detector in time-resolved XMCD in [59]. When a differential signal is not required, any of the two gates can perform the regular photon counting at flexible rates and delays.

We note here that in the experiments presented in the remaining sections of this chapter, we did not make use of the synchronous photon counting technique; time was too limited in the typical allocation of $\sim$ five shifts (40 hours) to set it up with the other instrumentation, and contrast was found to be adequate. The synchronous photon counting technique will become more feasible if TR-STXM instrumentation becomes more permanent at a beamline in the future.

9.2 Submicron mapping of GHz magnetic susceptibility

In this section we report submicron imaging (∼0.75 μm resolution) of complex magnetic susceptibility in a micron-size ferromagnetic heterostructure using TR-STXM. The real and imaginary parts of the susceptibility are extracted from the phase and amplitude of the small-angle ($< 20°$) rotational response of the local magnetization under microwave excitation. The experimental technique and the method for data analysis presented here deserve special attention, since they are the standard routine for further FMR-STXM experiments with higher spatial resolution and for probing smaller magnetization precession angles, which will be described in Chap.9.3. In the experiment presented here, frequency-dependent response patterns were observed in an incompletely saturated bilayer element. As we show in Chap. 9.3, this technique is extensible to better spatial resolution ($\sim$ 40 nm), and to higher frequencies (to ∼10 GHz) and layer-specific measurement.

9.2.1 Introduction

High frequency ($>$ 1 Ghz) magnetization dynamics of patterned magnetic heterostructures are of interest for a wide variety of applications, including high data-rate magnetic information storage [128, 129], on-chip power conversion [14, 118], and emerging applications in microwave signal processing [130, 131]. The dynamic response can be described completely by the complex, frequency-dependent susceptibility $\widetilde{\chi}(\omega)$, for arbitrary applied field pulses, if the magnetization response is linear. Pump-probe magneto-optical imaging techniques [132] have been used to image $\widetilde{\chi}(\omega)$ in symmetric [133, 134] and nearly uniformly magnetized [135] micron-size structures, with a best resolution of $\sim$ 300 nm.

Soft x-ray microscopies have compelling advantages for imaging the magnetization response in device-relevant structures [136]: superior spatial resolution (to 15 nm) [111], relevant temporal resolution ($<$ 30 ps), and the capability to image individual magnetic layers buried $\sim$ 1 μm below electrical leads. However, dynamic imaging through x-ray techniques had been limited before to the characterization of gyrotropic vortex motion [137,138], behavior which generates high contrast in XMCD. It had not been clear that the phase-sensitive

small-angle dynamics characterized in time-resolved XMCD [139], from which $\widetilde{\chi}(\omega)$ can be inferred [59], could be imaged in x-ray microscopy. This would be useful to characterize the majority of devices, or device-relevant structures, which are biased close to a uniform magnetization state. PEEM measurements have succeeded in characterizing the phase-resolved response, but only at a few discrete points, at the expense of large spatial averages (> 4 μm) [140], in a flux-closed square element.

In this section, we show that scanning transmission x-ray microscopy can be used to image phase-sensitive small-angle dynamics with submicron resolution. We have imaged the susceptibility $\widetilde{\chi}(\omega)$ at frequencies of 0.5-4.0 GHz in an incompletely saturated 7.5 $\mu m\times$ 30 μm ellipsoidal CoZrTa(20 nm)/SiO_2(7 nm)/CoZrTa(20 nm) bilayer element, with a sensitivity of $\sim 10^\circ$ at a spatial resolution of 0.75 μm. The phase and amplitude of the response are consistent with diversity of local resonance fields, but with a greater fraction being in resonance near 2 GHz. The technique, which is extensible to much finer spatial resolution as shown in Chap. 9.3, will enable imaging of susceptibility in submicron structures, making it possible to characterize layer-resolved magnetic eigenmodes in individual nanometer-scale structures.

9.2.2 The sample

A ferromagnetic(FM)/nonmagnetic(NM)/ferromagnetic(FM) sandwich structure, Ta (3 nm) / $Co_{91.5}Zr_{4.0}Ta_{4.5}$ (15 nm) / SiO_2 (2 nm) / Ta (3 nm) / $Co_{91.5}Zr_{4.0}Ta_{4.5}$ (15 nm) / SiO_2 (10 nm), was sputtered on a 200 nm Si_3N_4 membrane, and patterned into 7.5 μm$\times$ 30 μm elliptical elements with photolithography and lift-off process. The bottom 3 nm Ta layer is a seed layer to improve adhesion and homogeneity of the film. The top SiO_2 layer protects the metallic film from oxidation. The SiO_2(2 nm)/Ta(3 nm) bilayer in the middle serves as a 5 nm NM spacer layer. The FM layers $Co_{91.5}Zr_{4.0}Ta_{4.5}$(15 nm) were DC magnetron sputtered at optimized conditions to achieve soft magnetic properties (coercive field $H_c < 1$ Oe), with power 250 W, Ar pressure 1.2 mTorr, and deposition rate 3.8 Å/sec. An external

magnetic field of 50 Oe was applied along the long axis of the elliptical element during deposition. The induced anisotropy field H_K was measured to be 20 Oe in unpatterned films. For further details on the deposition system, see ref. [12].

9.2.3 Experimental technique: FMR-STXM

As in sections 9.1 and 9.3, we carried out the STXM measurements at the Canadian Light Source (CLS), soft x-ray spectromicroscopy beamline 10ID-1 (SM, minimum x-ray spot size 25 nm), with x-ray photon energy set to the Co L_3 edge at 779 eV for maximal x-ray magnetic circular dicroism (XMCD) signal [124]. To enhance the final contrast, we take two images under the same conditions, with x-rays of left- and right-circular polarization (CL and CR) respectively, subtract the two images(CR-CL) and convert the difference into optical density(OD),

$$OD = log_{10}(I_0/I_1),$$

where I_0 is the intensity of the incident x-ray before passing through the thin-film stack, and I_1 is the intensity of the transmitted x-ray. We took the average of the difference image (CR-CL) contrast over a large area on the bare membrane as I_0.

The diagram of the experimental setup is shown in Fig. 9.6 (a). The sample was mounted on a custom-designed coplanar waveguide (CPW), with a hole (100 μm diameter) in the center conductor allowing for x-ray transmission in the z-direction. The long axis of the elliptical element is arranged parallel with the center conductor, in the y-axis. The sample plane is tilted 30° away from the x-axis, to visualize the in-plane magnetization. In order to obtain a domain configuration other than the flux-closed remanance state and avoid the stochastic motion of domain walls under excitation [141], a static magnetic field of aprroximately 20 Oe was applied horizontally with a homemade electromagnet, with copper wire wound round an iron nail to fit into the compact vacuum chamber. The tip of the nail was positioned as close to the sample as possible, providing a concentrated magnetic flux over the element under investigation. Fig. 9.6 (b) compares the domain structure of the element at the demagnetized state and after the external dc field was applied. Note that

an accurate measurement of the field amplitude could not be performed due to the limited space inside the vacuum chamber, and an error of 20% is estimated.

For time-resolved measurements, we implemented the same '*pump-probe*' methodology for TR-XMCD experiments as described in ref. [59]. The x-ray bunch length is 35 ps and the bunch frequency is 500 MHz. The bunch clock signal is sent through a comb generator and then filtered to give a desired harmonic of 0.5 GHz, providing the rf excitation signal. For frequencies of 0.5 GHz, 2.0 GHz and 4.0 GHz, we kept the input rf power to the CPW constant at 1 W (+ 30 dBm) by adjusting the attenuators in the rf circuit and confirming the power value using an rf power meter, measured at the input to the STXM chamber. The delay line defines the relative position of the 'probe' versus the 'pump', and we chose the sampling rate to be 25 points per period for all three frequencies. For each image in the time series, we take an averaging window of 5× 5 pixels (0.75 μm× 0.75 μm square), scan it over the 227×100 pixels (34 μm×15 μm) image area at 1-pixel step. At each step, the averaged contrast over the window area is plotted against the delay time and fitted with a sinusoidal function, yielding both the amplitude of the local magnetization change as well as its phase compared with the driving rf signal. The offset from zero of the sinusoidal function refers to the local static contrast, as observed in the biased element in Fig. 9.6 (b). Fig. 9.6 (c) demonstrates the contrast as a function of time over the period (500 ps) of the 2.0 GHz excitation, in representative areas in the biased element. While the domain configuration displays no obvious shift, contrast plotted here in areas A, B and C shows clear oscillatory behavior with different amplitudes, phases and offsets. The background area BG sits on the bare Si_3N_4 membrane and shows close to zero optical density and no sinusoidal variation. We performed this analysis for the element under 0.5, 2.0 and 4.0 GHz excitations. Even though the excitation power is fixed, the element responds with larger oscillation amplitude at 2.0 GHz, while at 4.0 GHz (not shown) the response is considerably weaker and shows much more variance in the fitted parameter.

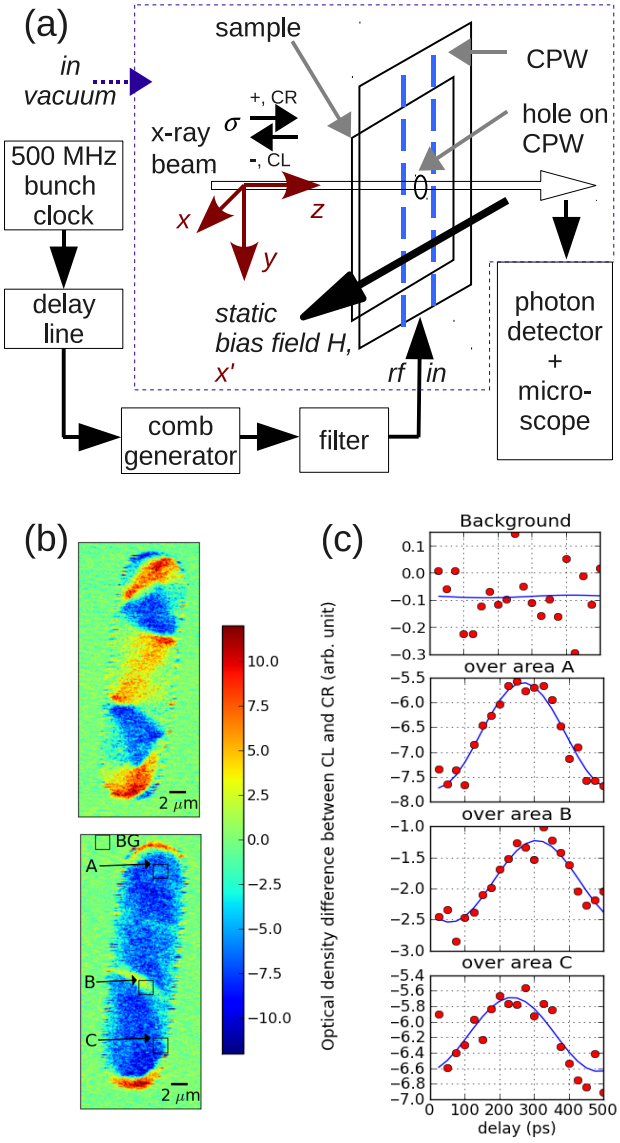

Figure 9.6: (a) layout of the experimental setup; (b) domain configuration of the element; upper panel: demagnetized state; lower panel: 20 Oe field applied in the x-direction; (c) time-dependent contrast fitted to sine wave, under 2 GHz excitation in the biased element, in selected areas BG, A, B and C, marked out in the lower panel of b).

9.2.4 Data analysis

Next we describe our method for extracting processional amplitude of the incompletely saturated element. Assuming the magnetization lies in-plane (x'y-plane) and no domain wall propagation takes place under the excitation, we interpret the dynamic response of the biased element as rotation of the local magnetization. We extracted the precessional amplitude of in-plane magnetization rotation α from the fitted functions as illustrated in Fig. 9.7 (a). At each location, the normalized magnetization $\mathbf{m}$ forms an angle θ with the x'-axis. The observed static magnetization contrast is proportional to the projection of $\mathbf{m}$ onto the x'-axis, $cos\theta$. This is also the offset of the fitted sine wave. The maximum contrast occuring in the elements corresponds to $\mathbf{m}$ parallel with the x'-axis. Under rf excitation, $\mathbf{m}$ oscillates at an angle α. In the small-angle limit of precession, the full range of precessional motion(arc l), equal to α in value, projects onto the x'-axis as $\Delta = lsin\theta$. The observed low-amplitude change in local contrast is thus related to the rotation angle α as shown in the right panel of Fig. 9.6 (a). The resulting maps of local magnetization rotation angle and the phase for both 0.5 GHz and 2.0 GHz are shown in Fig. 9.7 (b), which accentuate the difference in the response pattern at the two frequencies. At both frequencies, the areas showing highest contrast on the rotation angle map correspond to a phase around 90°, implying resonance. At 0.5 GHz these areas concentrate at the domain edges while at 2.0 GHz the major area within the domains gives larger rotation angles. It is likely that at those locations where the magnetization sees a more abrupt change, the local exchange field acts against the bias field, leading to a smaller effective field and thus lower resonant frequency. We eliminated the analysis for 4.0 GHz, since the observed response was very small and noisy, as expected for driving frequencies above resonance.

Finally we demonstrate the mapping of local susceptibility (real part and imaginary part)

$$\widetilde{\chi}(\omega) = \frac{Me^{j(\omega t-\delta)}}{H_o e^{j(\omega t)}} = \frac{M}{H_o}cos\delta - j\frac{M}{H_o}sin\delta = \chi' - j\chi"$$

at 0.5 GHz and 2.0 GHz in Fig. 9.8, derived from the amplitude and phase δ of the sine fit. The saturation magnetization of $Co_{91.5}Zr_{4.0}Ta_{4.5}$ film is 17 kOe, measured by FMR, which

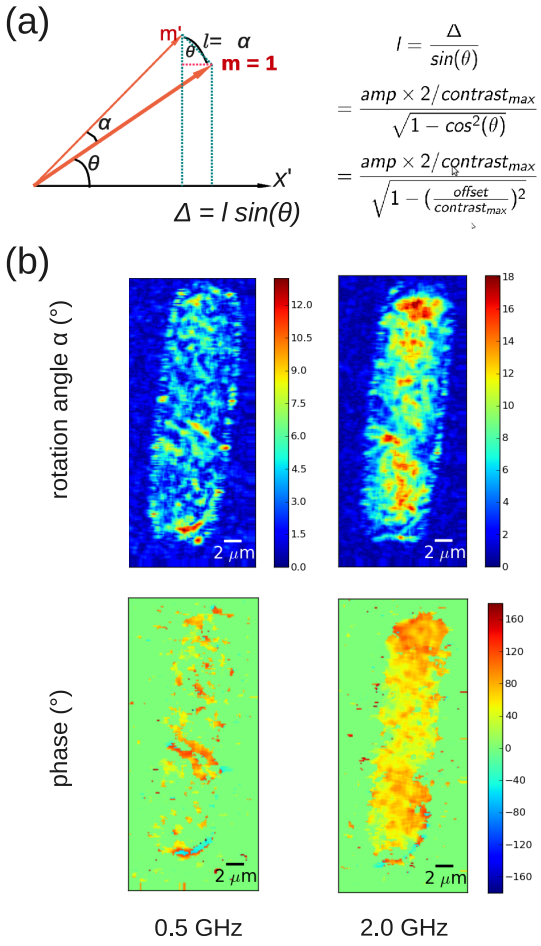

Figure 9.7: (a) Sample plane $x'y$: illustration of converting contrast variation (Δ) to magnetization rotation angle (α); (b) magnetization rotation angle and phase in the element under 0.5 GHz and 2.0 GHz excitations; the two phase maps in the lower panel share the same scale bar.

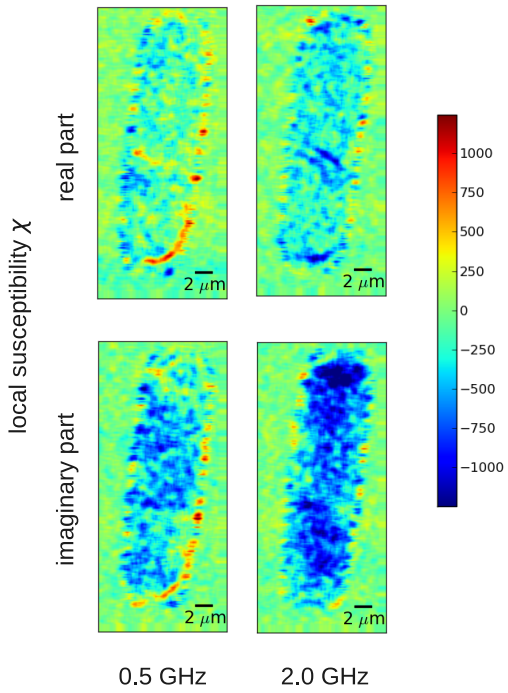

Figure 9.8: Real and imaginary part of the complex susceptibility, 0.5 GHz and 2.0 GHz.

corresponds to the optical density contrast of 11 in the element. The amplitude of the sine fit at each pixel is therefore converted to ΔM. The rf magnetic field amplitude on the CPW (400 μm center conductor width, 50 Ω impedance, +30 dBm rf power) is estimated to be 1.24 Oe. In the comparison between susceptibility maps $\chi(\omega)$ at $\omega = 0.5$ and 2.0 Ghz, we see that the higher frequency map is closer to to the FMR condition, with a large and mostly imaginary susceptibility.

9.2.5 Conclusion

We have demonstrated submicron (< 0.75 μm) imaging of complex GHz susceptibility $\tilde{\chi}(\omega)$, accessing small-to-medium-angle ($\sim 10^{\circ}$) magnetization dynamics, using scanning transmission x-ray microscopy. The technique is extensible to finer spatial resolution in submicron structures and layer-specific imaging in compositionally distinct layers, without

expected reduction in contrast, and is compatible with lock-in techniques [59,141] to enhance contrast. This technique will enable, for example, the study of eigenmodes in submicron device structures, possible before only for micron-size elements, and which we will present in the following final section of this thesis.

9.3 Phase-resolved imaging of spin-wave eigenmodes in submicron ellipses using scanning transmission xray microscopy

In this part we demonstrate the imaging of spin-wave eigenmodes in submicron ellipses using FMR-STXM, based on the experimental technique and data analysis routine discussed in Chap. 9.2.3. We have extended the spatial resolution to $\sim$ 40 nm, which is relevant for imaging functional spintronic devices. By controlling the symmetry of the rf excitation, we are able to resolve degenerate spin-wave eigenmodes with different symmetries, predicted by the micromagnetic simulations carried out using finite-element analysis of the Landau-Lifshitz-Gilbert (LLG) equation.

Degenerate spin-wave eigenmodes, with different symmetry, have the same distribution of the magnetization precession *amplitude* within the submicron FM thin film element. Therefore only imaging techniques providing high-resolution *phase* information are adequate for distinguishing them. While Brillouin light scattering (BLS) [142, 143] and time-resolved Kerr microscopy [132–135] are powerful tools for detecting spin-wave modes in small FM elements, the spatial resolution is limited by the wavelength of visible light. Most recently, Guo *et al.* [144] demonstrated the imaging of edge modes in Permalloy disks with spatial resolution of 100 nm, using ferromagnetic resonance force microscopy (FMRFM). The resolution is limited by the physical size of the scanning tip. Special care is required when preparing the magnetic tip, since a high stray field from the tip will disturb the intrinsic spin-wave modes within the FM thin film element. A critical point is that the FMRFM does not provide phase information; the contrast comes only from the amplitude of the magnetization precession. None of these other techniques mentioned gives layer-resolved imaging capability. Therefore, the TR x-ray microscopy is the only candidate which combines the advantages of nm regime spatial resolution, phase resolution, and layer-specificity in nanoscale (hetero-) structures.

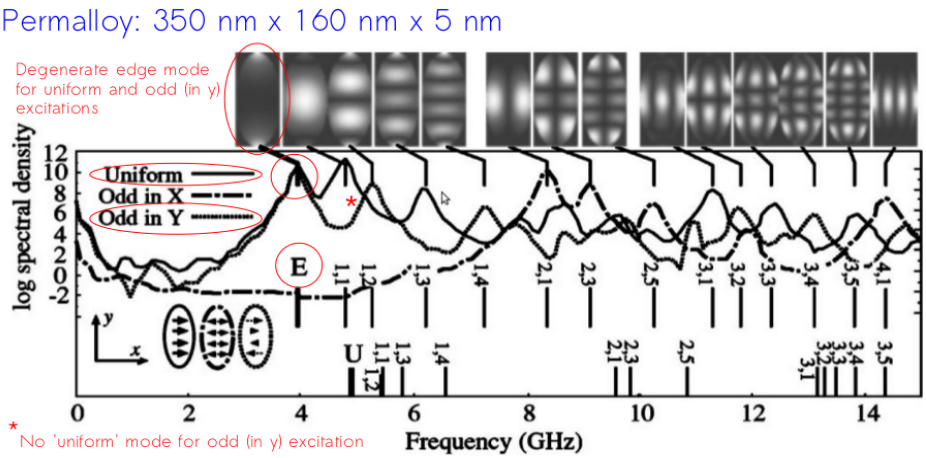

Figure 9.9: *from Ref. [145]* Spin-wave normal modes in a 350 nm × 160 nm × 5 nm Permalloy ($Ni_{80}Fe_{20}$) elliptical cylinder, simulated with OOMMF; constrast indicates the local magnetization precession amplitude.

9.3.1 Introduction: spin-wave eigenmodes

It has long been predicted by micromagnetic calculations that distinctive modes of standing spin-waves at different frequencies exist in small thin film FM elements under in-plane FMR, due to the finite lateral dimensions [145]. Fig. 9.9 [145] illustrates the calculated spin-wave normal modes in a 350 nm × 160 nm × 5 nm Permalloy ($Ni_{80}Fe_{20}$) elliptical cylinder. The calculation includes three sets of in-plane excitation fields: the solid line, the dot-dashed line and the fine dotted line represent the spectra for uniform driving field, driving field antisymmetric about the y-axis, and driving field antisymmetric about the x-axis, respectively. Each peak in the spectra corresponds to a specific resonance pattern in which the amplitude of the magnetization precession shows uniquely distributed nodes within the thin film element. The highest two peaks are in the lowest frequency range, corresponding to the 'edge' mode (E) and the 'uniform' mode (U), where the magnetization precession amplitude is the largest at the ends and the center of the ellipse, respectively. We notice further that the 'edge' modes are degenerate in the cases of uniform driving field and antisymmetric driving field about the x-axis, occuring at the same frequency with the same amplitude. The 'uniform' mode does not exist under antisymmetric driving fields; the

spin-wave mode pattern should reflect the symmetry of the driving field.

Fig. 9.10 shows our simulations results for $Ni_{81}Fe_{19}$ (Permalloy) elliptical cylinders with dimensions relevant for typical spintronic devices, 1000 nm $\times$ 500 nm $\times$ 20 nm in (a) and 1000 nm $\times$ 600 nm $\times$ 20 nm in (b). We used a different micromagnetic simulations package, *NMag*, based on the finite-element analysis of the LLG equation, from that used in Ref. [145] (OOMMF, a finite-difference method package) and reproduced comparable results, as the checking step for a reasonable simulation process. In the simulations, we first define the sample geometry and generate the finite-element mesh using the open source software *Netgen*. The largest mesh size is 5 nm, which is within the limit of the exchange length of Permalloy. With the geometry and mesh imported into NMag, we start with the sample saturated along the x-direction by setting the magnetization uniformly as $\mathbf{m} = (1, 0, 0)$. The hysteresis loop is obtained by applying a cyclic external field along the x-axis, letting the sample relax at each field point and recording the equilibrium magnetization. The hysteresis loops along the x-axis are shown in the left panel of Fig. 9.10 (a) and (b) for the two geometries, respectively. To get the remanent state of the sample, we let it relax from $\mathbf{m} = (1, 0, 0)$ under zero external field. Because of the large shape anisotropy introduced by the geometry of the elliptical cylinder, the Permalloy sample is almost uniformly magnetized along the x-axis at remanence, with only slight dispersion of the magnetization at the two tips of the ellipse.

To obtain the spin-wave modes under zero bias field in the simulation, we use the remanent state of the thin film sample as the static magnetization configuration. A square field pulse (duration $\sim$ 85 ps) of $\sim$ 12 Oe (very small compared with the shape anisotropy as could be inferred from the hysteresis loop) is applied along the y-axis uniformly over the whole space for even excitation. For odd excitation, the y-axis field is +12 Oe for $x > 0$ and -12 Oe for $x \leq 0$. The magnetization then relaxes after the field pulse, with the Gilbert damping parameter α set to 0.01, until reaching equilibrium. We take the data $\{\mathbf{m}(\mathbf{r}, t)\}$ in the whole sample during the time interval of 2.3 - 4.3 ns with step of 10 ps, and perform a fast Fourier transform (FFT) in each spatial element $d^3\mathbf{r}$ for $m_x(t)$, $m_y(t)$ and $m_z(t)$.

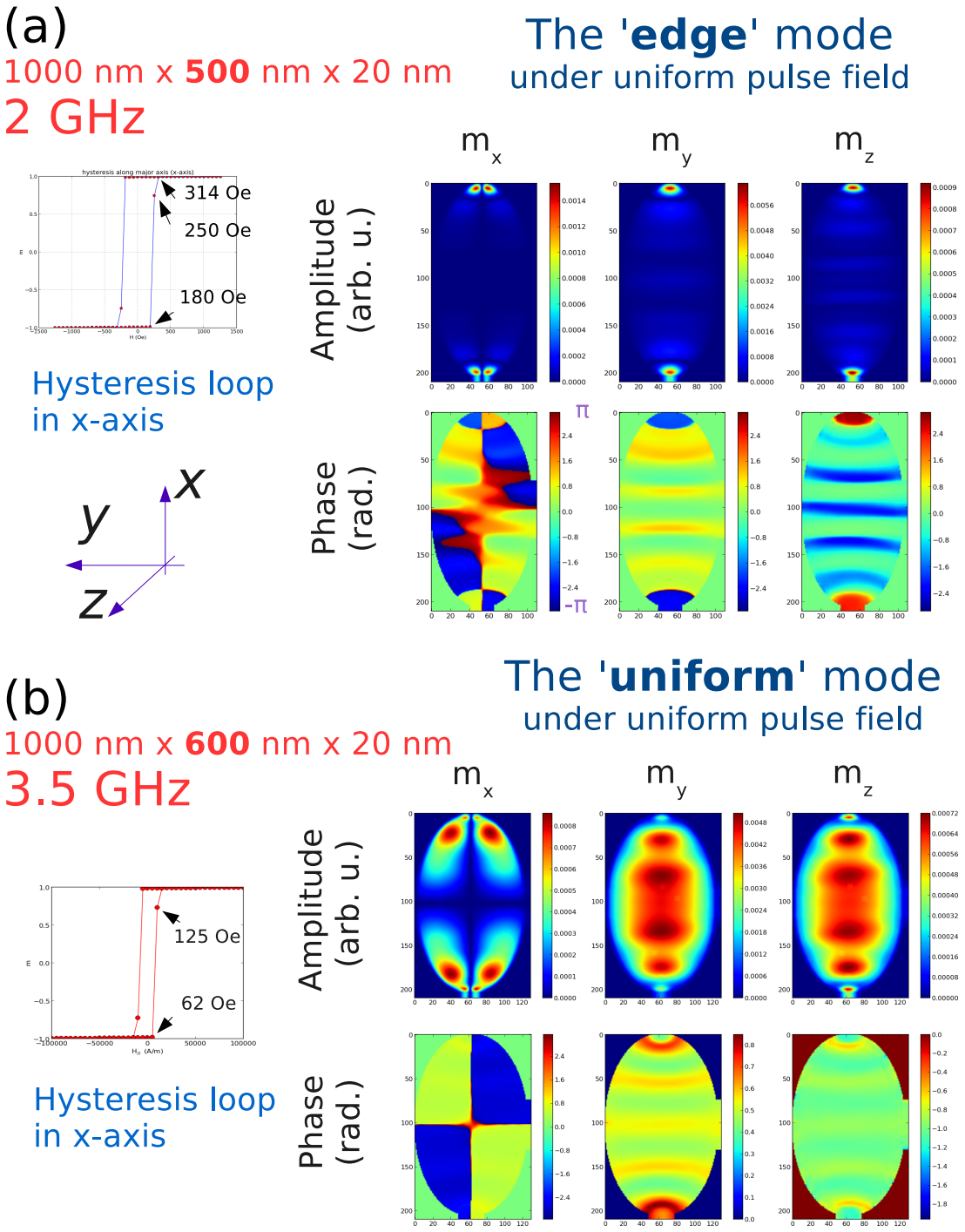

Figure 9.10: Spin-wave normal modes with amplitude and phase information, simulated with NMag, decomposed into the x-, y- and z-components; the left panel shows the simulated hysteresis loop of the element. (a) 1000 nm × 500 nm × 20 nm $Ni_{81}Fe_{19}$ elliptical cylinder at 2 GHz; (b) 1000 nm × 600 nm × 20 nm $Ni_{81}Fe_{19}$ elliptical cylinder at 3.5 GHz.

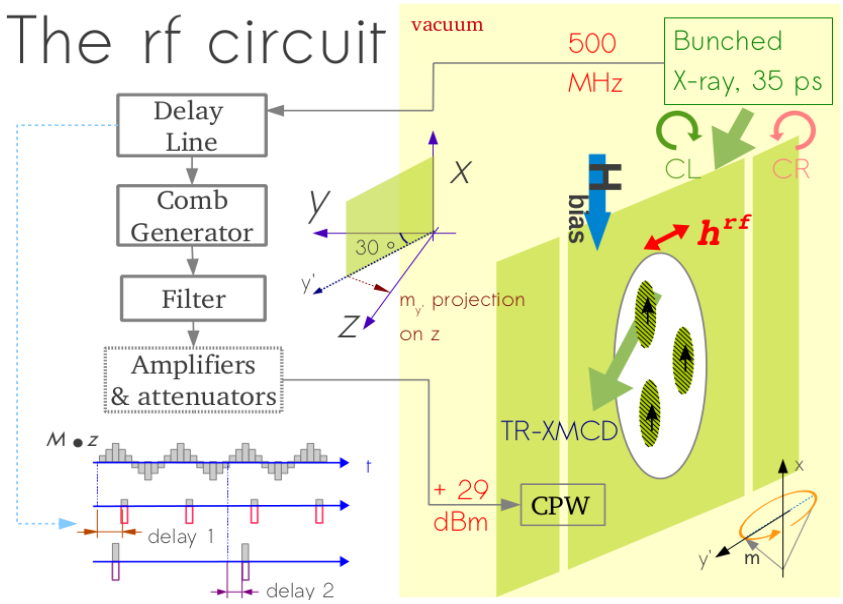

Figure 9.11: The rf circuit for TR-STXM using the *pump-probe* technique.

The time-domain data of the oscillating magnetization components m_x, m_y, m_z are then transformed into the frequency domain, and give the amplitude and phase at each discrete frequency. We plot the spatial distribution of the amplitude and phase for the x-, y- and z-components of **m** oscillation at 2 GHz in Fig. 9.10 (a) for the 1000 nm $\times$ 500 nm $\times$ 20 nm Permalloy sample, to show the 'edge' mode. Fig. 9.10 (b) shows the 'uniform' mode at 3.5 GHz for the 1000 nm $\times$ 600 nm $\times$ 20 nm Permalloy sample. Under uniform excitation, the phase maps are symmetric about the y-axis for m_y and m_z, and antisymmetric about the y-axis for m_x.

9.3.2 Experiment: odd and even excitation

The experimental setup for TR-STXM with the pump-probe technique was explained in detail in Chap.9.2.3. Here we review it briefly in Fig. 9.11. The 500 MHz x-ray bunch-clock signal is delayed at ps resolution to define the relative position in time of the rf pump and the x-ray probe. The combination of the comb generator and the filter selects the designated

harmonic of the 500 MHz input signal. In the experiments presented in this section, we used 2 GHz most of the time and fixed the power at + 29 dBm before sending the rf into the vacuum chamber. As we discussed in Chap.7, the magnetic contrast is proportional to $\sigma\hat{\mathbf{z}} \cdot \mathbf{M}$. Therefore the coplanar waveguide (CPW) (same as the sample plane) is tilted 30° away from the xy plane, which yields the magnetic contrast dominated by M_y. Note here that when comparing the experimental results with the simulations, we need only consider the m_y component.

In order to demonstrate the ability of our imaging techinique to distinguish between degenerate spin-wave eigenmodes, excitation rf fields in both odd and even symmetries are necessary. As we see from Fig. 9.11, the CPW generates uniform excitation field only. We fabricated special samples to achieve the odd and even excitations separately, as illustrated in Fig. 9.12. In (a), we show two types of samples. Both samples are patterned with e-beam lithography and subsequently the liftoff process. The thin FM films were deposited at optimized magnetron sputtering conditions (Ar 1.2 mTorr, DC 400 V) to achieve ideal soft magnetic properties. Sample *I* has the layer structure of Ta (3 nm)/ $Ni_{81}Fe_{19}$ (20 nm)/ Ta (3 nm), with the seed layer Ta (3 nm) to improve the film adhesion to the substrate and the homogeneity of the FM layer, and the top layer Ta (3 nm) to prevent oxidation. Sample *II* consists of Ta (2 nm)/ $Ni_{81}Fe_{19}$ (20 nm)/ SiO_2 (2 nm), where Ta (2 nm) is the seed and SiO_2 (2 nm) is the cap. The FM layers in the two samples are identical, and the 1 nm difference in the Ta seed layer thickness does not have any siginificant influence on the sample.

The crucial difference is the Cu (15 nm) layer on top of sample I. As explained in Fig. 9.12 (b), this extra layer of Cu introduces an odd rf excitation. We show the propagation of EM wave in the CPW on the *right* side of Fig. 9.12 (b). The wavevector **k** is along the center conductor of the CPW, with **E** field and **H** field in the plane perpendicular to **k**. Since we know already that the **H** field lies in the CPW/sample plane, the **E** field is perpendicular to the sample plane. The out-of-plane **E** field drives perpendicular rf current J_z^{rf} in the low-resistivity Cu layer, which generates the in-plane H^{rf} represented by the

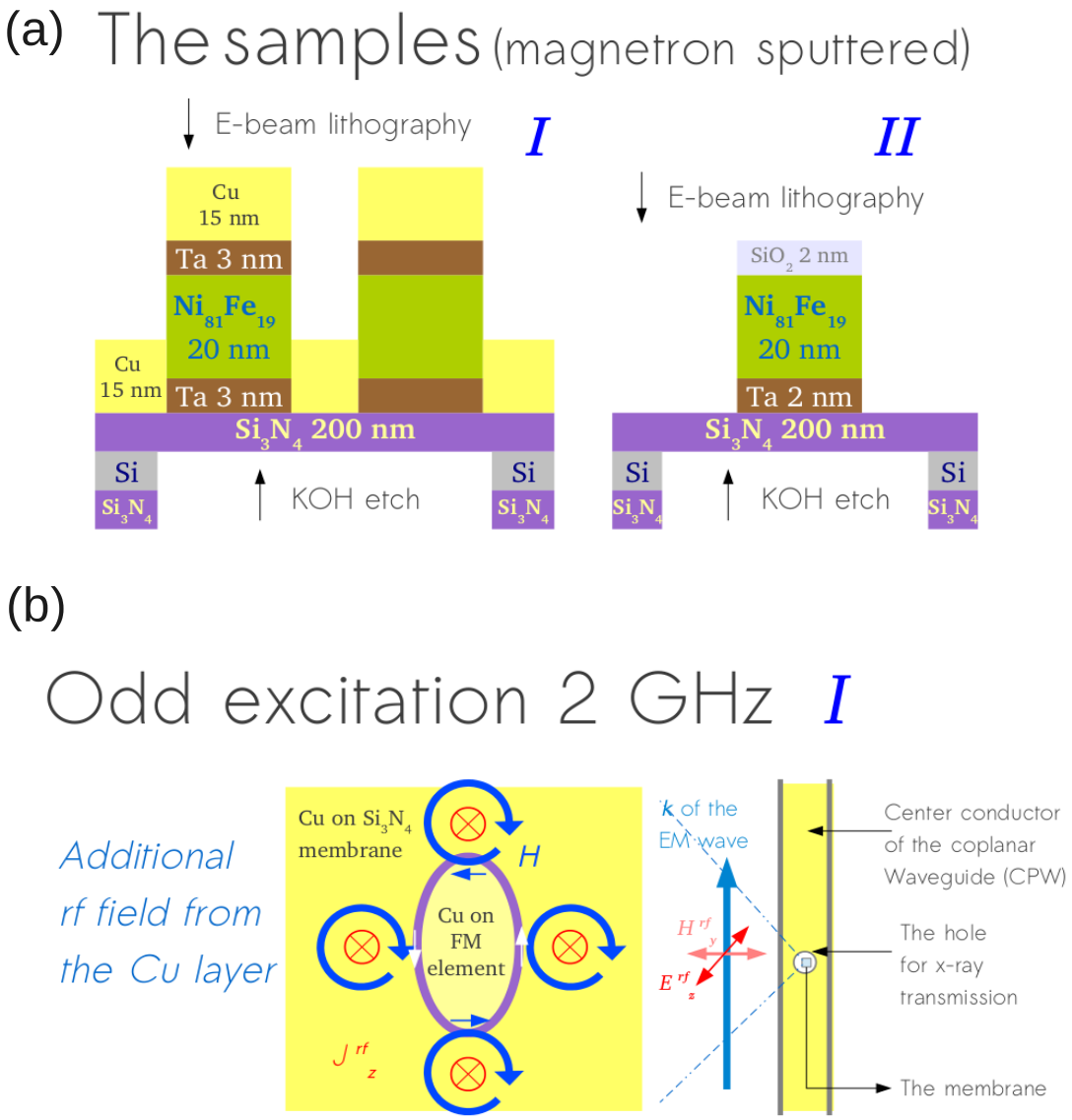

Figure 9.12: (a) Samples: I. odd excitation with the Cu capping layer; II. even excitation. (b) The origin of odd excitation in the Cu layer.

blue circular arrows in the figure. We see immediately that the H^{rf} at the top and the bottom of the elliptical thin film sample are antisymmetric about the y-axis. A detailed simulation work on the distribution of the **E** and **H** fields in a metallic film on CPW was carried out by Bailleul [146] which supports our argument. We would like to make the point here that since the sample is located right above the hole in the center conductor and is of extremely small size, only the ideal distribution of the **E** and **H** fields right above the center conductor has to be treated in our case, unlike in an extended FM film. For sample II, with absence of a highly conductive layer covering the sample, the **H** field sensed by the thin film elements are simply the uniform in-plane h^{rf} from the center conductor of the CPW, which is the even/uniform excitation.

9.3.3 Results and discussion

Finally in this part we present the direct observation of the spin-wave modes and the high-resolution phase distribution in the samples.

Fig. 9.13 demonstrates the 'edge' mode we observed in the 1000 nm × 500 nm × 20 nm $Ni_{81}Fe_{19}$ sample covered by Cu (15 nm). Comparing the simulation result illustrated at the upper left corner, we see a reasonable agreement between the calculation and the experimental observation, with the **M** precession amplitude concentrated at the edges of the ellipse. While the cone anlge is the largest at zero bias field under which the sample is on-resonance, when we apply external fields along the x-axis, the sample goes off-resonance and thus the amplitude of the **M** precession is reduced. The phase maps at 0 and 20 Oe bias are antisymmetric about the y-axis, consistent with the odd excitation experienced by the sample. Fig. 9.14 shows the dynamic response in the 1000 nm × 600 nm × 20 nm $Ni_{81}Fe_{19}$ sample covered by Cu (15 nm), under the same conditions as the sample presented in Fig. 9.13. The only difference is the sample dimension, which is reflected by the simulation result at the upper left corner. Instead of having an 'edge' mode at zero bias, this slightly wider (600 nm compared with 500 nm as in Fig. 9.13) sample exhibits a spin-wave pattern resembling the mixture of an 'edge' mode and the 'uniform' mode. This

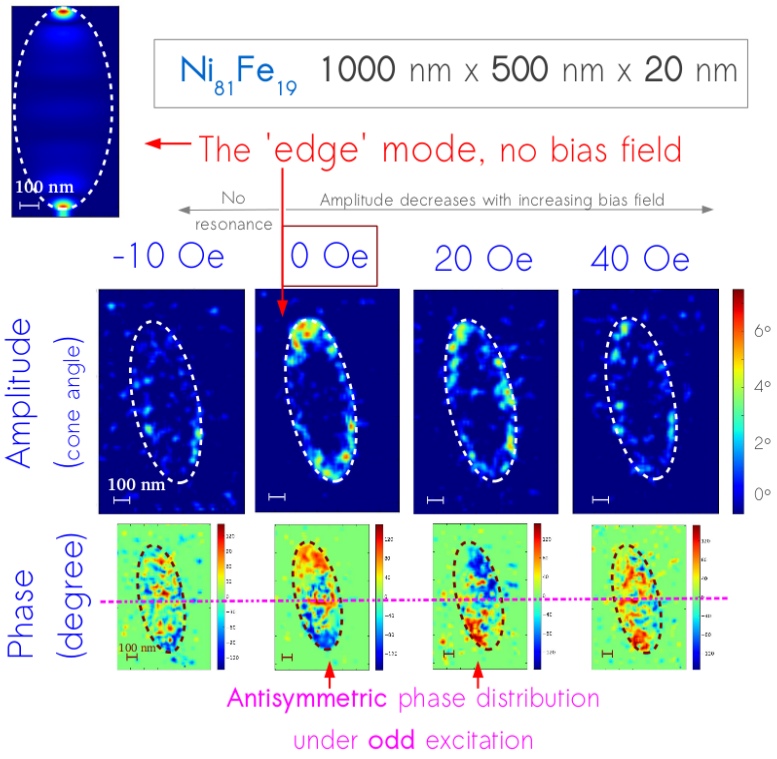

Figure 9.13: The 'edge' mode images at different bias fields, showing the difference between on-resonance and off-resonance.

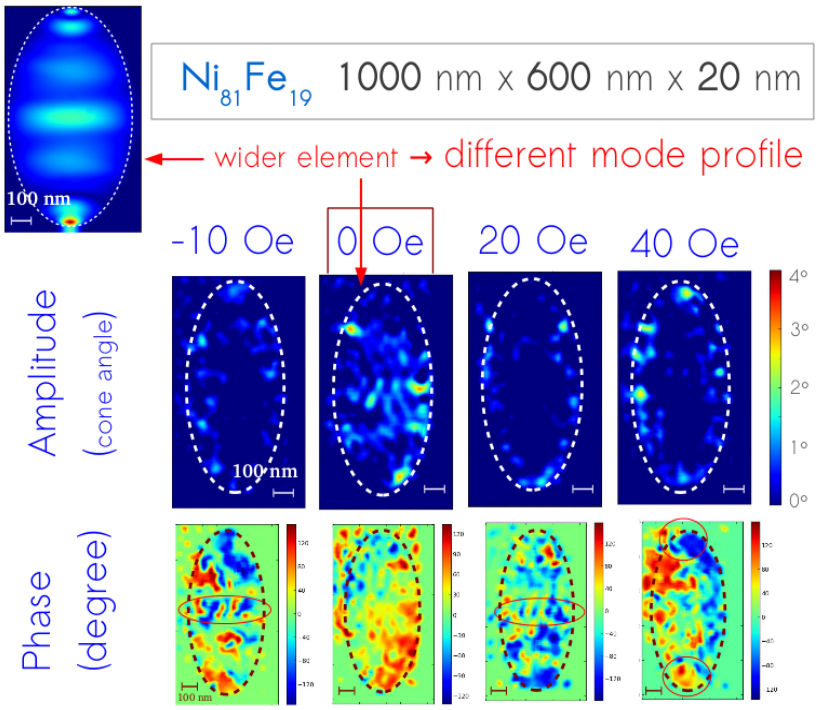

Figure 9.14: The mixed mode (between 'edge' and 'uniform') images at different bias fields, showing the difference between on-resonance and off-resonance.

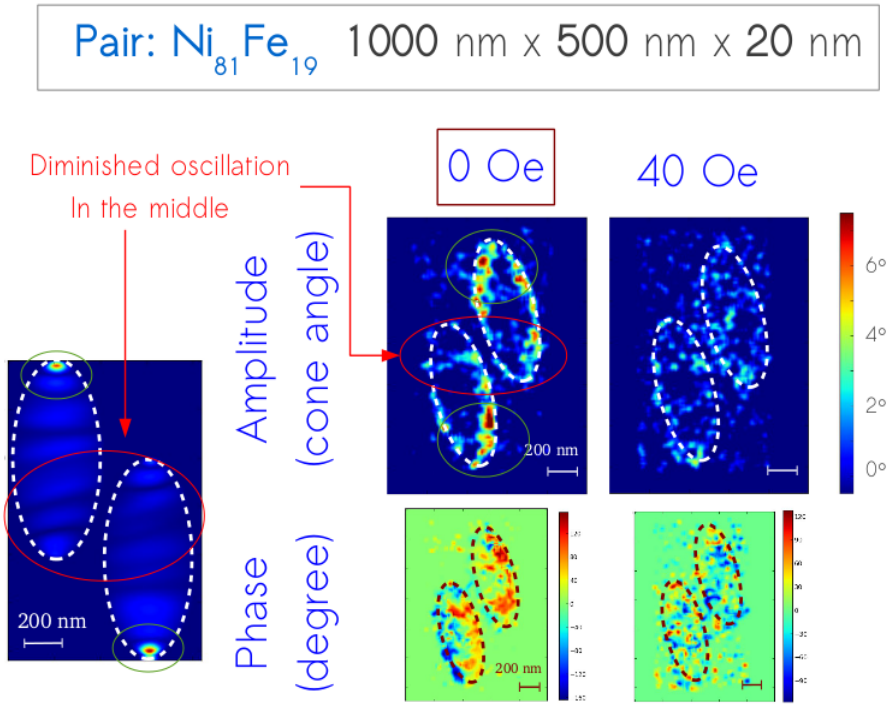

Figure 9.15: The mode images for a dipolarly coupled sample pair: the precession is suppressed in the middle part of the pair.

result is comprehensible based on the reduced shape anisotropy in the wider sample, as we could see from the hysteresis loops in Fig. 9.10. A lower shape anisotropy corresponds to a lower effective field H_B and thus lower ω_H in the Kittel relation, Eq. 5.49, leading to a lower resonance frequency ω_0. Therefore the frequencies at which the 'edge' mode and the 'uniform' mode occur are both shifted towards the low-frequency end for the wider element. According to Fig. 9.9, the 'uniform' mode occurs at higher frequency than the 'edge' mode. Since we fixed the rf excitation frequency at 2 GHz, the wider sample now sees a cross-over from the 'edge' mode to the 'uniform' mode. Again, we see a higher amplitude on-resonance compared with the off-resonance conditions, and the phase maps are antisymmetric about the y-axis.

Fig. 9.15 shows the results for a 1000 nm $\times$ 600 nm $\times$ 20 nm $Ni_{81}Fe_{19}$ pair under

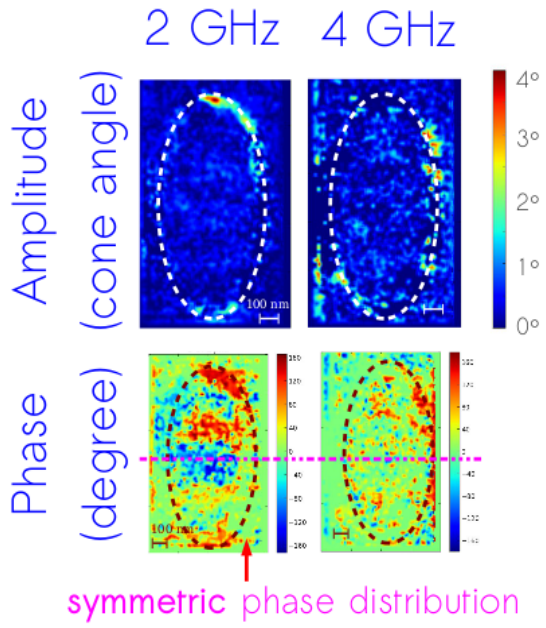

Figure 9.16: The mode images for a sample under even excitation: note the symmetric phase distribution about the y-axis.

odd excitation. Consistent with the simulation, the amplitude at the middle of the image, where the element pair experience relatively strong dipolar coupling, is suppressed. The phase distribution should reflect the symmetry of the excitation in this case.

Finally, we demonstrate the images from a sample under even excitation. The sample is under zero bias field and shows the 'edge' mode at 2 GHz excitation and no contrast at 4 GHz, consistent with the simulations. We point out here that the phase distribution for the 2 GHz case is symmetric about the y-axis, refecting the even excitation.

Conclusion From the images demonstrated, we conclude that we are able to resolve the different spin-wave eigenmodes with 40 nm resolution and clear phase information to distinguish between degenerate modes with different symmetries. Further extending this technique to multilayered structures with the element-specific imaging capability of x-ray, we see enormous potential for it to shed light on the dynamic studies in functional spintronic devices.

Bibliography

[1] S. A. Wolf, D. D. Awschalom, R. A. Buhrman, J. M. Daughton, S. von Molnar, M. L. Roukes, A. Y. Chtchelkanova, and D. M. Treger, "Spintronics: a spin-based electronics vision for the future," *Science*, vol. 294, p. 1488, 2001.

[2] R. Lavrijsen, A. Fernandez-Pacheco, D. Petit, R. Mansell, J. H. Lee, and R. P. Cowburn, "Tuning the interlayer exchange coupling between single perpendicularly magnetized CoFeB layers," *Applied Physics Letters*, vol. 100, no. 5, p. 052411, 2012. [Online]. Available: http://scitation.aip.org/content/aip/journal/apl/100/5/10.1063/1.3682103

[3] R. J. Spain and H. Rubinstein, "Thin-film switching in the hard direction by wall motion," *Journal of Applied Physics*, vol. 32, no. 3, pp. S288–S289, 1961. [Online]. Available: http://scitation.aip.org/content/aip/journal/jap/32/3/10.1063/1.2000441

[4] S. Chikazumi, *Physics of Magnetism.* John Wiley & Sons, INC., 1964.

[5] P. R. Ohodnicki, M. E. McHenry, and D. E. Laughlin, "Monte carlo studies of directional pair ordering in disordered binary and ternary ferromagnetic bcc crystalline alloys," *Journal of Applied Physics*, vol. 101, p. 09N118, 2007.

[6] J. F. Calleja, J. A. Corrales, M. Rivas, I. Iglesias, M. C. Contreras, and G. Suran, "Induced and local anisotropies in amorphous CoZr-rare earth thin films containing Pr, Nb and Tb," *Journal of Applied Physics*, vol. 79, p. 3168, 1996.

[7] H. Kronmuller and M. Fahnle, *Micromagnetism and the Microstructure of Ferromagnetic Solids.* Cambridge University Press, 2003.

[8] J. J. Quan, X. W. Zhou, and H. N. G. Wadley, "Low energy ion assisted atomic assembly of metallic superlattices," *Surface Science*, vol. 600, p. 2275, 2006.

[9] P. M. Martin, *Handbook of Deposition Technologies for Films and Coatings: Science, Applications and Technology.* Burlington : William Andrew, Incorporated, 2009.

[10] L. Hultman, J. Sundgren, J. E. Greene, D. B. Bergstrom, and I. Petrov, "High-flux low-energy (∼20 ev) n^{+2} ion irradiation during tin deposition by reactive magnetron sputtering: Effects on microstructure and preferred orientation," *Journal of Applied Physics*, vol. 78, p. 5395, 1995.

[11] M. Frommberger, C. Schmutz, M. Tewes, J. McCord, W. Hartung, R. Losehand, and E. Quandt, "Integration of crossed anisotropy magnetic core into toroidal thin-film inductors," *IEEE Transactions on Microwave Theory and Techniques*, vol. 53, p. 2096, 2005.

[12] C. Cheng, N. A. Sturcken, K. Shepard, and W. E. Bailey, "Vector control of induced magnetic anisotropy using an *in situ* quadrupole electromagnet in ultrahigh vacuum sputtering," *Review of Scientific Instruments*, vol. 83, p. 063903, 2012. [Online]. Available: http://dx.doi.org/10.1063/1.4725527

[13] R. Davies, N. Sturcken, C. Cheng, W. Bailey, and K. Shepard, "Coupled inductors with crossed-anisotropy CoZrTa/SiO_2 multilayer cores," *IEEE Transactions on Magnetics*, vol. 49, p. 4009, 2013.

[14] N. A. Sturcken, R. Davies, C. Cheng, W. E. Bailey, and K. Shepard, "Design of coupled power inductors with crossed-anisotropy magnetic core for integrated power conversion," *Proceedings of the IEEE Applied Power Electronics Conference and Exposition (APEC)*, p. 417, 2012.

[15] Y. Shiroishi, K. Fukuda, I. Tagawa, H. Iwasaki, S. Takenoiri, H. Tanaka, H. Mutoh, and N. Yoshikawa, "Future options for hdd storage," *IEEE Transactions on Magnetics*, vol. 45, p. 3816, 2009.

[16] J. M. Slaughter, "Materials for magnetoresistive random access memory," *Annual Review of Materials Research*, vol. 39, pp. 277–296, 2009.

[17] P. Ripka and M. Janosek, "Advances in magnetic field sensors," *IEEE Sensors Journal*, vol. 10, no. 6, pp. 1108–1116, 2010.

[18] P. P. Freitas, R. Ferreira, S. Cardoso, and F. Cardoso, "Magnetoresistive sensors," *Journal of Physics: Condensed Matter*, vol. 19, p. 165221, 2007.

[19] C. Tannous and J.Gieraltowski, "Giant magneto-impedance and its applications," *Journal of Materials Science: Materials in Electronics*, vol. 15, no. 2, pp. 125–133, 2004.

[20] C. R. Sullivan, "Integrating magnetics for on-chip power: challenges and opportunities," *Proceedings of the Custom Integrated Circuits Conference*, pp. 291–298, 2009.

[21] P. R. Morrow, C. M. Park, H. W. Koertzen, and J. T. DiBene, "Design and fabrication of on-chip coupled inductors integrated with magnetic material for voltage regulators," *IEEE Transactions on Magnetics*, vol. 47, p. 1678, 2011.

[22] M. Miura, H. Katahashi, K. Muramori, and M. Kajiyama, "Annealing behavior of magnetic anisotropy in CoNbZr films," *IEEE Transactions on Magnetics*, vol. 24, p. 2215, 1988.

[23] G. Suran, J. Sztern, and B. Barbara, "Well-defined in-plane uniaxial anisotropy in amorphous CoDyZr films," *Applied Physics Letters*, vol. 58, p. 1338, 1991.

[24] H. Raanaei, H. Nguyen, G. Andersson, H.Lidbaum, P.Korelis, K.Leifer, and B.Hjorvarsson, "Imprinting layer specific magnetic anisotropies in amorphous multilayers," *Journal of Applied Physics*, vol. 106, p. 023918, 2009.

[25] M. Frommberger, J. McCord, and E. Quandt, "High-frequency properties of FeCoSiB thin films with crossed anisotropy," *IEEE Transactions on Magnetics*, vol. 40, p. 2703, 2004.

[26] S. Zohar and W. E. Bailey, "Interface-related damping in polycrystalline $Ni_{81}Fe_{19}$ /Cu/ $Co_{93}Zr_7$ trilayers," *Journal of Applied Physics*, vol. 105, p. 07D309, 2009.

[27] N. Sturcken *et al.*, "A 2.5D integrated voltage regulator using coupled-magnetic-core inductors on silicon interposer delivering $10.8A/mm^2$," *Solid-State Circuits Conference Digest of Technical Papers (ISSCC), 2012 IEEE International*, pp. 400–402, 2012.

[28] G. Schrom, P. Hazucha, J. Hahn, D. Gardner, B. Bloechel, G. Dermer, S. Narendra, T. Karnik, and V. De, "A 480-MHz, multi-phase interleaved buck DC-DC converter with hysteretic control," *Power Electronics Specialists Conference, 2004. PESC 04. 2004 IEEE 35th Annual*, vol. 6, pp. 4702–4707, 2004.

[29] P. Hazucha *et al.*, "A 233-MHz 80converter utilizing air-core inductors on package," *IEEE Journal of Solid-State Circuits*, vol. 40, pp. 838–845, 2005.

[30] N. Sturcken, M. Petracca, S. Warren, L. Carloni, A. Peterchev, and K. Shepard, "An integrated four-phase buck converter delivering $1A/mm^2$ with 700ps controller delay and network-on-chip load in 45-nm SOI," *Custom Integrated Circuits Conference (CICC), 2011 IEEE*, pp. 1–4, 2011.

[31] J. Wright, D. W. Lee, A. Mohan, A. Papou, P. Smeys, and S. X. Wang, "Analysis of integrated solenoid inductor with closed magnetic core," *IEEE Transactions on Magnetics*, vol. 46, p. 2387, 2010.

[32] J. Lee, K. P. Hwang, and S. X. Wang, "Fabrication and analysis of high-performance integrated solenoid inductor with magnetic core," *IEEE Transactions on Magnetics*, vol. 44, p. 4089, 2008.

[33] C. Mathuna, N. Wang, S. Kulkarni, and S. Roy, "Review of integrated magnetics for Power Supply on Chip (PwrSoC)," *IEEE Transactions on Power Electronics*, vol. 27, p. 4799, 2012.

[34] J. Slonczewski, B. Petek, and B. E. Argyle, "Micromagnetics of laminated permalloy films," *IEEE Transactions on Magnetics*, vol. 24, p. 2045, 1988.

[35] H. Clow, "Very low coercive force in nickel-iron films," *Nature*, vol. 194, p. 1035, 1962.

[36] Y. Shimada and N. Saito, "Magnetic softness and domain wall structures of double-layered amorphous co-zr-nb films," *Japanese Journal of Applied Physics*, vol. 25, p. 419, 1986.

[37] H. Kronmuller, "Theory of the coercive field in amorphous ferromagnetic alloys," *Journal of Magnetism and Magnetic Materials*, vol. 24, p. 159, 1981.

[38] D. S. Gardner, G. Schrom, P. Hazucha, F. Paillet, T. Karnik, and S. Borkar, "Integrated on-chip inductors using magnetic material (invited)," *Journal of Applied Physics*, vol. 103, p. 07E927, 2008.

[39] A. Hubert and R. Schaefer, *Magnetic Domains.* Springer, Berlin-Heidelberg-New York, 1998.

[40] K. Hayashi, M. Hayakawa, Y. Ochiai, H. Matsuda, W. Ishikawa, Y. Iwasaki, and K. Aso, "Magnetic and other properties and sputtering behavior of co-base amorphous alloy films," *Journal of Applied Physics*, vol. 61, p. 2983, 1987.

[41] U. Queitsch, J. McCord, A. Neudert, R. Schafer, L. Schultz, K. Rott, and H. Bruckl, "Domain wall induced modes of high-frequency response in ferromagnetic elements," *Journal of Applied Physics*, vol. 100, p. 093911, 2006.

[42] K. Yamamoto, H. Matsuyama, Y. Hamakawa, and M. Kitada, "Magnetic domain structures and dynamics of cotazr/cr multilayered films," *Journal of Applied Physics*, vol. 75, p. 2998, 1994.

[43] M. Fahnle and C. Illg, "Electron theory of fast and ultrafast dissipative magnetization dynamics," *Journal of Physics: Condensed Matter*, vol. 23, p. 493201, 2011.

[44] J. Kunes and V. Kambersky, "First-principles investigation of the damping of fast magnetization precession in ferromagnetic $3d$ metals," *Physical Review B*, vol. 65, p. 212411, 2002.

[45] K. Gilmore, Y. U. Idzerda, and M. D. Stiles, "Identification of the dominant precession-damping mechanisms in Fe, Co, and Ni by first-principles calculations," *Physical Review Letters*, vol. 99, p. 027204, 2007.

[46] A. Brataas, Y. Tserkovnyak, and G. E. W. Bauer, "Scattering theory of Gilbert damping," *Physical Review Letters*, vol. 101, p. 037207, 2008.

[47] K. Gilmore and M. D. Stiles, "Anisotropic damping of the magnetization dynamics in Ni, Co, and Fe," *Physical Review B*, vol. 81, p. 174414, 2010.

[48] A. A. Starikov, P. J. Kelly, A. Brataas, Y. Tserkovnyak, and G. Bauer, "Unified first-principles study of Gilbert damping, spin-flip diffusion, and resistivity in transition metal alloys," *Physical Review Letters*, vol. 105, p. 236601, 2010.

[49] L. Berger, "Spin relaxation in metallic ferromagnets," *Physical Review B*, vol. 83, p. 054410, 2011.

[50] Y. Liu, A. A. Starikov, Z. Yuan, and P. J. Kelly, "First-principles calculations of magnetization relaxation in pure Fe, Co, and Ni with frozen thermal lattice disorder," *Physical Review B*, vol. 84, p. 014412, 2011.

[51] S. Mankovsky, D. Kodderitzsch, G. Woltersdorf, and E. H, "First-principles calculation of the Gilbert damping parameter via the linear response formalism with application to magnetic transition metals and alloys," *Physical Review B*, vol. 87, p. 014430, 2013.

[52] M. Fahnle and D. Steiauf, *Handbook of Magnetism and Advanced Magnetic Materials I*, ser. Dissipasive magnetization dynamics close to the adiabatic regime, H. Kronmuller and S. Parkin, Eds. Chichester: Wiley, 2007.

[53] V. Kambersky, "On the Landau-Lifshitz relaxation in ferromagnetic metals," *Canadian Journal of Physics*, vol. 48, p. 2906, 1970.

[54] K. Gilmore, Y. U. Idzerda, and M. D. Stiles, "Spin-orbit precession damping in transitional metal ferromagnets (invited)," *Journal of Applied Physics*, vol. 103, p. 07D303, 2008.

[55] S. M. Bhagat and P. Lubitz, "Temperature variation of ferromagnetic relaxation in the 3*d* transition metals," *Physical Review B*, vol. 10, p. 179, 1974.

[56] G. Counil, T. Devolder, J. V. Kim, P. Crozat, C. Chappert, S. Zoll, and R. Fournel, "Temperature dependences of the resistivity and the ferrromagnetic resonance linewidth in Permalloy thin films," *IEEE Transactions on Magnetics*, vol. 42, p. 3323, 2006.

[57] K. Fuchs, "The conductivity of thin metallic films according to the electron theory of metals," *Mathematical Proceedings of the Cambridge Philosophical Society*, vol. 34, p. 100, 1938.

[58] L. Van der Pauw, "A method of measuring specific resistivity and Hall effect of discs of arbitrary shape," *Philips Research Reports*, vol. 13, pp. 1–9, 1958.

[59] D. A. Arena, Y. Ding, E. Vescovo, S. Zohar, Y. Guan, and W. E. Bailey, "A compact apparatus for studies of element and phase-resolved ferromagnetic resonance," *Review of Scientific Instruments*, vol. 80, p. 083903, 2009.

[60] A. Ghosh, J. F. Sierra, S. Auffret, U. Ebels, and W. E. Bailey, "Dependence of nonlocal Gilbert damping on the ferromagnetic layer type in ferromagnet Cu/Pt heterostructures," *Applied Physics Letters*, vol. 98, p. 052508, 2011.

[61] J. Stohr and H. Siegmann, *Magnetism: From Fundamentals to Nanoscale Dynamics*. Springer, Berlin-Heidelberg-New York, 2006.

[62] C. Zener, "Classical theory of the temperature dependence of magnetic anisotropy energy," *Physical Review*, vol. 96, p. 1335, 1954.

[63] R. Pauthenet, "Experimental verification of spinwave theory in high fields (invited)," *Journal of Applied Physics*, vol. 53, p. 8187, 1982.

[64] W. P. Ayres, P. H. Vartanian, and J. L. Melchor, "Frequency doubling in ferrites," *Journal of Applied Physics*, vol. 27, p. 188, 1956.

[65] N. Bloembergen and S. Wang, "Relaxation effects in para- and ferromagnetic resonance," *Physical Review*, vol. 93, p. 72, 1954.

[66] H. Suhl, "The theory of ferromagnetic resonance at high signal powers," *Journal of Physics and Chemistry of Solids*, vol. 1, p. 209, 1957.

[67] J. D. Bierlein and P. M. Richards, "Harmonic generation and parametrically coupled spin waves in yttrium iron garnet," *Physical Review B*, vol. 1, p. 4342, 1970.

[68] G. P. Ridrigue, "Magnetism in microwave devices," *Journal of Applied Physics*, vol. 40, p. 929, 1969.

[69] V. G. Harris, "Modern microwave ferrites," *IEEE Transactions on Magnetics*, vol. 48, p. 1075, 2012.

[70] V. E. Demidov, S. Urazhdin, H. Ulrichs, V. Tiberkevich, A. Slavin, D. Baither, G. Schmitz, and S. O. Demokritov, "Magnetic nano-oscillator driven by pure spin current," *Nature Materials*, vol. 11, p. 1028, 2012.

[71] A. Berteaud and H. Pascard, "Nonlinear behavior of ferromagnetic thin films," *Journal of Applied Physics*, vol. 37, p. 2035, 1966.

[72] T. Gerrits, P. Krivosik, M. L. Schneider, C. E. Patton, and T. J. Silva, "Direct detection of nonlinear ferromagnetic resonance in thin films by the magneto-optical Kerr effect," *Physical Review Letters*, vol. 98, p. 207602, 2007.

[73] H. M. Olson, P. Krivosik, K. Srinivasan, and C. E. Patton, "Ferromagnetic resonance saturation and second order Suhl spin wave instability processes in thin Permalloy films," *Journal of Applied Physics*, vol. 102, p. 023904, 2007.

[74] M. Bao, A. Khitun, Y. Wu, J. Lee, K. L. Wang, and A. P. Jacob, "Coplanar waveguide radio frequency ferromagnetic parametric amplifier," *Applied Physics Letters*, vol. 93, p. 072509, 2008.

[75] Y. Khivintsev, J. Marsh, V. Zagorodnii, I. Harward, J. Lovejoy, P. Krivosik, R. E. Camley, and Z. Celinski, "Nonlinear amplification and mixing of spin waves in a microstrip geometry with metallic ferromagnets," *Applied Physics Letters*, vol. 98, p. 042505, 2011.

[76] J. Marsh, V. Zagorodnii, Z. Celinski, and R. E. Camley, "Nonlinearly generated harmonic signals in ultra-small waveguides with magnetic films: Tunable enhancements of 2nd and 4th harmonics," *Applied Physics Letters*, vol. 100, p. 102404, 2012.

[77] M. Yana, P. Vavassori, G. Leaf, F. Fradin, and M. Grimsditch, *Journal of Magnetism and Magnetic Materials*, vol. 320, p. 1909, 2008.

[78] V. E. Demidov, H. Ulrichs, S. Urazhdin, S. O. Demokritov, V. Bessonov, R. Gieniusz, and A. Maziewski, "Resonant frequency multiplication in microscopic magnetic dots," *Applied Physics Letters*, vol. 99, p. 012505, 2011.

[79] C. Bi, X. Fan, L. Pan, X. Kou, J. Wu, Q. Yang, H. Zhang, and J. Q. Xiao, "Electrical detection of nonlinear ferromagnetic resonance in single elliptical Permalloy thin film using a magnetic tunnel junction," *Applied Physics Letters*, vol. 99, p. 232506, 2011.

[80] H. L. Glass and M. T. Elliott, "Attainment of the intrinsic FMR linewidth in yttrium iron garnet films grown by liquid phase epitaxy," *Journal of Crystal Growth*, vol. 34, p. 285, 1976.

[81] A. G. Gurevich and G. A. Melkov, *Magnetization Oscillation and Waves*. CRC, Boca Raton, 1996.

[82] Y. U. Chen, C. T.and Idzerda, H. J. Lin, N. V. Smith, M. G., E. Chaban, G. H. Ho, E. Pellegrin, F. Sette, Y. Ma, and S. Modesti, "Experimental confirmation of the x-ray magnetic circular dichroism sum rules for iron and cobalt," *Physical Review Letters*, vol. 75, p. 152, 1995.

[83] R. N. Hall, G. E. Fenner, J. D. Kingsley, T. J. Soltys, and R. O. Carlson, "Coherent light emission from GaAs junctions," *Physical Review Letters*, vol. 9, p. 366, 1962.

[84] I. Hayashi, M. B. Panish, P. W. Foy, and S. Sumski, "Junction lasers which operate continuously at room temperature," *Applied Physics Letters*, vol. 17, p. 109, 1970.

[85] R. Kohler, A. Tredicucci, F. Beltram, H. Beere, E. Linfield, A. Davies, D. Ritchie, R. Iotti, and F. Rossi, "Terahertz semiconductor-heterostructure laser," *Nature*, vol. 417, p. 156, 2002.

[86] B. D. Josephson, "The discovery of tunnelling supercurrents," *Review of Modern Physics*, vol. 46, p. 251, 1974.

[87] Y. Nakamura, H. Terai, K. Inomata, T. Yamamoto, W. Qiu, and Z. Wang, "Superconducting qubits consisting of epitaxially grown NbN/AlN/NbN junctions," *Applied Physics Letters*, vol. 99, p. 212502, 2011.

[88] D. R. Smith, W. J. Padilla, D. C. Vier, S. C. Nemat-Nasser, and S. Schultz, "Composite medium with simultaneously negative permeability and permittivity," *Physical Review Letters*, vol. 84, p. 4184, 2000.

[89] A. Hoffman, L. Alekseyev, S. Howard, K. Franz, D. Wasserman, V. Podolskiy, E. Narimanov, D. Sivco, and C. Gmachl, "Negative refraction in semiconductor metamaterials," *Nature Materials*, vol. 6, p. 946, 2007.

[90] N. D. Lanzillotti-Kimura, A. Fainstein, B. Perrin, B. Jusserand, A. Soukiassian, X. X. Xi, and D. G. Schlom, "Enhancement and inhibition of coherent phonon emission of a Ni film in a $BaTiO_3/SrTiO_3$ cavity," *Physical Review Letters*, vol. 104, p. 187402, 2010.

[91] R. P. Beardsley, A. V. Akimov, M. Henini, and A. J. Kent, "Coherent terahertz sound amplification and spectral line narrowing in a stark ladder superlattice," *Physical Review Letters*, vol. 104, p. 085501, 2010.

[92] E. Goulielmakis *et al.*, "Direct measurement of light waves," *Science*, vol. 305, p. 1267, 2004.

[93] J. Y. Bigot, M. A. Mycek, S. Weiss, R. G. Ulbrich, and D. S. Chemla, "Instantaneous frequency dynamics of coherent wave mixing in semiconductor quantum wells," *Physical Review Letters*, vol. 70, p. 3307, 1993.

[94] M. S. Yeganeh, J. Qi, A. G. Yodh, and M. C. Tamargo, "Interface quantum well states observed by three-wave mixing in ZnSe/GaAs heterostructures," *Physical Review Letters*, vol. 68, p. 3761, 1992.

[95] E. O. Göbel, H. Jung, J. Kuhl, and K. Ploog, "Recombination enhancement due to carrier localization in quantum well structures," *Physical Review Letters*, vol. 51, p. 1588, 1983.

[96] A. Tulapurkar, Y. Suzuki, A. Fukushima, H. Kubota, H. Maehara, K. Tsunekawa, D. Djayaprawira, N. Watanabe, and S. Yuasa, "Spin-torque diode effect in magnetic tunnel junctions," *Nature*, vol. 438, p. 339, 2005.

[97] G. Woltersdorf, O. Mosendz, B. Heinrich, and C. H. Back, "Magnetization dynamics due to pure spin currents in magnetic double layers," *Physical Review Letters*, vol. 99, p. 246603, 2007.

[98] H. Kubota *et al.*, "Quantitative measurement of voltage dependence of spin-transfer torque in MgO-based magnetic tunnel junctions," *Nature Physics*, vol. 1, p. 37, 2008.

[99] O. Mosendz, J. Pearson, F. Fradin, G. Bauer, S. Bader, and A. Hoffmann, "Quantifying spin Hall angles from spin pumping: Experiments and theory," *Physical Review Letters*, vol. 104, p. 046601, 2010.

[100] M. Harder, Z. X. Cao, Y. S. Gui, X. L. Fan, and C.-M. Hu, "Analysis of the line shape of electrically detected ferromagnetic resonance," *Physical Review B*, vol. 84, p. 054423, 2011.

[101] D. Arena, C. Kao, E. Vescovo, Y. Guan, and W. E. Bailey, "Weakly coupled motion of individual layers in ferromagnetic resonance," *Physical Review B*, vol. 74, p. 064409, 2006.

[102] B. Thole, P. Carra, F. Sette, and G. van der Laan, "X-ray circular dichroism as a probe of orbital magnetization," *Physical Review Letters*, vol. 68, p. 1943, 1992.

[103] R. Weber and P. Tannenwald, "Long-range exchange interactions from spin-wave resonance," *Physical Review*, vol. 149, p. A498, 1965.

[104] N. Chan, V. Kambersky, and D. Fraitova, "Impedance matrix of thin metallic ferromagnetic films and SSWR in parallel configuration," *Journal of Magnetism and Magnetic Materials*, vol. 214, p. 93, 2000.

[105] M. Kostylev, "Strong asymmetry of microwave absorption by bilayer conducting ferromagnetic films in the microstrip-line based broadband ferromagnetic resonance," *Journal of Applied Physics*, vol. 106, p. 043903, 2009.

[106] W. Ament and G. Rado, "Electromagnetic effects of spin wave resonance in ferromagnetic metals," *Physical Review*, vol. 97, p. 1558, 1955.

[107] R. Urban, G. Woltersdorf, and B. Heinrich, "Gilbert damping in single and multilayer ultrathin films: role of interfaces in nonlocal spin dynamics," *Physical Review Letters*, vol. 87, p. 217204, 2001.

[108] S. Parkin, C. Kaiser, A. Panchula, P. Rice, B. Hughes, M. Samant, and S.-H. Yang, "Giant tunnelling magnetoresistance at room temperature with MgO (100) tunnel barriers," *Nature Materials*, vol. 3, p. 862, 2004.

[109] C. Cheng and W. E. Bailey, "Sub-micron mapping of GHz magnetic susceptibility using scanning transmission x-ray microscopy," *Applied Physics Letters*, vol. 101, p. 182407, 2012.

[110] S. Polisetty, J. Zhou, J. Karthik, A. R. Damodaran, D. Chen, A. Scholl, L. W. Martin, and M. Holcomb, "X-ray linear dichroism dependence on ferroelectric polarization," *Journal of Physics: Condensed Matter*, vol. 24, p. 245902, 2012.

[111] W. Chao, B. Harteneck, J. Liddle, E. Anderson, and D. Attwood, "Soft x-ray microscopy at a spatial resolution better than 15 nm," *Nature*, vol. 435, p. 1210, 2005.

[112] D. A. Allwood, G. Xiong, C. C. Faulkner, D. Atkinson, D. Petit, and R. P. Cowburn, "Magnetic domain-wall logic," *Science*, vol. 309, p. 1688, 2005.

[113] C. Chappert, A. Fert, and F. N. V. Dau, "The emergence of spin electronics in data storage," *Nature Materials*, vol. 6, p. 813, 2007.

[114] S. S. P. Parkin, M. Hayashi, and L. Thomas, "Magnetic domain-wall racetrack memory," *Science*, vol. 320, p. 190, 2008.

[115] A. Krasyuk, F. Wegelin, S. Nepijko, H. Elmers, G. Schonhense, M. Bolte, and C. Schneider, "Self-trapping of magnetic oscillation modes in Landau flux-closure structures," *Physical Review Letters*, vol. 95, p. 207201, 2005.

[116] G. Woltersdorf and C. H. Back, "Microwave assisted switching of single domain $Ni_{80}Fe_{20}$ elements," *Physical Review Letters*, vol. 99, p. 227207, 2007.

[117] L. Bocklage, B. Kruger, P. Fischer, and G. Meier, "Analytical modeling and x-ray imaging of oscillations of a single magnetic domain wall," *Physical Review B*, vol. 81, p. 054404, 2010.

[118] D. S. Gardner, G. Schrom, F. Paillet, B. Jamieson, T. Karnik, and S. Borkar, "Review of on-chip inductor structures with magnetic films," *IEEE Transactions on Magnetics*, vol. 45, p. 4760, 2009.

[119] R. Meere, T. O'Donnell, N. Wang, N. Achotte, S. Kulkarni, and S. C. O'Mathuna, "Size and performance tradeoffs in micro-inductors for high frequency DC-DC conversion," *IEEE Transactions on Magnetics*, vol. 45, p. 4234, 2009.

[120] C. Nistor, E. Faraggi, and J. L. Erskine, "Magnetic energy loss in Permalloy thin films and microstructures," *Physical Review B*, vol. 72, p. 014404, 2005.

[121] S. Yang and J. L. Erskine, "Domain wall dynamics and Barkhausen jumps in thin-film Permalloy microstructures," *Physical Review B*, vol. 72, p. 064433, 2005.

[122] H. Stoll *et al.*, "High-resolution imaging of fast magnetization dynamics in magnetic nanostructures," *Applied Physics Letters*, vol. 84, p. 3328, 2004.

[123] Y. Acremann, V. Chembrolu, J. P. Strachan, T. Tyliszczak, and J. Stohr, "Software defined photon counting system for time resolved x-ray experiments," *Review of Scientific Instruments*, vol. 78, p. 014702, 2007.

[124] G. Schutz, W. Wagner, W. Wilhelm, P. Kienle, R. Zeller, R. Frahm, and G. Materlik, "Absorption of circularly polarized x rays in iron," *Physical Review Letters*, vol. 58, p. 737, 1987.

[125] J. Stohr, Y. Wu, B. D. Hermsmeier, M. G. Samant, G. R. Harp, S. Koranda, D. Dunham, and B. P. Tonner, "Element-specific magnetic microscopy with circularly polarized x-rays," *Science*, vol. 259, p. 658, 1993.

[126] P. Fischer, T. Eimuller, G. Schutz, P. Guttmann, G. Schmahl, K. Pruegl, and G. Bayreuther, "Imaging of magnetic domains by transmission x-ray microscopy," *Journal of Physics D (Applied Physics)*, vol. 31, p. 649, 1998.

[127] B. Hong, T. Hayward, C. Barnes, and J. Jeong, "Double vortex interaction in micron-sized elliptical $Ni_{80}Fe_{20}$ elements studied by real-time Kerr microscopy," *IEEE Transactions on Magnetics*, vol. 45, p. 2511, 2009.

[128] N. D. Rizzo, M. DeHerrera, J. Janesky, B. Engel, J. Slaughter, and S. Tehrani, "Thermally activated magnetization reversal in submicron magnetic tunnel junctions for magnetoresistive random access memory," *Applied Physics Letters*, vol. 80, p. 2335, 2002.

[129] R. Sato, K. Kudo, T. Nagasawa, H. Suto, and K. Mizushima, "Simulations and experiments toward high-data-transfer-rate readers composed of a spin-torque oscillator," *IEEE Transactions on Magnetics*, vol. 48, p. 1758, 2012.

[130] W. Rippard, M. Pufall, S. Kara, T. Silva, S. Russek, and J. Katine, "Injection locking and phase control of spin transfer nano-oscillators," *Physical Review Letters*, vol. 95, p. 067203, 2005.

[131] C. Wang, Y. T. Cui, J. Sun, J. Katine, R. Buhrman, and D. Ralph, "Sensitivity of spin-torque diodes for frequency-tunable resonant microwave detection," *Journal of Applied Physics*, vol. 106, p. 053905, 2009.

[132] C. H. Back, R. Allenspach, W. Weber, S. Parkin, D. Weller, E. Garwin, and H. Siegmann, "Minimum field strength in precessional magnetization reversal," *Science*, vol. 285, p. 864, 1999.

[133] I. Neudecker, M. Klaui, K. Perzlmaier, D. Backes, L. Heyderman, C. Vaz, J. Bland, U. Rudiger, and C. H. Back, "Spatially resolved dynamic eigenmode spectrum of Co rings," *Physical Review Letters*, vol. 96, p. 057207, 2006.

[134] S. Tamaru, J. A. Bain, R. J. M. van de Veerdonk, T. M. Crawford, M. Covington, and M. H. Kryder, "Imaging of quantized magnetostatic modes using spatially resolved ferromagnetic resonance," *Journal of Applied Physics*, vol. 91, p. 8034, 2002.

[135] I. Neudecker, F. Hoffmann, G. Woltersdorf, and C. H. Back, "Imaging magnetic excitations in confined magnetic structures," *Journal of Physics D (Applied Physics)*, vol. 41, p. 164010, 2008.

[136] X. Yu *et al.*, "Images of a spin-torque-driven magnetic nano-oscillator," *Physical Review Letters*, vol. 106, p. 167202, 2011.

[137] B. V. Waeyenberge *et al.*, "Magnetic vortex core reversal by excitation with short bursts of an alternating field," *Nature*, vol. 444, p. 461, 2006.

[138] X. Cheng, K. Buchanan, R. Divan, K. Guslienko, and D. Keavney, "Nonlinear vortex dynamics and transient domains in ferromagnetic disks," *Physical Review B*, vol. 79, p. 172411, 2009.

[139] W. E. Bailey, L. Cheng, D. Keavney, C.-C. Kao, E. Vescovo, and D. Arena, "Precessional dynamics of elemental moments in a ferromagnetic alloy," *Physical Review B*, vol. 70, p. 172403, 2004.

[140] A. M. Kaiser, C. Wiemann, S. Cramm, and C. M. Schneider, "Spatially resolved observation of uniform precession modes in spin-valve systems," *Journal of Applied Physics*, vol. 109, p. 07D305, 2011.

[141] C. Cheng, K. Kaznatcheev, and W. E. Bailey, "Stochastic limits in synchronous imaging of sub-micron magnetization dynamics using scanning transmission x-ray microscopy," *Journal of Applied Physics*, vol. 111, p. 07E321, 2012.

[142] V. E. Demidov, U.-H. Hansen, and S. O. Demokritov, "Spin-wave eigenmodes of a saturated magnetic square at different precession angles," *Physical Review Letters*, vol. 98, p. 157203, 2007.

[143] V. E. Demidov, M. Buchmeier, K. Rott, P. Krzysteczko, J. Munchenberger, G. Reiss, and S. O. Demokritov, "Nonlinear hybridization of the fundanmental eigenmodes of microscopic ferromagnetic ellipses," *Physical Review Letters*, vol. 104, p. 217203, 2010.

[144] F. Guo, L. M. Belova, and R. D. McMichael, "spectroscopy and imaging of edge modes in Permalloy nanodisks," *Physical Review Letters*, vol. 110, p. 017601, 2013.

[145] R. D. McMichael and M. D. Stiles, "Magnetic normal modes of nanoelements," *Journal of Applied Physics*, vol. 97, p. 10J901, 2005.

[146] M. Bailleul, "Shielding of the electromagnetic field of a coplanar waveguide by a metal film: Implications for broadband ferromagnetic resonance measurements," *Applied Physics Letters*, vol. 103, p. 192405, 2013.